Computing Landscape, Velocity and Flux of Probability Mass in Gene Regulatory Networks

by

Anna Terebus
B.S., Rivne State Humanitarian University, Rivne, Ukraine, 2008
M.S., Rivne State Humanitarian University, Rivne, Ukraine, 2009

THESIS

Submitted as partial fulfillment of the requirements
for the degree of Doctor of Philosophy in Bioinformatics
in the Graduate College of the
University of Illinois at Chicago, 2019

Chicago, Illinois

Defense Committee:
Prof. Jie Liang, Chair and Advisor, Deparment of Bioengineering
Prof. Yang Dai, Department of Bioengineering
Prof. Ao Ma, Department of Bioengineering
Prof. Thomas Royston, Department of Bioengineering
Prof. Chun Liu, Department of Applied Mathematics, Illinois Institute of Technology

To my father,

Viktor Terebus,

who could not be here for my defense, but who was my first teacher of mathematics

and science, and my memories of him will never fade

A.T.

ACKNOWLEDGMENTS

I want to thank many people who contributed to my thesis in multiple ways, while supporting and encouraging me, criticizing my work or bringing me new ideas.

First of all, I would like to thank my advisor, Professor Jie Liang. He was always thoughtful, and while being very strict in his assignments and requirements, would always give me the opportunity to implement my own ideas. Dr. Liang would encourage and inspire me to work hard, by giving me the opportunity to participate in distinguished meetings and conferences and meet many accomplished scientists. Dr. Liang also taught me to write scientific papers.

I also want to thank my committee members: Dr. Chun Liu, Dr. Yang Dai, Dr. Ao Ma, and Dr. Thomas Royston. I would like to give special thanks to Dr. Chun Liu, who introduced me to the velocity of the probability concept, and who has been always supporting. The meetings we had were always very helpful and encouraging. The ideas and thoughts that Dr. Liu shared with me turned out to be crucial for my thesis work. Dr. Yang Dai taught me very important classes, which were always very organized and full of important projects. Dr. Ao Ma would always challenge me by asking questions, which would go far beyond the subject, and make me think all the way to sources. Dr. Thomas Royston gave me a great example of leadership, while also being a department head.

I would like to thank my past lab members, who while being my peers, were my first mentors in research and life in a different country, particularly, to Dr. Gamze Gursoy, Dr. Meishan Lin, Dr. Jieling Zhao, Dr. Ke Tang, Dr. Yun Xu, Dr. David Jimenez-Morales, and Dr. Youfang

ACKNOWLEDGMENTS (Continued)

Cao. My special thanks to Gamze Gursoy who is my role model scientist and very good friend, who would always help with the advice on different research perspectives, and served me as an inspiration for working hard and being a strong woman. I would also like to thank my current lab team, Wei Tian, Alan Perez-Rathke, Boshen Wang, Xue Lei, Farid Manuchehrfar, Pourya Delafrouz, Samira Mali, Lin Du, without them every day in the lab would not be the same.

I want to thank all my friends which I met in Chicago and friends from Ukraine for their support and encouragement. Special thanks to Amira Kefi, my good friend, who I met at the Bioinformatics program. Amira was always there for me in the hard times and happy moments.

I would like to thank Dr. Kenneth Brezinsky and all the College of Engineering Toastmasters Club. They helped me to become a better speaker and presenter. While communicating on toastmasters stage, I learned how to better communicate to people in daily life.

I am also very thankful to Graduate Student Council of UIC, and all people who I met there. I want to thank to all the GSC Officers and Executive Committee members starting from 2017. I believe we were a good team, and we achieved many great things together, and we shared so many happy and positive moments, which helped to inspire me for big research accomplishments. I want to specially thank Dean Linda Deanna, who while being my GSC mentor gave me valuable advice for my PhD studies and my life.

I also want to thank Andrii Bomba, Professor in the Department of Applied Mathematics, in Rivne State Humanitarian University. Writing a thesis for the Little Academy of Science competition in High School under his advising turned out to determine my goal to become a scientist. I want to thank my high school teacher of Mathematics, Liliya Ostapchuk, who

Contribution of Authors

Chapter 1 is a literature review of the concepts and theories studied in my PhD thesis.
Chapter 2 is based on work which has been done in collaboration with Dr. Youfang Cao,
former postdoc of Dr. Jie Liang, and published in the following papers:

- Terebus, Anna, Youfang Cao, and Jie Liang. "Exact computation of probability landscape
  of stochastic networks of single input and coupled toggle switch modules." 36th Annual
  International Conference of the IEEE Engineering in Medicine and Biology Society. IEEE,
  2014.

- Cao, Youfang, Anna Terebus, and Jie Liang. "Accurate chemical master equation solution
  using multi-finite buffers." Multiscale Modeling Simulation 14.2 (2016): 923-963.

- Cao, Youfang, Anna Terebus, and Jie Liang. "State space truncation with quantified er-
  rors for accurate solutions to discrete chemical master equation." Bulletin of mathematical
  biology 78.4 (2016): 617-661.

Dr. Cao developed the multi-finite buffer method and implemented the software, as well as
introduced the concept of state space aggregation. I proved the theorem about the inequality
between the probability of the aggregated state on the truncated states space and the aggregated
state on the state space without truncation. I worked with Dr. Cao and Dr. Liang on proofs
of the rest of the theorems and lemmas in the paper. Dr. Cao and I both worked on finding
theoretical error bounds and numerical computations of the examples. Dr. Cao and Dr. Liang
played large roles in discussion of the problems and writing the manuscripts.

Chapter 3 of this thesis is based on two manuscripts, one of them is accepted, and one is in preparation:

- Terebus, Anna, Youfang Cao, and Jie Liang. "Sensitivities of Regulation Intensities in Feed-Forward Loops with Multistability." 41st Annual International Conference of the IEEE Engineering in Medicine and Biology Society. IEEE, 2019.

- Terebus, Anna, Youfang Cao, and Jie Liang. "Network Motif of Feed-Forward Loop with multistability is a mediator of a Phenotypic Switch in Cells", manuscript.

Dr. Cao and Dr. Liang played large roles in the discussion of the problems. Dr. Liang also contributed in writing the manuscript.

Chapter 4 is based on the publication:

- Terebus, Anna, Chun Liu, and Jie Liang. "Discrete flux and velocity fields of probability and their global maps in reaction systems." The Journal of chemical physics 149.18 (2018): 185101.

Dr. Liu posed the general problem. Dr. Liang and I formulated and developed the key concepts, and I further developed the full theory. Dr. Liang and Dr. Liu played large roles in the discussion of the problems. Dr. Liang also made a significant contribution into discussing the results and writing of the manuscript.

In **Chapter 5** is based on a manuscript, which is ready for submission:

- Terebus, Anna, Chun Liu, and Jie Liang. Discrete and Continuous Models of Probability Flux of Switching Dynamics: A Case Study of Toggle-Switch System. manuscript

Among the three models discussed in the paper the Liouville model was suggested by Dr. Liu. Dr. Liang and Dr. Liu played the large roles in the discussion of the problems. Dr. Liang also made a significant contribution into formulating the problems, discussing the results, and writing of the manuscript. The section 5.5 is not a part of any other manuscripts at present moment.

Chapter 6 summarizes the results of the thesis and provides with the directions for future research.

TABLE OF CONTENTS

LIST OF TABLES

LIST OF FIGURES

LIST OF ABBREVIATIONS

ACME   Accurate Chemical Master Equation

dCME   Discrete Chemical Master Equation

FFL   Feed-forward Loop

MEG   Molecular equivalence group

ODE   Ordinary differential equation

SDE   Stochastic differential equation

SUMMARY

Gene regulatory networks are collections of molecules which regulate gene expression, namely, the levels of messenger RNAs (mRNAs) and their protein products. Gene regulatory networks control essential cellular processes, including cellular differentiation, cell fate, signal transduction, and metabolic regulations. Modeling of gene regulatory networks is very important.

Many computational models have been developed for modeling gene regulatory networks. Deterministic models study the processes in gene regulatory networks under assumptions of the higher species concentrations. However, when the copy numbers of molecules involved are small and the differences in reaction rates are large, stochasticity plays an important role in cellular processes governed by these networks.

The discrete Chemical Master Equation (dCME) provides a fundamental framework for studying the underlying stochastic processes of biological networks. However, directly solving the dCME is challenging due to the enormous size of the state space. Therefore it is necessary to truncate the state space, thus, the accuracy of such truncation needs to be assessed.

Here a new technique for effective state space enumeration, based on the introduction of multiple buffer queues for molecular species is proposed. It allows *a priori* evaluation of the truncation error for each of these buffer queues and computing the error bound of the solution.

The method for accurate solution of dCME allows to model behavior of gene regulatory networks in highly stochastic regime. Particularly, stochastic modeling suggests the appearance of phenotypic switch from slow promoter binding, which can lead to distinct expression levels

SUMMARY (Continued)

with considerable lifetime. Due to the challenges with solving of dCME, these issues are still not well understood. In this work the multistability in the feed-forward loop (FFL), where feedback and cooperativities are absent, is studied in detail. The extensive exploration of the the full parameter space of reaction rates, including regulations intensities, and the number of genes involved, provides global phase diagrams of the multistable properties of FFL. Furthermore, the studies of the sensitivities of the regulation intensities in FFL suggest that the parameter sensitivities depend on the number of peaks in this network.

While the time-evolving probability landscape or equivalently reaction trajectories define the overall stochastic behavior of the systems, vector fields of probability flux and probability velocity can further characterize time-varying and steady-state stochastic properties of the systems, including the degree of departure from the detailed balance at the steady-state for non-equilibrium systems, high probability paths, barriers, and checkpoints between different stable regions in multistable systems, as well as mechanisms of dynamic switching among different cellular states.

Conventional probability fluxes on continuous space are ill-defined and are problematic when at boundaries of the state space or when copy numbers are small. By re-defining the derivative and divergence operators based on the discrete nature of reactions, new formulations of discrete flux are introduced in this work. Such flux model fully accounts for the discreteness of both the state space and the jump processes of reactions and satisfies discrete version of continuity equation. The steady state and time-evolving probability fluxes and velocity fields were computed for several examples, including multistable feedbacks. The obtained results

SUMMARY (Continued)

suggest the existence of oscillations in the toggle switch with slow promoter binding. Such behavior was not shown before, and cannot be determined with the conventional Fokker-Planck flux model or newly developed Liouville flux model based on ordinary differential equations.

CHAPTER 1

INTRODUCTION

The genome encodes genes whose protein products are required for structure, function and regulation of the cells. The abundance of proteins and other molecular products of genes are controlled by the gene regulatory networks.

Modeling of gene regulatory networks allows quantification of interactions between molecular species in the cell. When copy numbers of participating species are small and differences in reaction rates are large, behavior of gene regulatory networks is intrinsically stochastic [1,2]. It means that starting from the same initial state the system can evolve along different trajectories and can reach to different states.

While the discrete Chemical Master Equation [3–5] (dCME) provides a general framework to study stochasticity in mesoscopic gene regulatory networks, there are a number of different approaches based on dCME to analyze the probability landscape of stochastic gene regulatory networks [6–8,8–16]. The stochastic simulation algorithm [6–10] (SSA) of Gillespie provides means to sample reaction trajectories rigorously from the underlying network dCME. Fokker-Planck and Langevin models are stochastic differential equation (SDE) models based on continuous approximations of the dCME, under the assumption of Gaussian noises [8, 12–14]. Ordinary differential equations models, under further simplifying assumptions of large concentrations, can describe changes in mean concentrations of the molecular species, although stochasticity is not taken into account [15, 16].

While directly solving dCME can help to investigate biological networks under highly stochastic regime, its solution remains difficult, as an analytical solution is possible only for a few simple cases, and computational solutions require the enumeration of the state space of an enormous size. Finite buffer method allows enumeration of state space for the exact solution of dCME based on the buffer concept [17,18]. However, the truncation of the state space implies the truncation error. In this work a new method based on multiple buffers for more effective enumeration is introduced, and mathematical guarantees for the *a priori* and computational bounds of the error for each buffer are shown.

Gene regulatory networks may be of very large scale and therefore studying them under highly stochastic conditions is challenging. Whereas gene regulatory networks motifs are small building blocks of gene regulatory networks consisting of several genes and proteins [19], which usually have well defined functionality and architecture. Feed-forward loop network motif is a gene regulatory network motif with top to down regulation, abundant in mammalian cell, particularly in stem cell pluripotency networks [20–22], microRNA regulation networks [23–25], and cancer networks [25]. Its abundance can suggest importance of feed-forward loop in cell differentiation, where the multistability in protein copy numbers plays an important role.

Current understanding of the origin of multiple stable points for protein concentration resides largely on feedback loops and cooperativity in the gene coregulations [26]. Recent studies suggest origin of phenotypic switch from slow promoter binding creating distinct expression levels with considerable lifetime [27–30]. Accurate solution of dCME enables studying how the complex behavior of multistability can be achieved from the simple feed-forward loop and

investigate the sensitivities of regulation intensities of the FFL by examining the effect of the change of the strength of the regulation between the genes. The obtained results suggest that the sensitivities of parameters depend on number of peaks.

In addition to probability landscape, it is also important to characterize the probability flux and velocity fields of a stochastic network [31–38], as they can help to further infer the mechanisms of network functions, including switching between cellular states [31, 32], and identification of barriers and checkpoints between them [39]. Furthermore, flux and velocity fields of probability can characterize the departure of the non-equilibrium steady state of a network from equilibrium, which helps to understand the non-linear behavior of the network [35, 40, 41]. Computing probability fluxes and velocity fields has also found applications in studies of stem cell differentiation [42], cell cycle [39], and cancer development [43, 44].

Main challenge in finding such flux and velocity functions is developing the concept of transport of probability (as any other quantity following the continuity equation) [45, 46] on the discrete state space. In order to overcome this challenge, the reactional flux, satisfying continuity equation, and the specie flux, indicating the amount of probability mass moving in each direction were proposed in this work.

The important concepts for this work are introduced below.

1.1   Discrete Chemical Master Equation.

The discrete Chemical Master Equation describes the time-evolution of a well-mixed biological system with constant volume and temperature, that can be modelled as being in proba-

bilistic combination of states at any given time and switching between the states is determined by transition rate matrix.

We consider biochemical system with n molecular species X_i, $i = \{1, \ldots, n\}$, which participate in m reactions R_k, $k = \{1, \ldots, m\}$. The *microstate* $\mathbf{x}(t)$ of the system at time t is a non-negative integer column vector of copy numbers of the molecular species: $\mathbf{x}(t) \equiv (x_1(t), x_2(t), \ldots, x_n(t))^T \in \mathbb{Z}_+^n$. All the microstates that the system can reach form *the state space* $\Omega = \{\mathbf{x}(t) | t \in (0, \infty)\}$. The size of the state space is denoted as $|\Omega|$.

The probability of the system to be at a microstate $\mathbf{x}$ at time t is denoted as $p(\mathbf{x}, t) \in \mathbb{R}_{[0,1]}^m$. The probability surface or landscape $\mathbf{p}(t)$ over the state space Ω is denoted as $\mathbf{p}(\mathbf{x}) = \{p(\mathbf{x}(t) | \mathbf{x}(t) \in \Omega)\}$.

A reaction R_k takes the general form
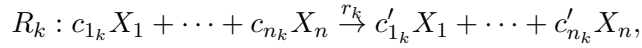
$$R_k : c_{1_k} X_1 + \cdots + c_{n_k} X_n \xrightarrow{r_k} c'_{1_k} X_1 + \cdots + c'_{n_k} X_n,$$

so that R_k brings the system from a microstate $\mathbf{x}$ to $\mathbf{x} + \mathbf{s}_k$, where the stoichiometry vector $\mathbf{s}_k \equiv (s_k^1, \ldots, s_k^n) \equiv (c'_{1_k} - c_{1_k}, \ldots, c'_{n_k} - c_{n_k})$ gives the unit vector of *the discrete increment* for reaction R_k. The reaction rate $A_k(\mathbf{x}, \mathbf{x} + \mathbf{s}_k)$ is determined by the product of the intrinsic reaction rate r_k and the combinations of relevant reactants in the current microstate $\mathbf{x}$:

$$A_k(\mathbf{x}, \mathbf{x} + \mathbf{s}_k) = A_k(\mathbf{x}) = r_k \prod_{l=1}^{n} \binom{x_l}{c_{lk}}.$$

Discrete Chemical Master Equation (dCME) is a set of linear ordinary differential equations describing the probability changes of each microstate of the system over time [7, 17, 18]. The dCME for an arbitrary microstate $\mathbf{x} = \mathbf{x}(t)$ can be written in the general form as:

$$\frac{dp(\mathbf{x}, t)}{dt} = \sum_{k=1}^{m} A_k(\mathbf{x} - \mathbf{s}_k) p(\mathbf{x} - \mathbf{s}_k, t) - A_k(\mathbf{x}) p(\mathbf{x}, t), \quad \mathbf{x} - \mathbf{s}_k, \mathbf{x} \in \Omega. \tag{1.1}$$

Direct solving of dCME directly requires an efficient and adequate account of the discrete state space. It is a challenging problem, therefore many studies involve continuous approximations of dCME.

1.2 Continuous Approximations of dCME

1.2.1 Deterministic Equation from the Law of Mass Action

Deterministic model of reactions describe the time-evolving mean value or concentration $\langle X_i \rangle$ of each molecular species X_i. The deterministic equations can be written generically at $\langle \mathbf{X} \rangle = (\langle X_1 \rangle, \ldots, \langle X_n \rangle)$ as

$$\frac{\partial \langle X_1 \rangle}{\partial t} = F_1(\langle X_1 \rangle, \ldots, \langle X_n \rangle);$$

$$\ldots \tag{1.2}$$

$$\frac{\partial \langle X_n \rangle}{\partial t} = F_n(\langle X_1 \rangle, \ldots, \langle X_n \rangle).$$

Here the functions

$$\mathbf{F}(\langle \mathbf{X} \rangle) \equiv (F_1(\langle X_1 \rangle, \ldots, \langle X_n \rangle), \ldots, F_n(\langle X_1 \rangle, \ldots, \langle X_n \rangle)) \tag{1.3}$$

characterize how the the *vector of molecular concentrations* $\langle \mathbf{X} \rangle$ changes with time. Based on (Equation 1.2)–(Equation 1.3), the Law of Mass Action can be written in the matrix form, as:

$$\frac{\partial \langle \mathbf{X} \rangle}{\partial t} = \mathbf{F}(\langle \mathbf{X} \rangle) \tag{1.4}$$

A standard deterministic model is based on the underlying chemical rate equations, namely, the law of mass action [47]. Here the rate of a chemical reaction is directly proportional to the product of the activities or concentrations of the reactants. Therefore, functions $F(\langle X_i \rangle)$ in (Equation 1.2) can be written:

$$F_i(\langle X_1 \rangle, \ \dots, \ \langle X_n \rangle) = \sum_{k=1}^{m} (s_k^i) r_k \langle X_1 \rangle^{|s_k^1|} \cdot \dots \cdot \langle X_n \rangle^{|s_k^n|}. \tag{1.5}$$

The law of Mass Action can be derived from dCME (Equation 1.1) using the theory of moment-closure approximations at high copy numbers [48–53].

1.2.2 Approximation Model of Fokker-Planck Equation

The Fokker-Planck model can be derived under the assumptions of i) small jumps between states due to firing of reactions, namely, $|s_k/V| < \epsilon$, where $\epsilon \to 0$, ii) slow change of the probability, namely, $|p(x) - p(x + s_k/V)| < \delta$ where $\delta \to 0$ for reaction R_k with stoichiometry s_k and system volume V. With these assumptions, the transition kernel $A_k(\mathbf{x} - \mathbf{s}_k/V) p(\mathbf{x} - \mathbf{s}_k/V, t)$ becomes differentiable to a high degree.

The model of the Fokker-Planck equation can be derived from the multivariate Taylor expansion or the Kramers-Moyal expansion of the discrete Chemical Master Equation [37]:

$$
\begin{aligned}
\frac{\partial p(\mathbf{x}, t)}{\partial t} &= \sum_{k=1}^{m} \left[A_k(\mathbf{x} - \frac{1}{V}\mathbf{s}_k)p(\mathbf{x} - \frac{1}{V}\mathbf{s}_k, t) - A_k(\mathbf{x})p(\mathbf{x}, t) \right] \\
&\approx \sum_{k=1}^{m} \left[A_k(\mathbf{x})p(\mathbf{x}, t) - \mathbf{s}_k\frac{1}{V}\nabla_{\mathbf{x}}A_k(\mathbf{x})p(\mathbf{x}, t) \right. \\
&\quad \left. + \frac{1}{2V^2}\mathbf{s}_k^T\nabla_{\mathbf{x}}\nabla_{\mathbf{x}}A_k(\mathbf{x})p(\mathbf{x}, t)\mathbf{s}_k - A_k(\mathbf{x})p(\mathbf{x}, t) \right. \\
&= \sum_{k=1}^{m} \left[-\frac{1}{V}\mathbf{s}_k\nabla_{\mathbf{x}}A_k(\mathbf{x})p(\mathbf{x}, t) + \frac{1}{2V^2}\mathbf{s}_k^T\nabla_{\mathbf{x}}\nabla_{\mathbf{x}}A_k(\mathbf{x})p(\mathbf{x}, t)\mathbf{s}_k \right].
\end{aligned}
\tag{1.6}
$$

In Fokker-Planck models terms higher than two are neglected [37].

1.3   Flux and Velocity of Probability. Continuity Equation.

The evolution of the probability landscape can be regarded as a process of movement of probability mass in the state space. The total probability mass is conserved at any time and sums up to one. A continuity equation for probability was introduced in [45, 46]. It is defined on a set of average molecular mass concentrations $\langle \mathbf{X} \rangle = (\langle X_1 \rangle, ..., \langle X_n \rangle) \in \mathbb{R}_+^n$:

$$
\frac{dp(\langle \mathbf{X} \rangle, t)}{dt} + \nabla_{\langle \mathbf{X} \rangle}\mathbf{J}(\langle \mathbf{X} \rangle, t) = 0,
\tag{1.7}
$$

where $\mathbf{J} = \mathbf{J}(\langle \mathbf{X} \rangle, t)$ is the vector of probability flux vector, namely, the flow of probability in the direction of each specie.

As the velocity of the probability is related to the flux by the relationship $\mathbf{J}(\langle\mathbf{X}\rangle, t) = \mathbf{v}(\langle\mathbf{X}\rangle, t)p(\langle\mathbf{X}\rangle, t)$, the continuity equation can also be written in terms of velocity as:

$$\frac{dp(\langle\mathbf{X}\rangle, t)}{dt} + \nabla_{\langle\mathbf{X}\rangle}\mathbf{v}(\langle\mathbf{X}\rangle, t)p(\langle\mathbf{X}\rangle, t) = 0. \tag{1.8}$$

1.4 Network Motifs.

Network motifs are simple building blocks of gene regulatory networks, occurring much more frequently in real biological networks compared to randomly generated networks [54]. Network motifs usually have very simple architecture and well-defined functionality. They consist of several nodes pairwise connected with the edges. The edges of genetic motifs map the interactions between protein and their target genes, whereas the nodes map the biological molecules involved in these interactions. There are two types of interactions between the nodes of the gene regulatory network, namely, activation and inhibition. Under the condition of inhibition, after the gene gets bound by its transcription factor, its expression level decreases. Under the condition of activation, after the gene gets bound by its transcription factor, its expression level increases. Two most abundant network motifs in nature are feed-forward and feedback loops (Figure 1) [19].

1.4.1 Feed-Forward Loop

The regulation in feed-forward loop is carried out from the top nodes towards the bottom ones by two regulation paths, such as the direct regulation from the top input node A to the output node C, and the indirect regulation from the input to the output through intermediate

buffer node B. Based on equality or inequality of the signs of regulation on the direct and indirect paths, there are two conventionally defined classes of feed forward loops, coherent Figure 1(A) and incoherent feed-forward loops Figure 1(B) correspondingly. Each regulatory link is either up or down regulation, and therefore there are eight types of feed-forward loop in total.

1.4.2 Feedback Loop

The feedback loop is simple two node gene regulatory network motif, consisting of two nodes A and B Figure 1(C), which mutually regulate each other. There are three types of feedback loops, namely, A and B mutually inhibit each other, A and B mutually activate each other, A activates B whereas B inhibits A (note, that the symmetrical case is equivalent). The feedback with mutual inhibition is also called toggle-switch.

1.5 Thesis Outline and Project Overview

My research focuses on accurate modeling of the behavior of stochastic gene regulatory networks. Specifically, I design the models and methods for accurate studying of gene regulatory networks, under the stochastic regime, when the copy numbers of molecules involved are small or differences in the reaction scales are large. The research described in this dissertation is organized as follows: **In chapter 2**, new method for accurate solution of discrete Chemical Master Equation, called Accurate Chemical Equation (ACME) method, was developed. It is based on introducing multiple buffer queues. For each buffer queue the error is predefined *a priori*. Therefore it allows to pre-estimate buffer size before the state space is enumerated. This chapter has been done in collaboration with Youfang Cao, former postdoc from the Liang
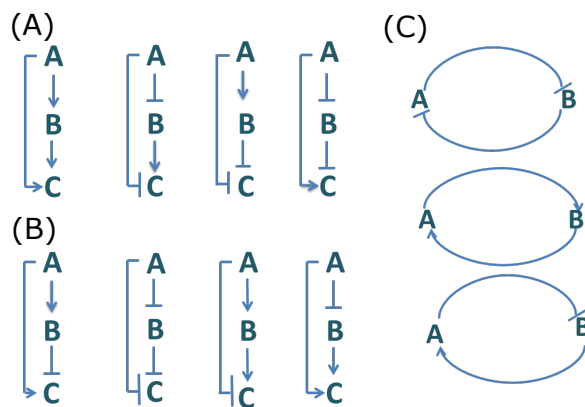
Figure 1.   Simple gene regulatory network motifs: (A) Schematic representation of four types of coherent feed-forward loops: (B) Schematic representation of four types of incoherent feed-forward loops. (C) Schematic representation of three types of feedback motifs.

lab, who developed the multi-finite buffer method and implemented the software, and who introduced the concept of state space aggregation. I proved the theorem about the inequality between the probability of the aggregated state on the truncated states space and the aggregated state on the state space without truncation. I worked with Dr. Cao and Dr. Liang on proofs of the rest of the theorems and lemmas in the paper. Dr. Cao and I both worked on finding theoretical error bounds and numerical computations of the examples. Dr. Cao and Dr. Liang played large roles in discussion of the problems and writing the manuscripts. This chapter is based on the publications:

- Terebus, Anna, Youfang Cao, and Jie Liang. "Exact computation of probability landscape of stochastic networks of single input and coupled toggle switch modules." 2014 36th Annual International Conference of the IEEE Engineering in Medicine and Biology Society. IEEE, 2014.

- Cao, Youfang, Anna Terebus, and Jie Liang. "Accurate chemical master equation solution using multi-finite buffers." Multiscale Modeling Simulation 14.2 (2016): 923-963.

- Cao, Youfang, Anna Terebus, and Jie Liang. "State space truncation with quantified errors for accurate solutions to discrete chemical master equation." Bulletin of mathematical biology 78.4 (2016): 617-661.

Chapter 3 of this thesis is devoted to modeling of the feed-forward loop with introduced ACME method. I showed that a complex behavior of multistability can be generated from the simple feed-forward loop network without cooperativity and feedback. I showed that the regulation intensities between different nodes of FFL play the important role in defining the number of peaks, under the conditions of slow promoter binding. I also studied the sensitivities of regulation intensities of the FFL. The results of this chapter are organized in the manuscripts:

- Terebus, Anna, Youfang Cao, and Jie Liang. "Sensitivities of Regulation Intensities in Feed-Forward Loops with Multistability." 2019 41st Annual International Conference of the IEEE Engineering in Medicine and Biology Society. IEEE, 2019.

- Terebus, Anna, Youfang Cao, and Jie Liang. "Network Motif of Feed-Forward Loop with multistability is a mediator of a Phenotypic Switch in Cells", manuscript.

Chapter 4 is devoted to the development of the new concept of probability velocity and flux. I introduced new definitions of derivative and differential on the discrete space for chemical reactions models, and the continuity equation for the probability on the discrete space. I defined two types of flux, reactional flux and species flux. Whereas the reactional flux satisfies continuity equation for probability, the species flux quantify the probability flux in every microstate in direction of every species. I showed how such definition of flux quantifies the flux for the birth and death process, bi-stable Schlogl process, and oscillatory Schnakenberg process. This chapter is based on publication:

- Terebus, Anna, Chun Liu, and Jie Liang. "Discrete flux and velocity fields of probability and their global maps in reaction systems." The Journal of chemical physics 149.18 (2018): 185101.

In **Chapter 5**, I showed the differences between the universal flux and well known model of the Fokker-Planck probability flux, as well as the Liouville flux model developed in this work, which was suggested by Dr. Chun Liu. Using the toggle-switch model, as an example, I showed that the differences between three types of flux. The results of this chapter are organized in a manuscript:

- Terebus, Anna, Chun Liu, and Jie Liang. "Discrete and Continuous Models of Probability Flux of Switching Dynamics: A Case Study of Toggle-Switch System." manuscript

I further show examples of the universal probability flux and velocity fields for different biological examples. Firstly I discuss the phenomena of oscillations in toggle switch loop.

Further, I study the problems of gene duplication in the toggle switch genetic network motif using the probability velocity and flux fields.

Chapter 6 summarizes the results of the thesis and provides with the directions for future research.

CHAPTER 2

ERROR AND ERROR BOUND FOR ACCURATE SOLUTION OF DISCRETE CHEMICAL MASTER EQUATION.

2.1   Introduction

Adapted by permission from Springer: Bulletin of mathematical biology, Cao, Y., Terebus, A. and Liang, J. State space truncation with quantified errors for accurate solutions to discrete chemical master equation, 78(4), pp.617-661, Copyright 2016. DOI:10.1007/s11538-016-0149-1.

Gene regulatory networks depict how interactions among molecules regulate expression of gene in a cell. These interactions dictate the levels of messenger RNAs (mRNAs) as well as production of proteins. They play important roles in biological processes such as cell fate determination [18, 55], signal transduction [56, 57], and metabolic regulations [58, 59]. When genes, transcription factors, signaling molecules, and regulatory proteins are in small quantities, stochasticity plays important roles [7, 16, 60–65]. The discrete Chemical Master Equation (dCME) provides a fundamental framework for fully characterizing mesoscopic stochastic processes in a well mixed system [8, 17, 66–69]. The steady state and time-evolving probability landscapes over discrete states governed by the dCME provide detailed information of these dynamic stochastic processes. However solution of the dCME remains difficult, as analytical solution is possible only for a few very simple cases [65, 70–72].

The dCME can be approximated using the FokkerPlanck equation and the chemical Langevin equation [36, 37, 39, 41]. However these approximations are not valid when copy numbers of molecular species are small [30, 73–75], as they may not provide a full account of the stochasticity of the system [8, 30, 73–76]. For example, Fokker-Planck model fails to capture multistability in gene regulation networks with slow switching between the ON and the OFF states [30]. A widely used approach to study stochasticity is that of stochastic simulation algorithm (SSA) [8]. It generates reaction trajectories following the underlying dCME. It is therefore inefficient for sampling biologically critical rare events that often occur in stiff multiscale reaction networks, in addition, assessment of convergence of simulation trajectories is also difficult [10, 77, 78].

Directly solving the dCME offers another attractive approach. By computing the probability landscape of a stochastic network numerically, its properties, such as those involving rare events, can be studied accurately in details. The finite state projection (FSP) method is among several methods that have been developed to solve dCME directly [17, 18, 66, 67, 79–81]. The FSP is based on a truncated projection of the state space and uses numerical techniques to compute the time-evolving probability landscapes, which are solutions to the dCME [66, 82, 83]. Although the error due to state space truncation can be calculated for the time-evolving probability landscape [66], the use of an absorbing boundary, to which all truncated states are projected, will lead to the accumulation of errors as time proceeds, and eventually trap all probability mass. The FSP method was designed to study transient behavior of stochastic networks, and is not well suited to study the long-term behavior and the steady state probability landscape of a network.

State-space of the open systems is enormous, therefore all computational methods require its truncation. However, it is unclear how accurate is the probability landscape computed on a truncated state space. For example, a synthesis reaction cannot happen on the boundary of truncated state space, if its product is not enumerated. Furthermore, it is unclear how to minimize truncation errors, thus limiting the scope of applications of direct methods such as the fb-dCME method [17, 18].

2.2   Molecular Equivalence Group

We can partition reactions into different Molecular Equivalence (MEG), each of which contains reactions sharing the common species, whose stoichiometries are non-zero. When the particular MEG is an open system, *i.e.*, containing synthesis and degradation reactions, finite buffer of virtual molecules is assigned to the subnetwork to limit the total copy number of species that can be synthesized [69, 84, 85]. Assume that the system of the reactions has q MEGs, therefore, we have to assign q buffers: $\mathbf{B} = (B_1, \cdots, B_q)$ to this system.

2.3   State Space Aggregation

Consider one MEG of stochastic network. The state space of this system is generally of infinite size $\Omega^{(\infty)}$, which can be partitioned into disjoint groups of subsets $\tilde{\Omega}^{(\infty)} \equiv \{\mathcal{G}_0, \mathcal{G}_1, \cdots, \mathcal{G}_N, \cdots\}$, where states in each aggregated subset $\mathcal{G}_s$ have exactly the same s total copies of equivalent elementary molecular species of the MEG. The total steady state probability $\tilde{\pi}_s^{(\infty)}$ on microstates in each group $\mathcal{G}_s$ can then be written as:

$$\tilde{p}_s^{(\infty)} \equiv \sum_{\mathbf{x} \in \mathcal{G}_s} p^{(\infty)}(\mathbf{x}) = \sum_{\mathbf{x} \in \mathcal{G}_s} \pi^{(\infty)}(\mathbf{x}, t = \infty). \tag{2.1}$$

In continuous time Markov model of mesoscopic systems, reactions occur instantaneously, and the synthesis and degradation reactions always generate or destroy one molecule at a time. This also applies to oligomers, which are assumed to form only upon association of monomers already synthesized, and dissociate into monomers first before full degradation. The re-constructed matrix $\tilde{\mathbf{A}}$ is thus a tri-diagonal block matrix, *i.e.*, $\mathbf{A}_{i,j}$ is all 0s if $|i-j| > 1$ [69]. Moreover, synthesis reactions always appear as lower blocks $\mathbf{A}_{i+1,i}$, and degradation reactions always as upper blocks $\mathbf{A}_{i,i+1}$. Diagonal blocks $\mathbf{A}_{i,i}$ contains all coupling reactions that do not alter the net number of synthesized molecules. Note that every $\mathbf{A}_{i+1,i}$ block and $\mathbf{A}_{i,i+1}$ block only includes synthesis and degradation reactions associated with the current MEG. We assume the other MEGs do not alter the total net copy number of molecular species in the group.

For such aggregated state space, the aggregated discrete Chemical Master Equation, can be written as follows:

$$\frac{dp^{(\infty)}(\mathcal{G}_0, t)}{dt} = \frac{d\sum_{\in\mathcal{G}_0} p(, t)}{dt} = \left(1^T \mathbf{A}_{0,0}\right) \tilde{\mathbf{p}}^{(\infty)}(\mathcal{G}_0, t) + \left(1^T \mathbf{A}_{0,1}\right) \tilde{\mathbf{p}}^{(\infty)}(\mathcal{G}_1, t),$$

$$\frac{dp^{(\infty)}(\mathcal{G}_i, t)}{dt} = \frac{d\sum_{\in\mathcal{G}_i} p(, t)}{dt} = \left(1^T \mathbf{A}_{i,i-1}\right) \tilde{\mathbf{p}}^{(\infty)}(\mathcal{G}_{i-1}, t) + \left(1^T \mathbf{A}_{i,i}\right) \tilde{\mathbf{p}}^{(\infty)}(\mathcal{G}_i, t) \qquad (2.2)$$

$$+ \left(1^T \mathbf{A}_{i,i+1}\right) \tilde{\mathbf{p}}^{(\infty)}(\mathcal{G}_{i+1}, t), \text{for } i = 1, \cdots, \infty.$$

We obtained it by summing up the master equations over all microstates in each group $\mathcal{G}_i$ and obtain a separate aggregated equation for each group, as the re-ordered matrix $\tilde{\mathbf{A}}$ is a block tri-diagonal matrix.

2.4 Steady State Probability Distribution on the Aggregated State Space

We consider the problem of calculating the steady state process controlled by a pair of "synthesis" and "degradation" transitions between aggregated states associated with different net copy number of the MEG [69, 84, 85]. This turns out to be a simple birth-death process. It takes the form:

$$\emptyset \underset{\beta_{i+1}^{(\infty)}}{\overset{\alpha_i^{(\infty)}}{\rightleftharpoons}} \mathsf{E}, \tag{2.3}$$
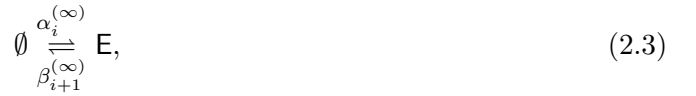
where E represents the elementary molecular species in the MEG, with its copy number the total net copy number of the MEG.

Following the well-known results on analytical solution of the steady state distribution of the birth-death processes [65, 86], the steady state solution for $\tilde{\pi}_i^{(\infty)}$ and $\tilde{\pi}_0^{(\infty)}$ can be written as:

$$\tilde{\pi}_i^{(\infty)} = \prod_{k=0}^{i-1} \frac{\alpha_k^{(\infty)}}{\beta_{k+1}^{(\infty)}} \tilde{\pi}_0^{(\infty)}, \tag{2.4}$$

and

$$\tilde{\pi}_0^{(\infty)} = \frac{1}{1 + \sum_{j=1}^{\infty} \prod_{k=0}^{j-1} \frac{\alpha_k^{(\infty)}}{\beta_{k+1}^{(\infty)}}}. \tag{2.5}$$

2.5 Error of the Truncation

We truncate the state space by fixing the maximum amount of total mass in the MEG. When the maximum total net copy number of the MEG is limited to N, states with a total net copy number larger than N will not be included, resulting in a truncated state space $\Omega^{(N)}$. Those microstates with exactly N total net copies of molecules in the network are the *boundary states*,

because neighboring states with one additional molecule are truncated. The true error for the steady state $Err^{(N)}$ due to truncating states beyond those with N net copies of molecules is the summation of true probabilities over microstates that have been truncated from the original infinite state space:

$$Err^{(N)} = \sum_{\mathbf{x}\in\Omega^{(\infty)},\,\mathbf{x}\notin\Omega^{(N)}} p^{(\infty)}(\mathbf{x}) = 1 - \sum_{\mathbf{x}\in\Omega^{(N)}} p^{(\infty)}(\mathbf{x}). \tag{2.6}$$

2.6   Boundary Probability

Such state space truncation only increases boundary probability:

Theorem The total steady state probability $\pi_i^{(N)}$ of an aggregated state group $\mathcal{G}_i$, for all $i = 0, 1, \cdots, N$, on the truncated state space $\Omega^{(N)}$ with a maximum net molecular copy number N, is greater than or equal to the non-truncated probability $\pi_i^{(\infty)}$ over the same group $\mathcal{G}_i$ obtained using the original state space $\Omega^{(\infty)}$ of infinite size, i.e., $\pi_i^{(\infty)} \le \pi_i^{(N)}$.

We first consider two truncated state spaces $\tilde{\Omega}^{(N)}$ and $\tilde{\Omega}^{(N+1)}$. Following (Equation 2.2), two finite sets of the block chemical master equation can be constructed for these two state spaces. The first set containing N equations is built on the state space $\tilde{\Omega}^{(N)}$.

$$
\begin{aligned}
\frac{dp^{(N)}(\mathcal{G}_0, t)}{dt} &= \left(1^T \mathbf{A}_{0,0}\right) \tilde{\mathbf{p}}^{(N)}(\mathcal{G}_0, t) + \left(1^T \mathbf{A}_{0,1}\right) \tilde{\mathbf{p}}^{(N)}(\mathcal{G}_1, t), \\
\frac{dp^{(N)}(\mathcal{G}_i, t)}{dt} &= \left(1^T \mathbf{A}_{i,i-1}\right) \tilde{\mathbf{p}}^{(N)}(\mathcal{G}_{i-1}, t) + \left(1^T \mathbf{A}_{i,i}\right) \tilde{\mathbf{p}}^{(N)}(\mathcal{G}_i, t) \\
&\quad + \left(1^T \mathbf{A}_{i,i+1}\right) \tilde{\mathbf{p}}^{(N)}(\mathcal{G}_{i+1}, t), \text{ for } i = 1, \cdots, N-1, \\
\frac{dp^{(N)}(\mathcal{G}_N, t)}{dt} &= \left(1^T \mathbf{A}_{N,N-1}\right) \tilde{\mathbf{p}}^{(N)}(\mathcal{G}_{N-1}, t) + \left(1^T \mathbf{A}_{N,N}\right) \tilde{\mathbf{p}}^{(N)}(\mathcal{G}_N, t).
\end{aligned}
\tag{2.7}
$$

The second set is built on the state space $\tilde{\Omega}^{(N+1)}$ containing $N+1$ equations.

$$
\begin{aligned}
\frac{dp^{(N+1)}(\mathcal{G}_0, t)}{dt} &= \left(1^T \mathbf{A}_{0,0}\right) \tilde{\mathbf{p}}^{(N+1)}(\mathcal{G}_0, t) + \left(1^T \mathbf{A}_{0,1}\right) \tilde{\mathbf{p}}^{(N+1)}(\mathcal{G}_1, t), \\
\frac{dp^{(N+1)}(\mathcal{G}_i, t)}{dt} &= \left(1^T \mathbf{A}_{i,i-1}\right) \tilde{\mathbf{p}}^{(N+1)}(\mathcal{G}_{i-1}, t) + \left(1^T \mathbf{A}_{i,i}\right) \tilde{\mathbf{p}}^{(N+1)}(\mathcal{G}_i, t) \\
&\quad + \left(1^T \mathbf{A}_{i,i+1}\right) \tilde{\mathbf{p}}^{(N+1)}(\mathcal{G}_{i+1}, t), \text{ for } i = 1, \cdots, N-1, \\
\frac{dp^{(N+1)}(\mathcal{G}_N, t)}{dt} &= \left(1^T \mathbf{A}_{N,N-1}\right) \tilde{\mathbf{p}}^{(N+1)}(\mathcal{G}_{N-1}, t) + \left(1^T \mathbf{A}_{N,N}\right) \tilde{\mathbf{p}}^{(N+1)}(\mathcal{G}_N, t) \\
&\quad + \left(1^T \mathbf{A}_{N,N+1}\right) \tilde{\mathbf{p}}^{(N+1)}(\mathcal{G}_{N+1}, t), \\
\frac{dp^{(N+1)}(\mathcal{G}_{N+1}, t)}{dt} &= \left(1^T \mathbf{A}_{N+1,N}\right) \tilde{\mathbf{p}}^{(N+1)}(\mathcal{G}_N, t) + \left(1^T \mathbf{A}_{N+1,N+1}\right) \tilde{\mathbf{p}}^{(N+1)}(\mathcal{G}_{N+1}, t).
\end{aligned}
\tag{2.8}
$$

At steady state, the left-hand side of the equations are zeros. For the first N equations, the corresponding block matrices are the same for both state spaces $\tilde{\Omega}^{(N)}$ and $\tilde{\Omega}^{(N+1)}$. We can then subtract the right-hand side of (Equation 2.8) from (Equation 2.7) and obtain the following steady state equations:

$$
1^T \mathbf{A}_{0,0} \Delta \pi_0 + 1^T \mathbf{A}_{0,1} \Delta \pi_1 = 0,
$$

$$
1^T \mathbf{A}_{i,i-1} \Delta \pi_{i-1} + 1^T \mathbf{A}_{i,i} \Delta \pi_i + 1 \mathbf{A}_{i,i+1} \Delta \pi_{i+1} = 0,
\tag{2.9}
$$

$$
\text{for } i = 1, \cdots, N-1,
$$

where $\Delta \pi_i = \pi_i^{(N)} - \pi_i^{(N+1)}$ is the steady state probability difference between the state group $\mathcal{G}_i$ in the dCME on $\tilde{\Omega}^{(N)}$ and $\tilde{\Omega}^{(N+1)}$. However, the block sub-matrix $\mathbf{A}_{N,N}$ of the boundary group $\mathcal{G}_N$ is different between the two state spaces. From the construction of the aggregated

dCME and buffer concept matrix $\tilde{\mathbf{A}}$, columns of the full matrices $\tilde{\mathbf{A}}^{(N+1)}$ over $\tilde{\Omega}^{(N+1)}$ and $\tilde{\mathbf{A}}^N$ over $\tilde{\Omega}^N$ all sum to 0 [84]. We use $\mathbf{A}_{i,j}^{(N)}$ to denote the block sub-matrix of the group $\mathcal{G}_N$ for the state space $\tilde{\Omega}^{(N)}$, and use $\mathbf{A}_{i,j}^{(N+1)}$ to denote the corresponding block sub-matrix for the state space $\tilde{\Omega}^{(N+1)}$. From the N-th line of the truncated version of Eqn (**??**), we have $1^T \mathbf{A}_{N-1,N}^{(N+1)} + 1^T \mathbf{A}_{N,N}^{(N+1)} + 1^T \mathbf{A}_{N+1,N}^{(N+1)} = 0$ for $\tilde{\Omega}^{(N+1)}$ and $1^T \mathbf{A}_{N-1,N}^{(N)} + 1^T \mathbf{A}_{N,N}^{(N)} = 0$ for $\tilde{\Omega}^{(N)}$. Since $\mathbf{A}_{N-1,N}^{(N)} = \mathbf{A}_{N-1,N}^{(N+1)}$, we have the following property

$$1^T \mathbf{A}_{N,N}^{(N+1)} = 1^T \mathbf{A}_{N,N}^{(N)} - 1^T \mathbf{A}_{N+1,N}^{(N+1)}, \tag{2.10}$$

We also have

$$1^T \mathbf{A}_{N+1,N+1}^{(N+1)} = -1^T \mathbf{A}_{N,N+1}^{(N+1)}. \tag{2.11}$$

From (Equation 2.7), we have for the steady state the probability of the state group $\mathcal{G}_N$ over the state space $\tilde{\Omega}^{(N)}$ as:

$$1^T \mathbf{A}_{N,N-1}^{(N)} \pi_{N-1}^{(N)} + 1^T \mathbf{A}_{N,N}^{(N)} \pi_N^{(N)} = 0, \tag{2.12}$$

From (Equation 2.8), we have for the steady state the probability of the state group $\mathcal{G}_N$ and $\mathcal{G}_{N+1}$ over the state space $\tilde{\Omega}^{(N+1)}$ as:

$$1^T \mathbf{A}_{N,N-1}^{(N+1)} \pi_{N-1}^{(N+1)} + 1^T \mathbf{A}_{N,N}^{(N+1)} \pi_N^{(N+1)} + 1^T \mathbf{A}_{N,N+1}^{(N+1)} \pi_{N+1}^{(N+1)} = 0, \tag{2.13}$$

and

$$1^T \mathbf{A}_{N+1,N}^{(N+1)} \pi_N^{(N+1)} + 1^T \mathbf{A}_{N+1,N+1}^{(N+1)} \pi_{N+1}^{(N+1)} = 0, \tag{2.14}$$

respectively.

As $\mathbf{A}_{N,N-1}^{(N+1)} = \mathbf{A}_{N,N-1}^{(N)}$, we subtract (Equation 2.13) from (Equation 2.12), and obtain:

$$1^T \mathbf{A}_{N,N-1} \Delta \pi_{N-1} + 1^T \mathbf{A}_{N,N}^{(N)} \pi_N^{(N)} - 1^T \mathbf{A}_{N,N}^{(N+1)} \pi_N^{(N+1)} - 1^T \mathbf{A}_{N,N+1}^{(N+1)} \pi_{N+1}^{(N+1)} = 0.$$

It can be re-written by applying the matrix property of (Equation 2.10) as:

$$1^T \mathbf{A}_{N,N-1} \Delta \pi_{N-1} + 1^T \mathbf{A}_{N,N}^{(N)} \Delta \pi_N + 1^T \mathbf{A}_{N+1,N}^{(N+1)} \pi_N^{(N+1)} - 1^T \mathbf{A}_{N,N+1}^{(N+1)} \pi_{N+1}^{(N+1)} = 0.$$

By using the matrix property in (Equation 2.11), we can further re-write it as:

$$1^T \mathbf{A}_{N,N-1} \Delta \pi_{N-1} + 1^T \mathbf{A}_{N,N}^{(N)} \Delta \pi_N + 1^T \mathbf{A}_{N+1,N}^{(N+1)} \pi_N^{(N+1)} + 1^T \mathbf{A}_{N+1,N+1}^{(N+1)} \pi_{N+1}^{(N+1)} = 0.$$

From (Equation 2.14), the last two terms sum to 0. Therefore, we obtain the $(N+1)$-st equation of the steady state probability difference as:

$$1^T \mathbf{A}_{N,N-1} \Delta \pi_{N-1} + 1^T \mathbf{A}_{N,N}^{(N)} \Delta \pi_N = 0.$$

As probability vector solution to (Equation 1.1) has non-negative elements, this equivalence implies that all elements in each $\Delta\pi_i$ have the same sign. As the total steady state probability mass in both state spaces sum up to 1,

$$\sum_{i=1}^{N} \tilde{\pi}_i^{(N)} = \sum_{i=1}^{N+1} \tilde{\pi}_i^{(N+1)} = 1,$$

we therefore know that the total probability differences is non-negative:

$$\sum_{i=1}^{N} \Delta\tilde{\pi}_i = \sum_{i=1}^{N} \tilde{\pi}_i^{(N)} - \sum_{i=1}^{N} \tilde{\pi}_i^{(N+1)} = 1 - (1 - \tilde{\pi}_{N+1}^{(N+1)}) = \tilde{\pi}_{N+1}^{(N+1)} \geq 0.$$

Therefore, the probability difference of each individual $\mathcal{G}_i$ between two state spaces must be non-negative:

$$\Delta\tilde{\pi}_i = \tilde{\pi}_i^{(N)} - \tilde{\pi}_i^{(N+1)} \geq 0, \quad i = 0, 1, \cdots, N.$$

This can be generalized. As N increases to infinity, we have:

$$\tilde{\pi}_i^{(N)} \geq \tilde{\pi}_i^{(N+1)} \geq \cdots \geq \tilde{\pi}_i^{(\infty)}, \quad i = 0, 1, \cdots, N.$$

This proves the theorem.

2.7 Error Bound

It can also be shown that if N is sufficiently large, the true error $Err^{(\infty)}$ is bounded by the true boundary probability $\pi_N^{(\infty)}$ times a constant.

Assymptotic Convergence of the Error For a truncated state space with a maximum net molecular copy number N in the network, the true error $Err^{(N)}$ follows the inequality below when N increases to infinity:

$$Err^{(N)} \leq \frac{\frac{\alpha_M^{(\infty)}}{\beta_{M+1}^{(\infty)}}}{1 - \frac{\alpha_M^{(\infty)}}{\beta_{M+1}^{(\infty)}}} \tilde{\pi}_N^{(\infty)}, \tag{2.15}$$

where M is an integer selected from $N, \cdots, \infty$ to satisfy $\frac{\alpha_M^{(\infty)}}{\beta_{M+1}^{(\infty)}} = \sup\limits_{k \geq N} \left\{ \frac{\alpha_k^{(\infty)}}{\beta_{k+1}^{(\infty)}} \right\}$.

Proof. From (Equation 2.6), we can first derive an explicit expression of the true error $Err^{(N)}$ using the aggregated synthesis and degradation rates $\alpha_k^{(\infty)}$ and $\beta_{k+1}^{(\infty)}$:

$$\begin{aligned} Err^{(N)} &= 1 - \sum_{\mathbf{x} \in \Omega^{(N)}} \pi^{(\infty)}(\mathbf{x}) = 1 - \sum_{i=0}^{N} 1^T \tilde{\pi}^{(\infty)}(\mathcal{G}_i) = 1 - \tilde{\pi}_0^{(\infty)}(1 + \sum_{j=1}^{N} \prod_{k=0}^{j-1} \frac{\alpha_k^{(\infty)}}{\beta_{k+1}^{(\infty)}}) \\ &= 1 - \frac{1 + \sum_{j=1}^{N} \prod_{k=0}^{j-1} \frac{\alpha_k^{(\infty)}}{\beta_{k+1}^{(\infty)}}}{1 + \sum_{j=1}^{\infty} \prod_{k=0}^{j-1} \frac{\alpha_k^{(\infty)}}{\beta_{k+1}^{(\infty)}}} = \frac{\sum_{j=N+1}^{\infty} \prod_{k=0}^{j-1} \frac{\alpha_k^{(\infty)}}{\beta_{k+1}^{(\infty)}}}{1 + \sum_{j=1}^{\infty} \prod_{k=0}^{j-1} \frac{\alpha_k^{(\infty)}}{\beta_{k+1}^{(\infty)}}} \end{aligned} \tag{2.16}$$

From (Equation 2.16), (Equation 2.6), we have:

$$\begin{aligned} \frac{Err^{(N)}}{\tilde{\pi}_N^{(\infty)}} &= \frac{\sum_{j=N+1}^{\infty} \prod_{k=0}^{j-1} \frac{\alpha_k^{(\infty)}}{\beta_{k+1}^{(\infty)}}}{\prod_{k=0}^{N-1} \frac{\alpha_k^{(\infty)}}{\beta_{k+1}^{(\infty)}}} = \frac{(\prod_{k=0}^{N-1} \frac{\alpha_k^{(\infty)}}{\beta_{k+1}^{(\infty)}})(\sum_{j=N+1}^{\infty} \prod_{k=N}^{j-1} \frac{\alpha_k^{(\infty)}}{\beta_{k+1}^{(\infty)}})}{\prod_{k=0}^{N-1} \frac{\alpha_k^{(\infty)}}{\beta_{k+1}^{(\infty)}}} \\ &= \sum_{j=N+1}^{\infty} \prod_{k=N}^{j-1} \frac{\alpha_k^{(\infty)}}{\beta_{k+1}^{(\infty)}} \leq \sum_{j=N+1}^{\infty} \left[\sup_{k \geq N} \left\{ \frac{\alpha_k^{(\infty)}}{\beta_{k+1}^{(\infty)}} \right\} \right]^{j-N} = \sum_{j=1}^{\infty} \left[\sup_{k \geq N} \left\{ \frac{\alpha_k^{(\infty)}}{\beta_{k+1}^{(\infty)}} \right\} \right]^{j}, \end{aligned} \tag{2.17}$$

When N is sufficiently large and there is no peak of the probability landscape for the state of the size larger than N, $\sup\limits_{k \geq N} \left\{ \frac{\alpha_k^{(\infty)}}{\beta_{k+1}^{(\infty)}} \right\} < 1$. The terms in the infinite series $\sum_{j=1}^{\infty} \left[\sup\limits_{k \geq N} \left\{ \frac{\alpha_k^{(\infty)}}{\beta_{k+1}^{(\infty)}} \right\} \right]^j$ then forms a converging geometric series. Therefore, we have

$$\sum_{j=1}^{\infty} \left[\sup_{k \geq N} \left\{ \frac{\alpha_k^{(\infty)}}{\beta_{k+1}^{(\infty)}} \right\} \right]^j = \frac{\sup\limits_{k \geq N} \left\{ \frac{\alpha_k^{(\infty)}}{\beta_{k+1}^{(\infty)}} \right\}}{1 - \sup\limits_{k \geq N} \left\{ \frac{\alpha_k^{(\infty)}}{\beta_{k+1}^{(\infty)}} \right\}},$$

and the following inequality holds:

$$\lim_{N \to \infty} \frac{Err^{(N)}}{\bar{\pi}_N^{(\infty)}} \leq \lim_{N \to \infty} \frac{\sup\limits_{k \geq N} \left\{ \frac{\alpha_k^{(\infty)}}{\beta_{k+1}^{(\infty)}} \right\}}{1 - \sup\limits_{k \geq N} \left\{ \frac{\alpha_k^{(\infty)}}{\beta_{k+1}^{(\infty)}} \right\}}.$$

Let $M \in \{N, \cdots, \infty\}$ be the integer such that $\frac{\alpha_M^{(\infty)}}{\beta_{M+1}^{(\infty)}} = \sup\limits_{k \geq N} \left\{ \frac{\alpha_k^{(\infty)}}{\beta_{k+1}^{(\infty)}} \right\}$, we have the following inequality equivalent to Inequality (Equation 2.15):

$$\lim_{N \to \infty} \frac{Err^{(N)}}{\bar{\pi}_N^{(\infty)}} \leq \lim_{N \to \infty} \frac{\frac{\alpha_M^{(\infty)}}{\beta_{M+1}^{(\infty)}}}{1 - \frac{\alpha_M^{(\infty)}}{\beta_{M+1}^{(\infty)}}}.$$

This proves asymptotic convergence of the boundary probability to the true error.

Therefore the boundary probability converges to the true error, and the boundary probability for the truncated state space $\Omega^{(N)}$, which is even larger, that boundary probability on the full state space, converges to the true error.

We assign the separate buffer for each MEG, and the minimal buffer size can be determined by comparing the error estimate of the buffer to the desired error tolerance. If the estimated error is larger that the error tolerance, the buffer size needs to be increased. Otherwise, the buffer size can be reduced to save memory space.

2.8   Theoretical Error Bound

In principle, one does not know buffer capacity is needed to find probability within particular error bound. For that we derived the theoretical error bound for every buffer. We first found the upper bound for the synthesis reactions $(\overline{\alpha_i})$ and the lower bound of degradation rate $(\underline{\beta_i})$ in i-th MEG.

The theoretical error bound of the system when the size of the state space is limited to $N+1$ states $(0, 1, ...N)$ is then determined by the probability π_N^N of the $(N+1)$-th state when the buffer is exhausted, which can be calculated exactly as:

$$\pi_N^{(N)} = \frac{\prod_{j=0}^{N} \frac{\overline{\alpha}_{j-1}}{\underline{\beta}_j}}{1 + \sum_{i=1}^{N} \prod_{j=1}^{i} \frac{\overline{\alpha}_{j-1}}{\underline{\beta}_j}}.$$

Computation for the error requires multiplication of large numbers in numerator. For the large N such product may exceed the size of the numerical type of the variable used. We can avoid this problem by computing the error of each buffer size recursively from the equation:

$$\pi_0^{(1)} = 1, \pi_i^{(i+1)} = 1 \bigg/ 1 + \frac{\overline{\alpha}_{i-1}}{\underline{\beta}_i \pi_{i-1}^{(i)}}. \tag{2.18}$$

We use the example of Phage Lambda Bistable Epigenetic Switch to illustrate how the system can be separated into MEGs and how the errors can be computed.

2.9   Phage Lambda Bistable Epigenetic Switch

The bistable epigenetic switch for lysogenic maintenance and lytic induction in phage lambda is one of the well-parameterized realistic gene regulatory system. The efficiency and stability of the switch have been extensively studied [87–89]. Here we characterize the truncation error to the dCME solutions of the reaction network adapted from Cao *et al.* [90]. The network consists of 11 different species and 50 different reactions. The detailed reaction schemes and rate constants are shown in Table I,Table II,Table III.

The network can be partitioned into two MEGs. The MEG$_1$ consists of the dimer of CI protein $CI2$ and all complexes of operator sites bounded with $CI2$. The MEG$_2$ consists of the dimer of Cro protein $Cro2$ and all complexes of operator sites bounded with $Cro2$.

To numerically demonstrate assymptotic convergence of errors, we compute the true error of the steady state solution to the dCME using sufficiently large sizes of $MEG_1 = 80$ and $MEG_2 = 38$, which gives negligible truncation error, with infinitesimally small boundary probabilities 6.96×10^{-31} for MEG_1 and 3.95×10^{-32} for MEG_2. Solution obtained using these MEGs is therefore considered to be exact. With this exact steady state probability landscape, the true truncation error $Err^{(N)}$ at smaller sizes of MEG_1 and MEG_2 can both be computed using (Equation 2.6) (Figure 2A and B, blue dashed lines and crosses). The corresponding boundary probabilities $\pi_N^{(\infty)}$ or computed error are computed from the exact steady state probability

landscape for both MEG_1 (Figure 2A, green dashed line and circles) and MEG_2 (Figure 2B, green dashed line and circles).

Our results show that the true error $Err^{(N)}$ (Figure 2A and B, blue dashed lines and crosses) is bounded by the computed boundary probability $\pi_N^{(\infty)}$ (Figure 2A and B, green dashed lines and circles)

when the size of the MEG is sufficiently large. The insets in Figure 2A and B show the ratios of the true errors to the computed errors at different sizes of the MEG, and the grey straight lines mark the ratio one. The computed errors are larger than the true errors when the black line is below the grey straight line (Figure 2A and B, insets). In this example, the computed boundary probability is greater than the true error when $MEG_1 \geq 24$ and $MEG_2 \geq 3$.

To examine *a priori* estimated upper bounds for the truncation errors in MEG_1 and MEG_2, we assign the values of $\overline{\alpha}_i = k_{s1CI_2}$ and $\underline{\beta}_{(i+1)} = [(i+1) - 3] \cdot k_{dCI_2}$ for the MEG_1, where the subscript $(i+1)$ is the total copy number of species $CI2$ in the system. The subtraction of 3 is necessary because up to 3 copies of $CI2$ can be protected from degradation by binding to operator sites $OR1$, $OR2$, and $OR3$. Similarly, we have $\overline{\alpha}_i = k_{sCro_2}$ and $\underline{\beta}_{i+1} = [(i+1) - 3] \cdot k_{dCro_2}$. We compute the *a priori* estimated upper bounds of errors for different truncations of MEG_1 and MEG_2 using (Equation 2.18) (Figure 2A and B, red solid lines). The true truncation errors and the *a priori* estimated error bounds of MEG_1 and MEG_2 all decrease monotonically with increasing MEG sizes (Figure 2A and B). The computed errors also monotonically decrease when the MEG sizes are larger than 13 for MEG_1 and 4 for MEG_2. For both MEGs, the *a*

priori estimated error bounds are larger than computed errors at all MEG sizes. They are also larger than the true errors when the MEG sizes are sufficiently large.

The probability landscape projected on the MEGs increase after state space truncation. We first compute the steady state probability landscapes of $CI2$ obtained by truncating MEG_1 at different sizes ranging from 0 to 80 while MEG_2 is fixed at 38 (Figure 2C). The results are compared with the exact steady state landscape computed using $MEG_1 = 80$ and $MEG_2 = 38$ (Figure 2C, red line). We then also similarly examine the steady state probability landscapes of $Cro2$ obtained by truncating at different sizes of MEG_2 from 0 to 38 while MEG_1 is fixed at 80 (Figure 2D).

Our results show clearly that all probabilities in the landscapes increase when more states are truncated at smaller MEG sizes (Figure 2C and D). The probability landscapes computed using larger sizes of MEGs (*e.g.*, $MEG_1 = 30$, Figure 2C, yellow line and $MEG_2 = 8$, Figure 2D, yellow line) are approaching the exact landscape (Figure 2C and D, red line). The probability landscapes obtained using smaller MEGs deviate significantly from the exact probability landscape. The smaller the MEG size, the more significant the deviation is.

We further examine how the probability landscape projected on one MEG increase with state space truncation at another MEG. We first compare the projected steady state probability landscapes on $CI2$ obtained by truncating MEG_2 at different sizes ranging from 0 to 38 while MEG_1 is fixed at 80 (Figure 2E). We compare the results with the exact steady state landscape (Figure 2E, red line). We also similarly examine the projected steady state proba-

bility landscapes of $Cro2$ obtained by truncating at different sizes of MEG_1 ranging from 0 to 80 while MEG_2 is fixed at 38 (Figure 2F).

Our results show that all probabilities on the landscapes of MEG_1 (MEG_2) increase when the state space is truncated at MEG_2 (MEG_1) (Figure 2E and F). The probability landscapes computed using larger sizes of MEGs (*e.g.*, $MEG_2 = 8$ in Figure 2E, yellow line and $MEG_1 = 30$ in Figure 2F, yellow line) are approaching the exact landscape using $MEG_1 = 80$ and $MEG_2 = 38$ (Figure 2E and F, red line). However, the probability landscapes using smaller MEGs significantly deviate from the exact probability landscape. The smaller the MEG size, the more significant the deviation is.

2.10   Conclusions

Solving the discrete chemical master equation (dCME) is of fundamental importance for studying stochasticity in reaction networks. The main challenges are the discrete nature of the states and the difficulty in enumerating these states, as the size of the state space expands rapidly when the network becomes more complex. This study addresses a key issue in obtaining direct solution to the dCME, including pre-estimation of the size of the system for a certain error threshold and computing the errors of the solution. As state space truncation is inevitable, such quantification of the errors of such truncations is very important. The proven facts of state space truncation could be used for other truncations methods with reflective boundary, with buffer concept, and allow control the error for the truncation. Developed method also allows direct computation of the distribution of first passage time, an important problem in studying rare events in biological networks currently relies heavily on sampling techniques.
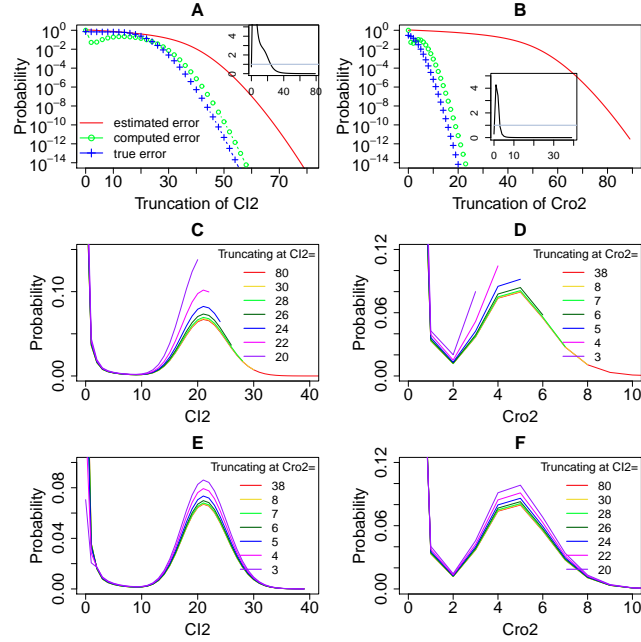
Figure 2. Error quantification and comparisons for the phage lambda bistable epigenetic switch model. (A) and (B): The *a priori* estimated error (red solid lines), the computed error (green lines and circles), and the true error (blue lines and crosses) of the steady state probability landscapes of CI and Cro dimers at different sizes of truncations. The insets in (A) and (B) show the ratio of the true errors to the computed errors at different sizes of the MEG, and the grey straight line marks the ratio one. The computed errors are larger than the true errors when the black line is below the grey straight line. (C) and (D): The steady state probability landscapes of CI and Cro dimers solved using different truncations of net molecular number in the MEG_1 and MEG_2, respectively. Note that probability distributions end at where truncation occurs. The probabilities in the landscapes are significantly inflated when truncating the state space at smaller net molecular numbers of the corresponding MEG. (E) and (F): The steady state probability landscapes of CI and Cro dimers solved using different truncations of net molecular number in the MEG_2 and MEG_1, respectively. The probabilities in the landscapes are also significantly inflated when truncating the state space at smaller net molecular numbers of the opposite MEG.

TABLE I

Reaction scheme and rate constants in phage lambda epigenetic switch mode. We use $CORn$ denotes Cro_2 bound operator site ORn, $RORn$ denotes CI_2 bound ORn, where n can be 1, 2, and 3. Note that molecular species enclosed in parenthesis are those whose presence is required for the specific reactions to occur, but their copy numbers do not influence the transition rates between microstates.

Reactions	Rate constants
Synthesis reactions [87, 91–93]	
$\emptyset + (OR3 + OR2) \rightarrow CI_2 + (OR3 + OR2)$	$k_{sCI_2} = 0.0069/s$
$\emptyset + (OR3 + COR2) \rightarrow CI_2 + (OR3 + COR2)$	$k_{sCI_2} = 0.0069/s$
$\emptyset + (OR3 + ROR2) \rightarrow CI_2 + (OR3 + ROR2)$	$k_{s1CI_2} = 0.069/s$
$\emptyset + (OR1 + OR2) \rightarrow Cro_2 + (OR1 + OR2)$	$k_{sCro_2} = 0.0929/s$
Degradation reactions [87, 94]	
$CI_2 \rightarrow \emptyset$	$k_{dCI_2} = 0.0026/s$
$Cro_2 \rightarrow \emptyset$	$k_{dCro_2} = 0.0025/s$
Association rate of binding reactions [95]	
$CI_2 + OR1 \rightarrow ROR1$	$k_{bOR1CI_2} = 0.021/s$
$CI_2 + OR2 \rightarrow ROR2$	$k_{bOR2CI_2} = 0.021/s$
$CI_2 + OR3 \rightarrow ROR3$	$k_{bOR3CI_2} = 0.021/s$
$Cro_2 + OR1 \rightarrow COR1$	$k_{bOR1Cro_2} = 0.021/s$
$Cro_2 + OR2 \rightarrow COR2$	$k_{bOR2Cro_2} = 0.021/s$
$Cro_2 + OR3 \rightarrow COR3$	$k_{bOR3Cro_2} = 0.021/s$
Dissociation reactions - CI_2 dissociation from OR1	
$ROR1 + (OR2) \rightarrow CI_2 + OR1 + (OR2)$	$0.00898/s$
$ROR1 + (ROR2 + OR3) \rightarrow CI_2 + OR1 + (ROR2 + OR3)$	$0.00011/s$

TABLE II

Reaction scheme and rate constants in phage lambda epigenetic switch mode. Continued.

Reactions	Rate constants
Dissociation reactions - CI_2 dissociation from OR1 (continued)	
$ROR1 + (ROR2 + ROR3) \rightarrow CI_2 + OR1 + (ROR2 + ROR3)$	$0.01242/s$
$ROR1 + (ROR2 + COR3) \rightarrow CI_2 + OR1 + (ROR2 + COR3)$	$0.00011/s$
$ROR1 + (COR2) \rightarrow CI_2 + OR1 + (COR2)$	$0.00898/s$
Dissociation reactions - CI_2 dissociation from OR2	
$ROR2 + (OR1 + OR3) \rightarrow CI_2 + OR2 + (OR1 + OR3)$	$0.2297/s$
$ROR2 + (ROR1 + OR3) \rightarrow CI_2 + OR2 + (ROR1 + OR3)$	$0.0029/s$
$ROR2 + (OR1 + ROR3) \rightarrow CI_2 + OR2 + (OR1 + ROR3)$	$0.0021/s$
$ROR2 + (ROR1 + ROR3) \rightarrow CI_2 + OR2 + (ROR1 + ROR3)$	$0.0029/s$
$ROR2 + (COR1 + OR3) \rightarrow CI_2 + OR2 + (COR1 + OR3)$	$0.2297/s$
$ROR2 + (OR1 + COR3) \rightarrow CI_2 + OR2 + (OR1 + COR3)$	$0.2297/s$
$ROR2 + (COR1 + COR3) \rightarrow CI_2 + OR2 + (COR1 + COR3)$	$0.2297/s$
$ROR2 + (ROR1 + COR3) \rightarrow CI_2 + OR2 + (ROR1 + COR3)$	$0.0029/s$
$ROR2 + (COR1 + ROR3) \rightarrow CI_2 + OR2 + (COR1 + ROR3)$	$0.0021/s$
Dissociation reactions - CI dissociation from OR3	
$ROR3 + (OR2) \rightarrow CI_2 + OR3 + (OR2)$	$1.13/s$
$ROR3 + (ROR2 + OR1) \rightarrow CI_2 + OR3 + (ROR2 + OR1)$	$0.0106/s$
$ROR3 + (ROR2 + ROR1) \rightarrow CI_2 + OR3 + (ROR2 + ROR1)$	$0.0106/s$
$ROR3 + (ROR2 + COR1) \rightarrow CI_2 + OR3 + (ROR2 + COR1)$	$0.0106/s$
$ROR3 + (COR2) \rightarrow CI_2 + OR3 + (COR2)$	$1.13/s$

TABLE III

Reaction scheme and rate constants in phage lambda epigenetic switch mode. Continued.

Reactions	Rate constants
Dissociation reactions - Cro dissociation from OR1	
$COR1 + (OR2) \rightarrow Cro_2 + OR1 + (OR2)$	$0.0202/s$
$COR1 + (ROR2) \rightarrow Cro_2 + OR1 + (ROR2)$	$0.0202/s$
$COR1 + (COR2 + OR3) \rightarrow Cro_2 + OR1 + (COR2 + OR3)$	$0.0040/s$
$COR1 + (COR2 + ROR3) \rightarrow Cro_2 + OR1 + (COR2 + ROR3)$	$0.0040/s$
$COR1 + (COR2 + COR3) \rightarrow Cro_2 + OR1 + (COR2 + COR3)$	$0.0040/s$
Dissociation reactions - Cro dissociation from OR2	
$COR2 + (OR1 + OR3) \rightarrow Cro_2 + OR2 + (OR1 + OR3)$	$0.1413/s$
$COR2 + (ROR1 + OR3) \rightarrow Cro_2 + OR2 + (ROR1 + OR3)$	$0.1413/s$
$COR2 + (OR1 + ROR3) \rightarrow Cro_2 + OR2 + (OR1 + ROR3)$	$0.1413/s$
$COR2 + (ROR1 + ROR3) \rightarrow Cro_2 + OR2 + (ROR1 + ROR3)$	$0.1413/s$
$COR2 + (COR1 + OR3) \rightarrow Cro_2 + OR2 + (COR1 + OR3)$	$0.0279/s$
$COR2 + (OR1 + COR3) \rightarrow Cro_2 + OR2 + (OR1 + COR3)$	$0.053/s$
$COR2 + (COR1 + COR3) \rightarrow Cro_2 + OR2 + (COR1 + COR3)$	$0.0328/s$
$COR2 + (ROR1 + COR3) \rightarrow Cro_2 + OR2 + (ROR1 + COR3)$	$0.053/s$
$COR2 + (COR1 + ROR3) \rightarrow Cro_2 + OR2 + (COR1 + ROR3)$	$0.0279/s$
Dissociation reactions - Cro dissociation from OR3	
$COR3 + (OR2) \rightarrow Cro_2 + OR3 + (OR2)$	$0.0022/s$
$COR3 + (ROR2) \rightarrow Cro_2 + OR3 + (ROR2)$	$0.0022/s$
$COR3 + (COR2 + OR1) \rightarrow Cro_2 + OR3 + (COR2 + OR1)$	$0.0008/s$
$COR3 + (COR2 + ROR1) \rightarrow Cro_2 + OR3 + (COR2 + ROR1)$	$0.0008/s$
$COR3 + (COR2 + COR1) \rightarrow Cro_2 + OR3 + (COR2 + COR1)$	$0.003/s$

CHAPTER 3

SENSITIVITY OF PARAMETERS AND MULTISTABILITY IN THE FEED-FORWARD LOOP WITH SLOW PROMOTER DYNAMICS

3.1 Introduction

Studying the nature and the mechanisms of phenotypic variabilities of the cells is important for understanding essential biological processes, including bacterial cell fate [18, 96], stem sell differentiation [21, 28], tumor formation [97, 98]. The abundances of different proteins in this cell are key players indicating particular phenotype of the cell. Understanding the nature of change in gene expression levels can provide a valuable insight into understanding of the switching mechanism between different phenotypes [99].

Gene expression levels of mRNA and proteins are governed by gene regulatory networks, the collections of molecular regulators that interact with each other and with other substances in the cell. Quantitative modeling of gene regulatory networks allows to estimate the stable points in proteins abundances at different time moments, as well as equilibrium state of the cell. Current understanding of the origin of multiple stable points for protein concentration resides largely on feedback loops and cooperativity in the gene coregulations [26]. Recent studies suggest origin of phenotypic switch from slow promoter binding creating distinct expression levels with considerable lifetime [27–30]. However the nature and extend of this kind of bistability is not well understood. Derministic methods fail in capturing bistability in gene expression

35

due to slow promoter binding, and stochastic differential equations approaches are ineficient in this case. Furthermore it was shown that for the single gene self-regulation model with certain reaction rate values multistability cannot be captured with Fokker-Planck equation [30]. This phenomena, referred as stochastic multimodality, is usually associated with eucaryotic cells, likely due to remodeling of chromatin structures, and it can be precisely captured with highly accurate stochastic models. Gillespie stochastic simulations methods [7] are challenging capturing rare events and have limitations of assessing the error. Discrete Chemical Master Equation (dCME) provides a fundamental framework for studying stochastic gene regulatory networks. However direct solving of dCME is not always possible due to the enormous state space. In order to address this limitation we use the ACME (Accurate Chemical Master Equation) algorithm [69, 100], which has the advantages of more effective memory usage, rapid estimation of errors, and pre-estimation of buffer size in order to maintain a predefined error-tolerance threshold.

In the chapter we study feed-forward loop (FFL), which is one of the most prevalent in the nature types of network motifs [19]. It occurs much more frequently in biological networks found in nature, compared to randomly generated networks. In addition, it has a well defined functionality. The regulation in feed-forward loop is carried out from the top nodes towards the bottom ones by two regulation paths: the direct regulation from the top input node to the output node, and the indirect regulation from the input to the output through intermediate buffer node. Based on equality of the signs of regulation on the direct and indirect paths, there are two conventionally defined classes of feed forward loops, coherent and incoherent

feed-forward loops correspondingly. As each regulatory link is either up or down regulation, and therefore there are eight types of feed-forward loop in total. FFL is found to be significant in yeast [101], in bacteria [102, 103], and also widely observed in mammals [20, 22, 23].

High abundance of feed-forward loop network motifs in the nature is related to its essential functionality. Indeed, deterministic studies reveal important functional characteristics of feed-forward loop. Feed-forward loops are known to have signal processing functions, such as sign-sensitive acceleration (incoherent), namely speeding up the response time of the target gene expression following stimulus steps in one direction, sign-sensitive delays (coherent loops), pulse generation functions, and cooperativity increase [104]. It is also one of the network motifs capable to maintain robust adaptation [105, 106], and "fold-change" detection [107]. Although deterministic models of feed-forward loops are very well studied, stochastic modeling remains a captivating research field, which can possibly reveal new functions of significant biological importance [108].

High frequency of appearance of feed-forward loop in mammal cell, particularly in stem cell pluripotency networks [20–22], microRNA regulation networks [23–25], and cancer networks [25], suggests importance of feed-forward loop in differentiation. We have explored the role of feed-forward loop network in phenotypic switching in the cell, namely, studied the range of the values of the parameters, which allow this switch to occur, as well as find the number of possible phenotypic states. We have also examined the network parameters, such as regulations intensities, the strength of the input, the speed of binding and unbinding of transcription factors

to genes, and the number of genes involved in order to see how every each of them affects the multistable properties of feed-forward loop.

We further examine the parameters sensitivity of FFLs, a measure of system behavior in response to perturbations of its parameters. It characterizes how changes in the network parameters can affect the network output, for example, at the steady state. Sensitivity analysis helps to understand how network output is sensitive to input, and models parameters, and has been widely used as a measure of robustness. Sensitivity of FFLs to parameters was examined in detail previously [105, 106, 109], including how FFL can carry the function of adaptation [105, 106]. However, the behavior of sensitivity of FFLs in the stochastic regime, where slow parameters binding results in highly stochastic behavior of the system is unknown.

We study the sensitivity of the regulation intensities of feed-forward loop to model parameters. Regulation intensities play important role as they define the strength of regulation in FFLs. We introduce a new definition of sensitivity, which characterizes the response of the steady state probability distribution to perturbation to system parameters, within a given interval. Further we show how the steady state responds to change of values of the parameters. We show how change in gene expression under FFL regulations are sensitive to system parameters, including the state of multistability in FFLs. Summarized results we obtained can be used for analyzing phenotypic switching in real biological network, which consist of feed-forward loop as substantial element of their architectures or for construction of synthetic networks aimed to produce certain phenotypic behavior.

3.2   Multistability in FFL

3.2.1   Architecture

We construct the network motif of FFL as a three node motif consisting of three genes a, b, and c and their protein products A, B, and C respectively (Figure 3 (A)). Gene a expresses protein A at constant expression rate s_A. Gene b has one promoter site, and turns into a gene-protein complex bA, after protein A binds to it. Gene b is expressed with a constant basal expression rate s_B, but once it is bound with a protein A the rate is changed k_1-fold. Gene c has one promoter site, which can be occupied by either one of its transcription factors A or B. This type of regulation is known as "OR" gate. Competitive binding of proteins A and B to gene c promoter site turns it to two gene-protein complexes cA or cB correspondingly. The basal expression rate of gene c is s_C, but it is changed k_2-fold for a complex cB, and by k_3-fold for a complex cA. Below we present the general system of biochemical reactions corresponding to constructed feed-forward loop model:

$$b + A \xrightarrow{r_b^A} bA; \quad bA \xrightarrow{f_b^A} b + A;$$

$$c + A \xrightarrow{r_c^A} cA; \quad cA \xrightarrow{f_c^A} c + A;$$

$$c + B \xrightarrow{r_c^B} cB; \quad cB \xrightarrow{f_c^B} c + B;$$

$$\emptyset \xrightarrow{s_A} A; \quad A \xrightarrow{d_A} \emptyset;$$

$$b \xrightarrow{s_B} B; \quad bA \xrightarrow{s_B * k_1} B; \quad B \xrightarrow{d_B = 1} \emptyset;$$

$$c \overset{s_C}{\rightarrow} C; \quad cB \overset{s_C * k_2}{\rightarrow} C; \quad cA \overset{s_C * k_3}{\rightarrow} C; \quad C \overset{d_C}{\rightarrow} \emptyset.$$
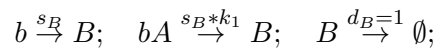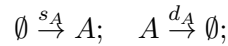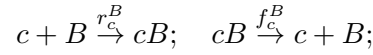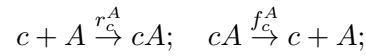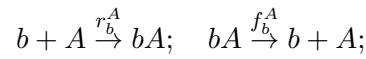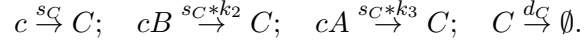
Here $r_b^A = r_c^A = r_c^B = 0.005$ are binding rated of proteins A to gene b, A to gene c, and B to gene c correspondingly, $f_b^A = f_c^A = f_c^B = 0.1$ are unbinding rates of proteins A to gene b, A to gene c, and B to gene c correspondingly; the rates of degradation of proteins A, B, and C are $d_A = d_B = d_C = 1$, and basal synthesis rates are $s_A = s_B = s_C = 10$.

Correspondingly to the sign of the regulations eight types of feed-forward loops are depicted on Figure 3 (B) [19]. Coherent FFLs are C_1, C_2, C_3, C_4 and incoherent are I_1, I_2, I_3, I_4 (Figure 3 (B)).

3.2.2 Simulations

In order to explore all possible types of phenotypic behavior of FFL we examine behavior of waste range of intensities k_1, k_2, and k_3 possible combinations. We performed the computations for a total of 5200 examples, corresponding to the different parameter k_1, k_2, and k_3 combinations. Thus $k_1 \in [0.025, 3.0]$, $k_2 \in [0.025, 5.1]$ and $k_3 \in [0.025, 5.1]$. With such parameter ranges we were able to cover all eight possible cases of feed forward loops (Figure 3 (B), Table 3.2.2).

There were six cases of multistabilities discovered for feed-forward loop (Figure 4), which are systems with one peak shown in red color, systems with two peaks, either for B, or for C, shown in yellow color, systems with three peaks for C shown in green color, systems with four peaks (two peaks for B and two peaks for C) shown in lightblue color, as well as systems with six peaks, shown in purple color. These cases fall in the categories of system with mono- or bimodality of B and up to three stable points for C.

TABLE IV. Parameter ranges for eight types of FFL modeled

Type of FFL	k_1 range	k_2 range	k_3 range
C_1	(1.0..3.0]	(1.0..5.1]	(1.0..5.1]
C_2	[0.025..1.0)	(1.0..5.1]	(0.025..1.0]
C_3	(1.0..3.0]	[0.025..1.0)	[0.025..1.0)
C_4	[0.025..1.0)	[0.025..1.0)	(1.0..5.1]
I_1	(1.0..3.0]	[0.025..1.0)	(1.0..5.1]
I_2	[0.025..1.0)	[0.025..1.0)	[0.025..1.0)
I_3	(1.0..3.0]	(1.0..5.1]	[0.025..1.0)
I_4	[0.025..1.0)	(1.0..5.1]	(1.0..5.1]

Exhaustive parameter search allows us to construct full phase space diagrams of phenotypic behavior corresponding to different parameter combinations (Figure 5). The heat map for $k_1 \leq 0.4$ or $k_1 \geqslant 2.4$ represents bimodality for B concentration, and for $2.1 > k_1 > 0.8$ the unimodality of its concentration.

The joint distributions of B and C have one peak (red colored on the (Figure 4- Figure 5)), when the values of intensities k_1, k_2, and k_3 are close to 1. It means that only one phenotypic state is observed, when the regulations intensities in FFL are weak.

There are two types of distributions with two peaks (yellow areas on the Figure 5), and yellow landscapes on the Figure 3 corresponding to two different phenotypic states. In the first case $k_1 \leq 0.4$ or $k_1 \geqslant 2.4$ the phenotypic state is characterized by bistability of B, given monostability of C. It means that if the regulation of the intensity of about two fold produces bistability for this example. For $2.1 > k_1 > 0.8$, distribution of B is bistable, and yellow areas on the diagram Figure 5 show two phenotypic states of C given monostability of B.

Green color on the heatmap Figure 5, and corresponding schematic green colored representation on the Figure 4 indicates the regions with three modes and three possible phenotypes for protein C, given monostability of B. We can observe that these regions appear, when the difference in the scale of the rates k_2 and k_3 is at least about two folds, so the stable states for every regulation intensity are separated from each other.

Blue color indicates phenotypic cases with bimodality for both B and C, and purple color corresponds to bimodality for B and three modes for C.

We can see that in the systems with the weak regulations separate phenotypic states do not appear, although when the regulations are strong systems have very well defined peaks. The heat map Figure 5 suggests two classes of FFL, based on multistability characteristics: the group of C_2, C_4, I_1, and I_3, where the tristability of output protein C always exists, given that regulation intensities are strong enough, and the group of C_1, C_3, I_2, and I_4, where the signs of the regulations of the output node C are the same, and tristability occurs only, when the regulations k_2 and k_3 have very distinct values.
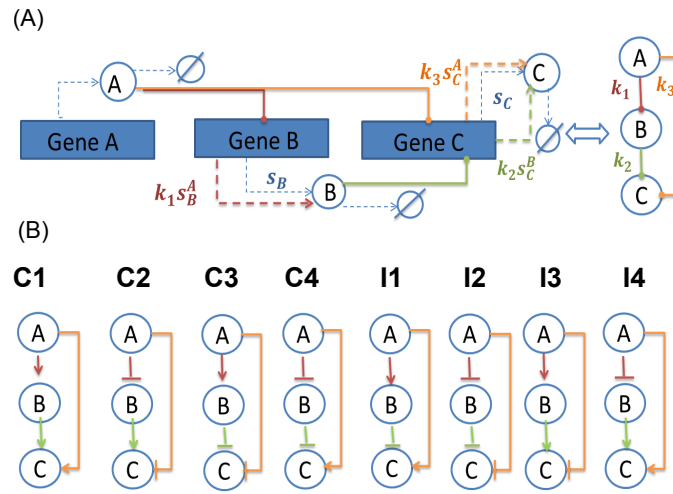
Figure 3. Topology, graphical representation, and the types of FFL: (A) General topology and corresponding 3-node schematic representation of implemented FFL containing three genes a, b, c expressing three proteins A, B, C, such that protein A regulates b and c expression by binding to them, and protein B regulates c expression. (B) The eight types of feed-forward loop.
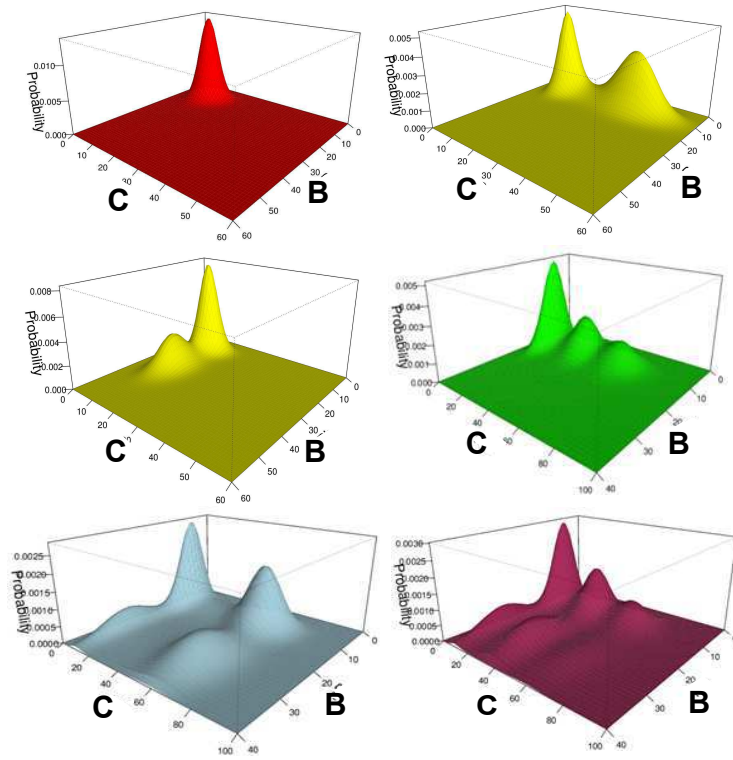
Figure 4. Different cases of multistability for Feed Forward Loop (FFL): Examples of probability landscapes for 6 cases of multistable behavior: 1 peak shown in red color; 2 peaks, either for B, or for C, shown in yellow color; 3 peaks for C shown in green color; 4 peaks (2 peaks for B and 2 peaks for C) shown in lightblue color; and 6 peaks (2 peaks for B, and 3 peaks for C) shown in purple color.
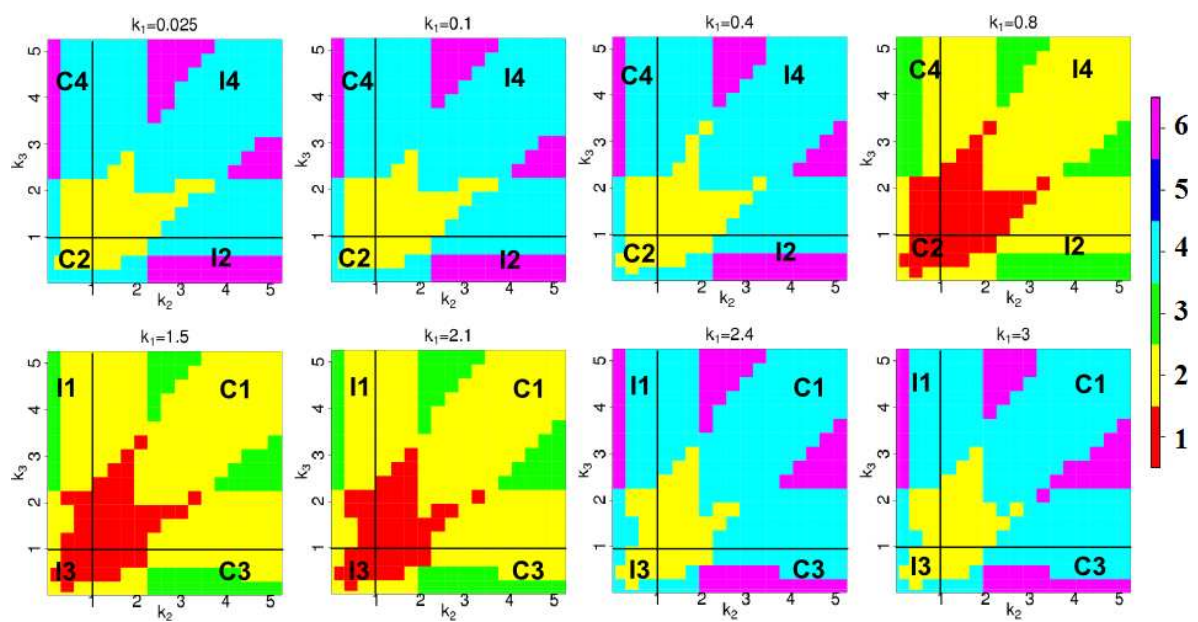
Figure 5. Full phase diagrams: different multistabilities under different reaction rates for all 8 cases of FFL.

3.2.3   Deterministic Approach

Straight mass-action kinetic law ordinary differential equation (ODE) formulation allows only to find approximate mean concentration for the species A, B, and C, and does not give any answer about the number of phenotypic states of the system. Steady state solutions with respect to discrete genes concentration for mass action kinetics tell that there are at most six phenotypic states.

The equations governing the kinetics in the constructed feed-forward loop were developed as follows:

$$\frac{d[b]}{dt} = f_b^A[bA] - r_b^A[A][b];$$

$$\frac{d[bA]}{dt} = r_b^A[A][b] - f_b^A[bA];$$

$$\frac{d[c]}{dt} = f_c^A[cA] + r_c^B[cB] - r_c^A[A][c] - r_c^B[B][c];$$

$$\frac{d[cA]}{dt} = r_c^A[A][c] - f_c^A[cA];$$

$$\frac{d[cA]}{dt} = f_c^A[B][c] - r_c^A[cB];$$

$$\frac{d[A]}{dt} = s_A - d_A[A];$$

$$\frac{d[B]}{dt} = s_B[b] + k_1 * s_B[bA] - d_B[B];$$

$$\frac{d[C]}{dt} = s_C[c] + k_2 * s_C[cA] + k_3 * s_C[cB] - d_C[C].$$

Here $[A]$, $[B]$, $[C]$ are the concentrations of proteins A, B, and C respectfully. $[b]$, $[c]$ are the concentrations of genes b, and c, and $[bA]$, $[cA]$, $[cB]$ are the concentrations of genes b, and c in corresponding bound states bA, cA, cB.

Let the total amount of molecules of gene b in the system be n_b, and total amount of molecules of gene c in the system be correspondingly n_c. Hypothetically assume that the copy numbers of genes b and a are high, then the unique deterministic solution of the system above looks as follows:

$$[b] = \frac{f_b^A n_b}{f_b^A + r_b^A [A]};$$

$$[bA] = \frac{n_b r_b^A [A]}{f_b^A + r_b^A [A]};$$

$$[c] = \frac{f_c^A f_c^B n_C}{f_c^A f_c^B + f_c^B r_c^A [A] + f_c^A r_c^B [B]};$$

$$[cB] = \frac{f_c^A r_c^B n_C [B]}{f_c^A f_c^B + f_c^B r_c^A [A] + f_c^A r_c^B [B]};$$

$$[cA] = \frac{f_c^B r_c^A n_C [A]}{f_c^A u_c^B + f_c^B r_c^A [A] + f_c^A r_c^B [B]}$$

$$[A] = s_A / d_A;$$

$$[B] = \frac{s_b n_b}{d_b} \cdot \frac{f_b^A + k_1 r_b^A [A]}{f_b^A + r_b^A [A]}$$

$$[C] = \frac{s_C n_C}{d_C} \cdot \frac{f_c^A f_c^B + k_2 f_c^B r_c^A [A] + k_3 f_c^A r_c^B [B]}{f_c^A f_c^B + f_c^B r_c^A [A] + f_c^A r_c^B [B]}$$

However the copy number of genes in the real systems is low, and usually does not exceed two copies. Thus the formulation of mass-action kinetics equation for $[b]$ and $[c]$ in a canonical way is not reasonable. Indeed in the case of $n_b = n_c = 1$, quantities $[b]$, $[bA]$, $[c]$, $[cA]$, and $[cB]$ are fractions from the interval $[0,1]$, whereas they can only be equal to 0 and 1. In this case we can compute six integer steady state solutions with respect to $[b]$, $[bA]$, $[c]$, $[cA]$, and $[cB]$ concentrations. Every each of these solutions corresponds to particular combination of gene copy numbers. They are 8-tuples $([A], [B], [C], [b], [bA], [c], [cA])$, such as

$$(s_A/d_A, s_B/d_B, s_C/d_C, 1, 0, 1, 0, 0),$$

$$(s_A/d_A, k_1 s_B/d_B, s_C/d_C, 0, 1, 1, 0, 0),$$

$$(s_A/d_A, s_B/d_B, k_2 s_C/d_C, 1, 0, 0, 1, 0),$$

$$(s_A/d_A, k_1 s_B/d_B, k_2 s_C/d_C, 0, 1, 0, 1, 0),$$

$$(s_A/d_A, s_B/d_B, k_3 s_C/d_C, 1, 0, 0, 0, 1),$$

$$(s_A/d_A, k_1 s_B/d_B, k_3 s_C/d_C, 0, 1, 0, 0, 1).$$

From this deterministic assumption given discrete set of genes we obtain six stable peaks for the system. However as we show in the work when the rates of regulation are not very well separated in space some of these peaks can be merged together. Note that this approach is different from

boolean modeling, where the analysis is conducted in a qualitative way (as ON/OFF output) at time dynamics [110].

In the real biological systems these states could be not well separated in space and some of the peaks could merge together. For example on the Figure 6 we can see two examples of discrepancy in between analytical predictions from deterministic model and accurate values from direct solution of dCME for averages and modes of steady state protein C probability distribution. On the Figure 6 (A) the mean value from ODE (vertical blue line) and the first moment of exactly computed probability landscape (vertical yellow line) diverge from each other. Three green lines represent possible distinct phenotypic states, and diverge from real solutions. On the Figure 6 (B) we observe three predicted from ODE phenotypes, however in the reality system has only one peak. The mean obtained from ODE and real mean computed from the distribution overlap, but in this case mean value does not carry any significant information about system behavior and phenotypical variability. We can see that deterministic modeling are not effective in studies of system phenotype.

3.2.4 The Dependence of the Multistability and Values of k_2 and k_3

The number of modalities of protein B in FFL architecture completely depends on regulation intensity of k_1 with respect to its basal expression rate, as the intensities k_2 and k_3 due to network architecture do not affect the phenotype of B. The question we want to raise in this section, is how the regulation intensities k_1, k_2, and k_3 affect the number of peaks of protein C.

We start from $k_1 = 0.025$ (Figure 7 (A)) and change it gradually, until we reach $k_1 = 3.0$ fixing the number of changes of phenotypic states. The red color on the map (Figure 7 (D))
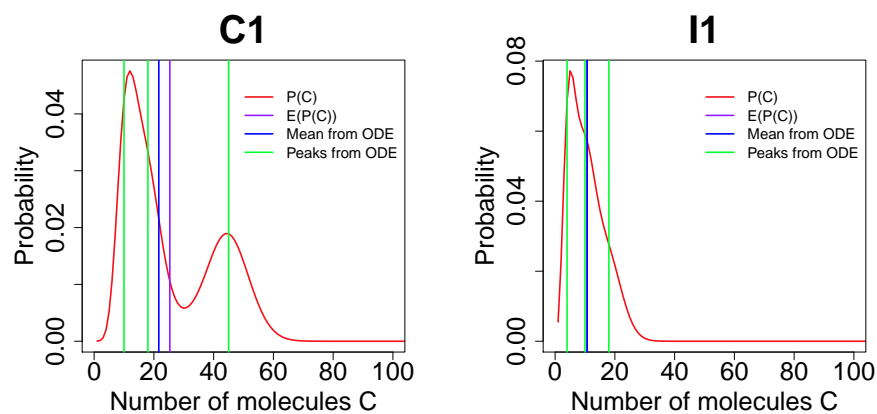
Figure 6.   Examples of discrepancy in between deterministic and stochastic modeling of Feed

Forward Loop (FFL) for two examples: (A) There are three modalities predicted from

deterministic approach with discrete set of genes, however the solution of corresponding

dCME gives only two peaks; the yellow line, which stands for exact mean diverges from the

red line, which stands for the predicted mean from ODE; (B) There are three peaks predicted

from deterministic approach with discrete set of genes, however there is only one possible

phenotype in reality.

indicates "zero change" areas meaning that in the systems with such values k_2 and k_3, the change of k_1 will not affect the number of phenotypes. As opposed to the red areas orange color indicating 1-2 changes of the number of phenotypic states while changing k_1 gradually is less abundant. However the places of the localization of this color are approximately on the joints of heatmap Figure 7 (A). It means that when phenotypic state for some parameter combination is not stable, the mutation of the regulation rate k_1 can affect the change of phenotype of output, while for the systems with well distinguished phenotypes the change of k_1 do not disturb the phenotype of the output C.

The affect of k_2 and k_3 on phenotypic behavior of output is more explicit and direct. The Figure 7 (B) shows the colormap for the number of possible phenotypic states for possible combinations of k_1 and k_3 given $k_2 = 0.025$, and correspondingly (E) shows the number of times this phenotypic behavior changes with the gradual change of k_2 on the interval (0.025, 5.1). We can see the abundance of yellow color indicating high sensitivity of phenotypes to k_2 change. As in the previous case the yellow area (4 changes of the phenotypic states), is close to the joints in between areas with different number of modes. There are particular cases, when small increase of rate k_3 gives big phenotypic changes to the output behavior. For example, for k_1 fixed at 1.5 for $k_3 = 3.6$ we have four changes of phenotype, when for $k_3 = 3.9$ only one change. Indeed on the Figure 7 (D) for $k_3 = 3.9$, we can see that the system changes only once from three possible peaks to one possible peak. These are the regions of high robustness of the phenotype.

Analogously we plot the color diagram of the number of peaks given different parameter combinations of k_1 and k_2 given k_3 fixed at 0.025 (Figure 7 (C)), and corresponding color map of the number of change of the modes of C for k_3 changing on the interval $(0.025, 5.0)$. Note that the behavior is very similar to the previous case, meaning that phenotypic multistability strongly depends on both of the values of k_2 and k_3.

3.2.5   Gene Duplication and Multistability

Understanding how gene duplication affects phenotypic variability is important, when for instance studying appearance of disease [111], or origin of evolution [112].

In order to show how insertion of a gene can the affect the number of possible phenotypes, we modeled a case, when there are two copies of gene c. There are six possible states of the system depending on whether the promoter sites of gene c is free or occupied. Thus for a triplet (c, cA, cB) possible states are $(2,0,0)$, $(0,2,0)$, $(0,0,2)$, $(1,1,0)$, $(1,0,1)$, $(0,1,1)$. These generic states can result in separate phenotypic states given slow promoter dynamics of the system. In the case when rates of expression and basal rates are not very well separated in space, the phenotypic states are being merged. On the Figure 8, we plot the distributions of the number of possible phenotypes for protein C given one copy of c (C), and two copies of c (B) for $k_1 = 0.025$. We can observe that the red area corresponding to monostable region is larger in case of two copies of gene c. This result shows that introducing multiple copies of gene can not only enrich phenotypic behavior, but also cause merging of different phenotypic states together, basically leading to a single phenotype with the increase of the number of gene c.

Note that bacterial cell can have multiple copies of the same gene, taking into account fast binding and unbinding dynamics, we do not belive that stochastic multimodality phenomena is typical for this organism. However in mammalian cells there are only two copies of the same gene, and given slow promoter dynamics, stochastic phenotypic switching seems to appear as a natural mechanism for them. Although we were not able to catch all six phenotypic states for C at our parameter space (Figure 7 (B)), we were able to observe the cases with four and five modes of the output (blue and purple areas correspondingly).

Assuming that in the beginning of the cell life both of the two copies of the gene are functioning, and later due to mutations one of the copies gets knocked out, we can expect two opposite types of scenarios to happen: one of the phenotypic states is lost, if regulation intensities are large, as well as a new possible diseased phenotype is getting developed, when regulation intensities are low. Further increase of the copies of c in the system will lead to increase of the region of monostability, giving larger number of possible modes. Basically insertion of the gene can lead to larger number of the states, but at the same time only feed-forward loops with strong regulations intensities develop these new phenotypic states. System with low intensities are loosing the states and become more stable.

We can see that insertion and deletion are symmetrical processes in principle with regards to transcription factor regulations activities, and we believe that it explains the relation of insertion to adaptation [113], as areas where the system are monostable are larger, so basically slight change of regulation intensities will not bring a system to a system with more phenotypic states.

3.2.6   Input Intensity and Multistability

In one of the experiments we conducted we changed synthesis intensity of protein A to see how it affects the number of modes of the proteins B and C. On the Figure 9 (A) we plot the heatmap for the number of modes of C1 given $s_A = 3.0$ and on the Figure 9 (B) correspondingly for $s_A = 10.0$. We can see that for higher values of k_1 the second peak for protein B appears faster. Thus at $k_1 = 2.4$ we have two peaks for protein B for $s_A = 10$, and only one peak for $s_A = 3.0$. We also can observe that the areas of monostability for weaker input are wider, and the areas with the higher number of peaks are less. From that we can conclude that high input induces multiphenotypic behavior.

3.2.7   Speed of Promoter Binding and Multistability

All the previous results were obtained for slow binding and unbinding reactions rates systems. Indeed when the system switches in between phenotypic states slowly, the synthesis-degradation process for C can converge to its equilibrium at every phenotypic state of gene c. The questions we want to answer with this section is how slow should be promoter dynamics in order to be able to obtain multiple phenotype due to stochastic fluctuations with no feed-back and cooperativity. Thus we were gradually changed binding and unbinding affinities of gene c for I1 with regulation intensities fixed at $k_1 = 3.0$, $k_2 = 0.025$, $k_3 = 5.1$ in order to see how the number of phenotypic states was affected by $GeneC$ binding dynamics. For slow binding kinetics the output C of FFL discussed above has three peaks which, are $C = 0$ corresponding to protein C expression when $GeneC$ is inhibited by B, $C = 9$ corresponding to basal C expression, and $C = 49$ corresponding to C expression activated by A.
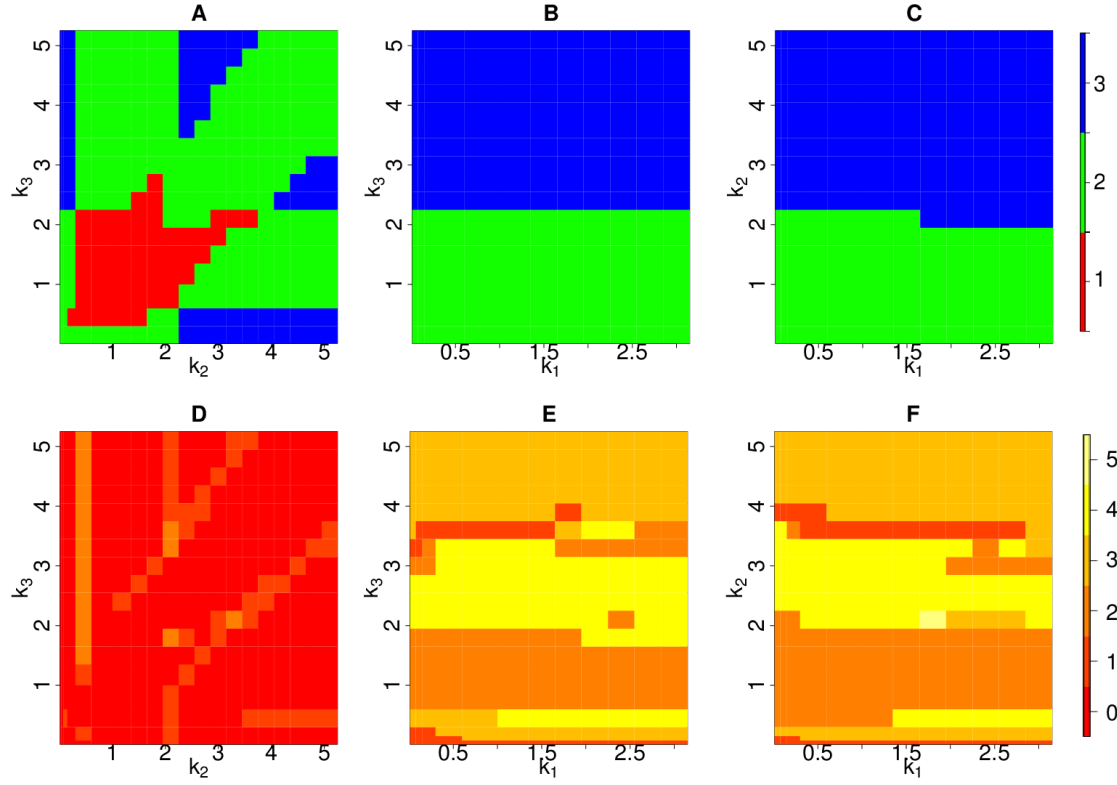
Figure 7. The heatmaps for the number peaks of the output protein C for (A) k_1 fixed at 0.025, (B) k_2 fixed at 0.025, (C) k_3 fixed at 0.025, and corresponding color diagrams for number of changes of peaks of C when (D) k_1 changes on the interval (0.025,3.0), (E) k_2 changes on the interval (0.025,5.0), (f) k_3 changes on the interval (0.025,5.0).
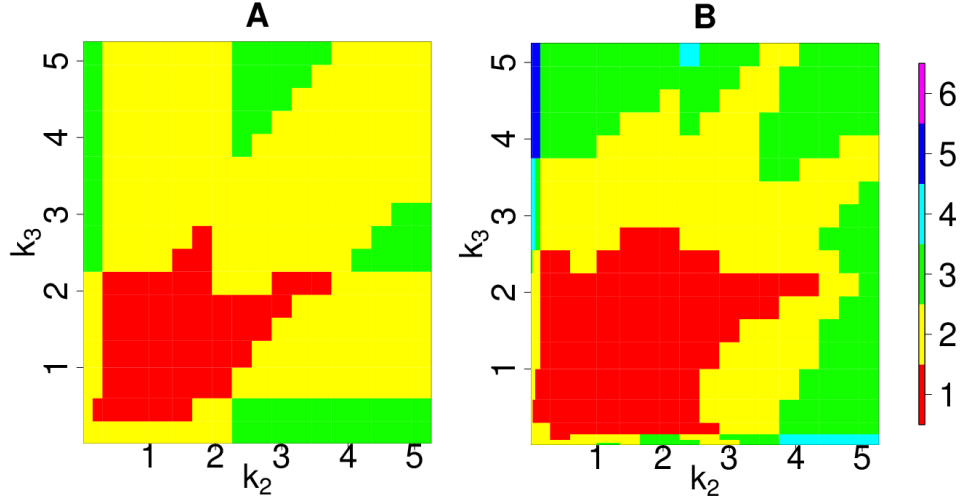
Figure 8. Number of phenotypes corresponding to protein C concentration for FFL with $k_1 = 0.025$ for the cases of (A) one gene in the system and (B) two genes in the system.

On the Figure 10 (A) the output of protein C is plotted, when both binding affinity in between c and A and c and B have the same values, and we are gradually changing them to n-fold, $n = 0.5, 2, 4, 8, 16$ from our generic case. We can see that for slower than our generic case dynamics (red line, $n = 0.5$) the modes of the distribution are even better distinguished. However with increase of both binding and unbinding rates both peaks for synthesis and degradation dissapear at $n = 8$ fold (green line), and at $n = 16$ we see the monostable distribution with one peak. On the Figure 10 (B) the output of protein C is plotted, when only binding affinity in between c and B was changed to n-fold, $n = 0.5, 2, 4, 8, 16$, and the biding rate in between c and A remains the same as for generic example. The peak corresponding to expression
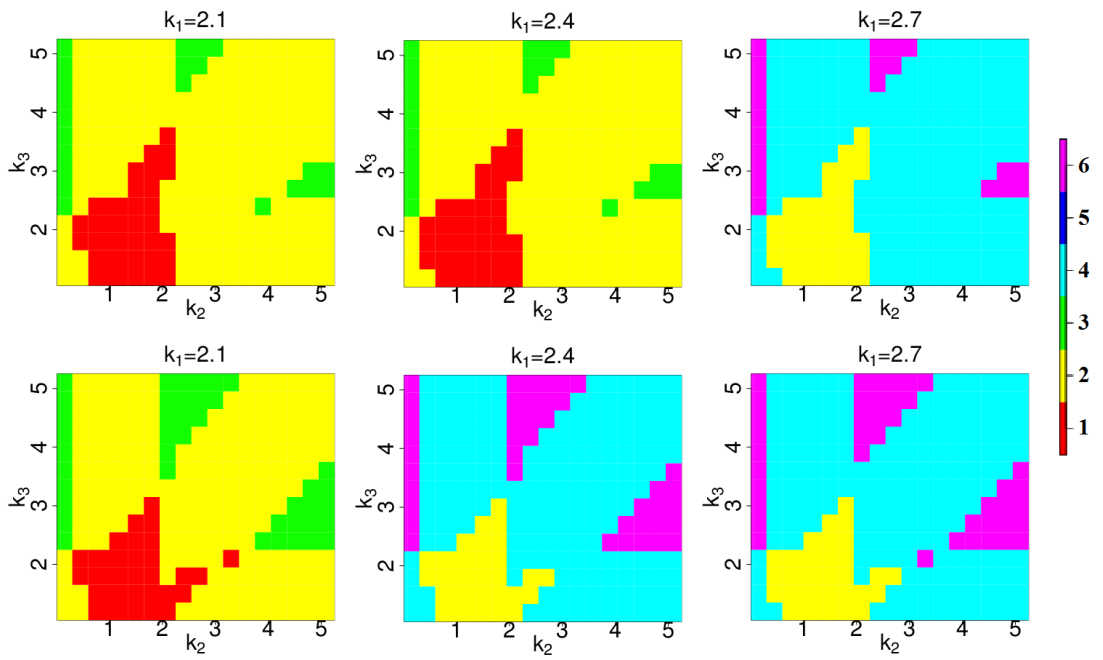
Figure 9. Number of peaks of the system for C1 with (A) $s_A = 3.0$ (B) $s_A = 10.0$.

of c, when activated by A remains robust, however the peak for c at inhibited state is getting smaller with binding rate increase until it merges with peak for basal expression at $n = 16$ (darkgreen line). Figure 10 (C) depicts the probability distributions of C, when only binding affinity of protein A to gene c is changed to n-fold, $n = 0.5, 2, 4, 8, 16$. The peak corresponding to expression of c, when it is inhibited by B does not change, however the peak for gene c at the activated state dissapears with binding rate increases as in the previous case. The basal expression rate and unbinding rate are the number of the same magnitude for $n = 16$, meaning that multiple phenotypes in feed-forward regulations are possible when unbinding rate is at least about a magnitude smaller than the expression rate of the protein.

The speed of the binding dynamics of b correlates in a similar way with phenotypic behavior of protein B, however generally does not affect the output C.

These results were confirmed by experimental study [114], where the fast switchers were usually showing environmental conditions with mixed phenotype, but slow switchers were showing distinct environmental conditions for every phenotype of positive feedback loop.

3.3   Sensitivities of Regulation Intensities in FFL

3.3.1   Definition of Sensitivity

In deterministic models, sensitivity of parameters simply measures changes in the output at steady state, when values of model parameters are altered. In stochastic models where the output is a probability distribution, sensitivities is often measured by changes in the expected value of the output [115].
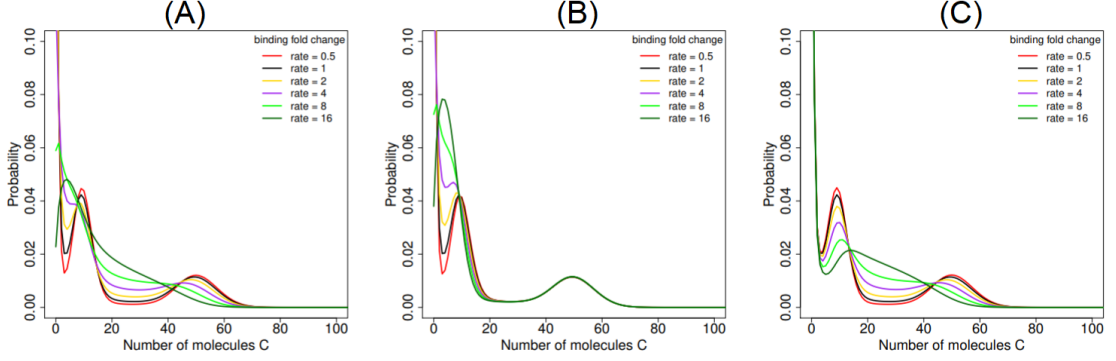
Figure 10. The distributions for I1 with $k_1 = 3.0$, $k_2 = 0.025$, $k_3 = 5.1$, when (A) c binding affinity to both protein B and A was changed $n - fold$, (B) c binding affinity to both protein B was changed $n - fold$, (B) c binding affinity to both protein A was changed $n - fold$.

Here we introduce a new definition of stochastic sensitivity and show it is more effective in measuring the differences and similarities in behavior of different types of FFLs.

We define the sensitivity $s'_{k_i}(k_0, k)$ to changes in k_i, $i = 1, 2, 3$, whose value is altered from k_0 to k as follows:

$$s'_{k_i}(k_0, k) = \mathbb{E}\left[\frac{|P_k(\mathbf{x}) - P_0(\mathbf{x})|}{P_0(\mathbf{x})} \Big/ \frac{|k - k_0|}{k_0}\right],$$

where $P_0(\mathbf{x})$ is the system probability landscape at parameter value of $k_i = k_0$ and $P_k(\mathbf{x})$ is the landscape at $k_i = k \neq k_0$. The value of parameter k_i belongs to a finite interval (a, b), which

is $(0, 1)$ for inhibition and $(1, A)$ for activation, where A is some finite number. The sensitivity of s_{k_i} on the interval (a, b) is defined as:

$$s_{k_i} = \max_{k_0, \, k \in (a, \, b)} s'_{k_i}(k_0, k). \tag{3.1}$$

Our stochastic sensitivity is specific to the intervals of regulation intensities, which is FFL specific.

3.3.2 Sensitivity of Regulation Intensity k_1

We examined the stochastic sensitivity of regulation intensity k_1 using (Equation 3.1). We consider the cases when gene b is inhibited by protein A, with $k_1 < 1$, and gene b is activated by protein A, with $k_1 > 1$ (Figure 11).

The sensitivity of k_1 is smaller in the green and yellow regions of Figure 11, and larger in the white and pink regions (Figure 11). There are two situations when the sensitivity of k_1 is smallest, and the system is most robust to change in k_1. The first situation is when $k_2 = 1$, where the regulation of the gene c by B is weak, such that the expression of c does not depend on B copy number. The other region is where $k_2 = k_3$, both the rates of activation/inhibition of c by B and c by A are of similar values. It means that the system is robust to k_1 change when the proteins A and B regulate the output node C with the same intensity. The sensitivity of k_1 is also small for the smallest values of k_1 (i.e., $k_1 < 1$), and larger for larger values of k_1 (i.e., $k_1 > 1$).
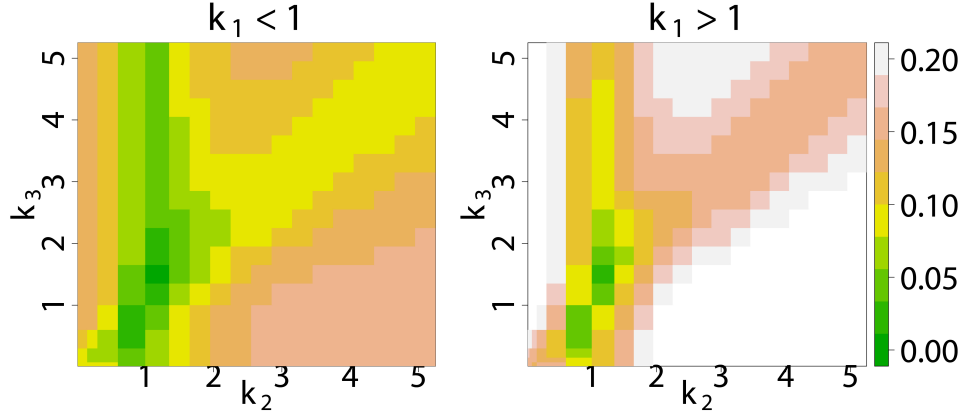
Figure 11. The sensitivity of regulation intensity $s(k_1)$ on the inhibition of gene b by protein A ($k_1 < 1$), and on the activation of gene b by protein A ($k_1 > 1$).

3.3.3   Sensitivity of Regulation Intensity k_2

We examined the stochastic sensitivity of regulation intensity k_2 using (Equation 3.1). We consider the cases when gene c is inhibited by protein B, with $k_2 < 1$, and gene c is activated by protein B, with $k_2 > 1$ (Figure 12).

The sensitivity of k_2 is smaller in the green and yellow regions of Figure 12, and larger in the white and pink regions (Figure 12). The sensitivity is smaller, when the values of k_1 are small, specifically, A inhibits the expression of b and the overall copy number of B in the system is reduced. Hence, the regulation of output C by B is less prominent, and k_2 has smaller sensitivity. The sensitivity of k_2 is also smaller for the small values of k_2 (i.e., $k_2 < 1$), and
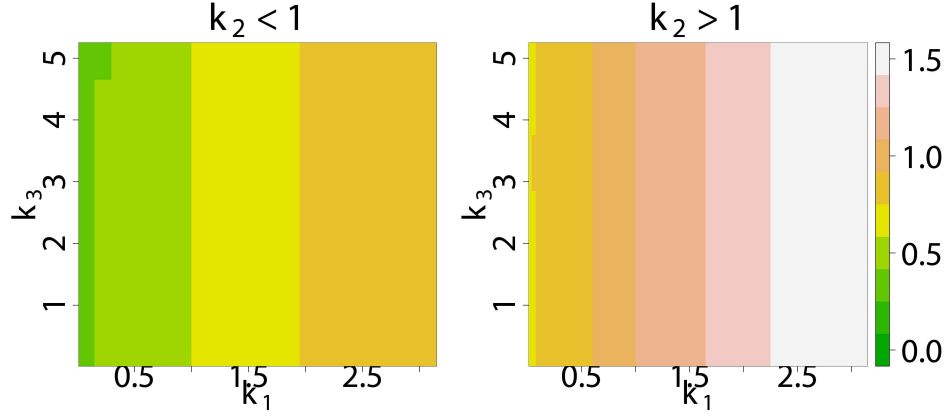
Figure 12. The sensitivity of regulation intensity $s(k_2)$ on the inhibition of gene c by protein B ($k_2 < 1$), and on the activation of gene c by protein B ($k_2 > 1$).

larger for larger values of k_2 ($k_2 > 1$). The dependence of the sensitivity of k_2 to the value of k_3 is negligible.

3.3.4 Sensitivity of Regulation Intensity k_3

We examined the stochastic sensitivity of regulation intensity k_3 using (Equation 3.1). We consider the cases when gene c is inhibited by protein A, with $k_3 < 1$, and gene c is activated by protein A, with $k_3 > 1$ (Figure 13).

The sensitivity of k_3 is smaller in the green and yellow regions of the Figure 13, and larger in the white and pink regions (Figure 13). Smaller k_3 sensitivities correspond to larger values of k_1. In this situation A activates the expression of c, therefore the effect of the regulation of c by direct path is more prominent. There is also a weak dependence of the sensitivity of k_3 of
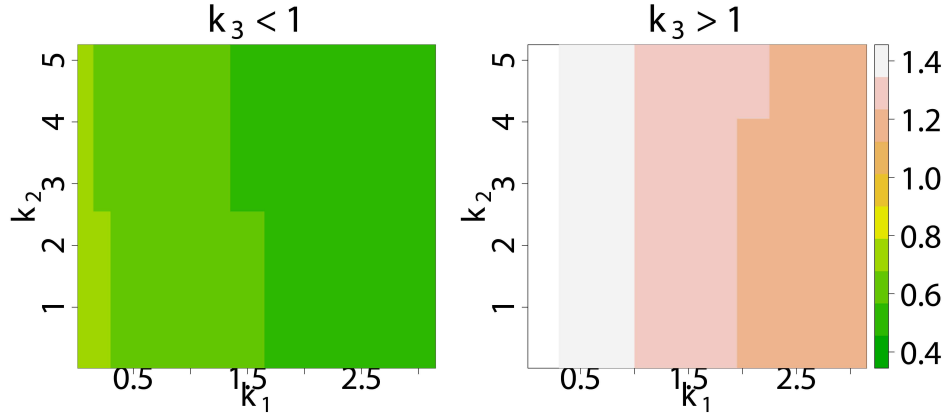
Figure 13. The sensitivity of regulation intensity $s(k_3)$ on the inhibition of gene c by protein A ($k_3 < 1$), and activation of gene c by protein A ($k_3 > 1$).

the value of k_2. Smaller k_3 sensitivities correspond to larger values of k_2 in the case of $k_3 < 1$, where the inhibition is more prominent with larger k_2. Smaller k_3 sensitivities correspond to smaller values of k_2 in the case of $k_3 > 1$, where the activation is more prominent with larger k_2. The sensitivity of k_3 is also smaller for the small values of k_3 ($k_3 < 1$), and larger for larger values of k_3 ($k_3 > 1$).

3.3.5 Dependence of Sensitivity on Multistability of FFLs

We now examine the dependence of the values of the sensitivity on the number of peaks in the system Table. (3.3.5). Our results show that the number of peaks is correlated with the sensitivities of k_1, k_2, and k_3. FFLs with three peaks are the least robust to changes in the

TABLE V. k_1, k_2, and k_3 sensitivities of coherent and incoherent FFLs with different numbers of peaks

Type of FFL	Number of peaks	Mean k_1	Mean k_2	Mean k_3
Coherent	3	0.16	0.80	0.94
	2	0.15	0.77	0.69
	1	0.12	0.44	0.47
Incoherent	3	0.20	1.02	0.89
	2	0.15	0.72	0.75
	1	0.11	0.57	0.46

parameters for both coherent and incoherent FFLs. In contrast, systems with one peak are the most robust to the change of the parameters for both case of coherent and incoherent loops.

3.4 Conclusions

Gene regulatory networks play crucial role in defining cellular phenotype characteristics and molecular content. Their modeling is a hot topic of system biology field, which remains to be challenging due to high complexity and ubiquitously stochastic nature of them. Although gene regulatory networks in the cell in general might consist of dozens of genes and their proteins products, their functions are usually defined by smaller subnetwork subunits called network motifs. One of the interesting questions of network motifs properties is their role

in maintaining multiphenotypic behavior. Deterministic models restrict the class of networks capable to generate multiple phenotypes only to feed-back network motifs. In oppose to that, stochastic models show that multiple phenotypes of the system can be generated from stochastic fluctuations in between states with distinct gene expression levels. This phenomena is associated with mammalian cells, which have highly stochastic behavior and slow promoter dynamics due to complexity of their chromatin structure.

In this work we studied feed-forward loop network motifs as one of the most ubiquitous three node network motifs, which has high significance in mammalian cells. Its deterministic dynamic behavior is well studied, and suggests signal processing and adaptation functions. However modeling of feed-forward loop network model with taking into account stochasticity remains to be a challenging and promising research topic. The results of our computational experiments showed that feed-forward loop can generate multiple cell phenotypes due to stochastic fluctuations in between distinct expression levels given slow promoter dynamics. The regulation intensities are the key players, which could be tuned in order to obtain certain phenotypic behavior. The direct regulation path from the input to output and indirect path through the intermediate buffer node could result in two separate modalities, which together with basal expression of the output gene, generate three distinct phenotypes of the system for the system with one copy of output gene c. By combining this result and two possible phenotypes for gene b we obtained six modalities for feed-forward loop. When the number of copies of gene c is two the number of phenotypic states for the output protein C can be at most six, giving 12 phenotypes points in total. However in reality this case is hard to achieve due to necessity of

high separation of rates. In contrast with this we showed that the increase of the number of peaks in general leads to expansion of the area of monostability, as the regions of the expression with different rates get merged together. Another interesting observation made is that high intensity of input amplifies multistability in feed-forward loop, suggesting feed-forward loop architecture to be favorable for maintaining multiple phenotypic states.

Hight significance of feed-forward loop in stem cell regulation network containing core pluripotency transcription factors $Oct4$ and $Nanog$ suggests its active role in maintaining pluripotency versus differentiation [21]. In this type of networks $Nanog$ participates as intermediate node, which get activated by $Oct4$, and then both of these factors control the expression of genes associated with the onset of differentiation or pluripotency.

We also studied the sensitivities of regulation intensities of feed-forward loops (FFLs) under the conditions of slow promoter binding. We first computed the precise steady state probability distributions of eight types of FFLs under a wide range of conditions. Obtained results reveal the overall of multistable behavior of FFLs in the copy number of C. We introduced a new definition of the stochastic sensitivity, to quantify the sensitivity of different parameters of stochastic FFL. I showed how the steady state distribution responds to changes in model parameters. Specifically, we quantified how sensitivities of regulation intensities depend on the values of other regulation intensities and the state of multistability of the system. We found that the sensitivity of regulation intensity k_1 depends on the values of k_2 and k_3, whereas the sensitivities of k_2 and k_3 strongly depend on k_1. The FFL with more peaks of protein C copy number is less robust.

The results of this work could be used in construction of synthetic feed-forward loop, and choosing parameters of the system according to particular programmed phenotypic behavior.

CHAPTER 4

DISCRETE FLUX AND VELOCITY FIELDS OF PROBABILITY AND THEIR GLOBAL MAPS IN REACTION SYSTEMS

4.1   Introduction

Reprinted from "Terebus A, Liu C, Liang J. Discrete flux and velocity fields of probability and their global maps in reaction systems. The Journal of chemical physics. 2018 Nov 14;149(18):185101" with the permission of AIP Publishing

Biochemical reactions in cells are intrinsically stochastic [16,60,61,64]. When the concentrations of participating molecules are small or the differences in reaction rates are large, stochastic effects become prominent [62–65]. Many stochastic models have been developed to gain understanding of these reaction systems [7,67,69,116,117]. These models either generate time-evolving landscapes of probabilities over different microstates [67, 69, 116, 117], or generate trajectories along which the systems travel [7, 10]. Vector fields of probability flux and probability velocity are also of significant interest, as they can further characterize time-varying properties of the reaction systems, including that of the non-equilibrium steady states [33–37,118]. For example, determining the probability flux can help to infer the mechanism of dynamic switching among different attractors [31, 32]. Quantifying the probability flux can also help to characterize the departure of non-equilibrium reaction systems from detailed balance [35,40,41], and can help to identify barriers and checkpoints between different stable cellular states [39]. Computing proba-

68

bility fluxes and velocity fields has found applications in studies of stem cell differentiation [42], cell cycle [39], and cancer development [43, 44].

Models of probability fluxes and velocities in well-mixed mesoscopic chemical reaction systems have been the focus of many studies [31, 36, 37, 39–41, 46, 74, 119–121]. They are often based on the formulation of the Fokker-Planck and the Langevin equations, both involving the assumption of Gaussian noise of two moments [36,37,39,41,118,122]. However, these models are not valid when copy numbers of molecular species are small [30, 73–75], as they do not provide a full account of the stochasticity of the system [8, 30, 73–76]. For example, the Fokker-Planck model fails to capture multistability in gene regulation networks with slow switching between the ON and the OFF states [30]. These models are also of inadequate accuracy when systems are far from equilibrium [75]. Moreover, solving the systems of partial differential equations resulting from the Fokker-Planck and Langevin Equations requires explicit boundary conditions for states where one or more molecular species have zero copies [37]. These boundary conditions are ill-defined in the context of Gaussian noise [123] and are difficult to impose using the Fokker-Planck/Langevin formulation, or any other continuous models, as reactions cannot occur on boundary states when one or more reactants are exhausted.

Several discrete models of probability flux and velocity based on continuous-time Markov jump processes associated with the firing of reactions have also been introduced [31, 119–121]. However, these models have limitations. The models developed in [31, 121] account only for outflow fluxes. While the probability of transition to a subsequent microstate after a reaction jump is accounted for, the inflow flux describing the probability of transition into the current

microstate from a previous state is not explicitly considered. The work in [124] studies the phosporylation and dephosophorylation process. It introduces a formulation of discrete flux based on a forward finite difference operator. However, this is only applicable to this special system of simple single-species reactions, where there is no mass exchange between the two different molecular types. The models developed in [119, 120] are limited to analysis of single reactional trajectories. In addition, the probability flux is often assumed to be associated with reactions that are reversible [125]. While these models offer an in-the-moment view on how probability mass moves in the system by following trajectories generated from reaction events, they do not offer a global picture of the time-evolving probability flux at a specific time or at fixed locations in the state space. To construct the global flow-map of discrete probability flux and velocity, proper formulations of discrete flux and velocity, as well as methods to quantify the discrete forward and backward flux between every two states connected by reactions are required.

In this work, we introduce the appropriate formulations of discrete flux and discrete velocity for arbitrary mesoscopic reaction systems. We redefine the derivative operator and discrete divergence based on the discrete nature of chemical reactions. The discreteness of both the state space and the jump processes of reactions is taken into consideration, with the discrete version of the continuity equation satisfied. Our approach allows the quantification of probability flux and velocity at every microstate, as well as the ability in tracing out the outflow probability fluxes and the inflow fluxes as reactions proceeds. In addition, proper boundary conditions are imposed so vector fields of flux and velocity can be exactly computed anywhere in the

discrete state space, without the difficulty of enforcing artificial reflecting conditions at the boundaries [126]. Our method can be used to exactly quantify transfer of probability mass and to construct the global flow-map of the probability flux in all allowed directions of reactions over the entire state space. Results computed using our model can provide useful characterization of the dynamic behavior of the reaction system, including the high probability paths along which the probability mass of the system evolves, as well as properties of their non-equilibrium steady states.

The accurate construction of the discrete probability flux, velocity, and their global flow-maps requires the accurate calculation of the time-evolving probability landscape of the reaction networks. Here we employ the recently developed ACME method [69, 84] to compute the exact time-evolving probability landscapes of networks by solving the underlying discrete Chemical Master Equation (dCME). This eliminates potential problems arising from inadequate sampling, where rare events of low probability are difficult to quantify using techniques such as the stochastic simulations algorithm (SSA) [7, 9, 10].

In this chapter we first introduce the concept of ordering of the microstates of the system, the definitions of discrete derivatives and divergence, as well as flux and velocity on a discrete state space. We further illustrate how time-evolving probability flux and velocity fields can be computed for three classical systems, namely, the birth-death process [69, 127], the bistable Schlögl model [10, 128], and the oscillating Schnakenberg system [37, 90, 129].

4.2   Models and Methods

Recall, that for a well-mixed biochemical system with constant volume and temperature, and n molecular species X_i, $i = 1, \ldots, n$, which participate in m reactions R_k, $k = 1, \ldots, m$, the microstate $\mathbf{x}(t)$ of the system at time t is a column vector of copy numbers of the molecular species: $\mathbf{x}(t) \equiv (x_1(t), x_2(t), \ldots, x_n(t))^T \in \mathbb{Z}_+^n$, where all values are non-negative integers. All the microstates that the system can reach form *the state space* $\Omega = \{\mathbf{x}(t) | t \in (0, \infty)\}$. The size of the state space is denoted as $|\Omega|$. The probability of the system to be at a particular microstate $\mathbf{x}$ at time t is denoted as $p(\mathbf{x}, t) \in \mathbb{R}_{[0,1]}$. The probability surface or landscape $\mathbf{p}(t)$ over the state space Ω is denoted as $\mathbf{p}(t) = \{p(\mathbf{x}, t) | \mathbf{x} \in \Omega)\}$. A reaction R_k takes the general form of
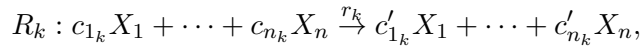
$$R_k : c_{1_k} X_1 + \cdots + c_{n_k} X_n \overset{r_k}{\to} c'_{1_k} X_1 + \cdots + c'_{n_k} X_n,$$

so that R_k brings the system from a microstate $\mathbf{x}$ to $\mathbf{x} + \mathbf{s}_k$, where the stoichiometry vector

$$\mathbf{s}_k \equiv (s_k^1, \ldots, s_k^n) \equiv (c'_{1_k} - c_{1_k}, \ \ldots, c'_{n_k} - c_{n_k})$$

gives the unit vector of *the discrete increment* of reaction R_k. $\mathbf{s}_k$ also defines *the direction of the reaction R_k*.

The discrete Chemical Master Equation (dCME) is a set of linear ordinary differential equations (Equation 1.1) describing the changes of probability over time at each miscrostate

of the system [7, 17, 18, 71]. The dCME for an arbitrary microstate $\mathbf{x} = \mathbf{x}(t)$ can be written in the general form as:

$$\frac{\partial p(\mathbf{x}, t)}{\partial t} = \sum_{k=1}^{m} [A_k(\mathbf{x} - \mathbf{s}_k)p(\mathbf{x} - \mathbf{s}_k, t)$$
$$- A_k(\mathbf{x})p(\mathbf{x}, t)], \quad \mathbf{x} - \mathbf{s}_k, \mathbf{x} \in \Omega,$$

where the reaction propensity function $A_k(\mathbf{x})$ is determined as follows $\mathbf{x}$:

$$A_k(\mathbf{x}) = r_k \prod_{l=1}^{n} \binom{x_l}{c_{lk}}.$$

It is possible that only a subset or none of the permissible reactions can occur at a particular state $\mathbf{x}$ if it is at the boundary of the state space Ω, where the number of reactants is inadequate. Specifically, we define the boundary states $\partial\Omega_k$ for reaction k as the states where reaction R_k cannot happen:

$$\partial\Omega_k \equiv \{\mathbf{x} = (x_1, \ldots, x_i, \ldots, x_n)| \quad \text{there exist} \quad i : x_i < c_{i_k}\}.$$

We define the overall boundary states as $\partial\Omega \equiv \bigcup_{k=1}^{m} \partial\Omega_k$.

Reactional probability vector and its time-derivative. We can consider each of the k-th reactions separately and decompose the right hand side of (Equation 1.1) into m components, one for each reaction, $k = 1 \ldots m$:

$$\frac{\partial p_k(\mathbf{x}, t)}{\partial t} = A_k(\mathbf{x} - \mathbf{s}_k) p(\mathbf{x} - \mathbf{s}_k, t) - A_k(\mathbf{x}) p(\mathbf{x}, t). \tag{4.1}$$

$\partial p(\mathbf{x}, t)/\partial t$ in (Equation 1.1) therefore can also be written as:

$$\frac{\partial p(\mathbf{x}, t)}{\partial t} = \sum_{k=1}^{m} \frac{\partial p_k(\mathbf{x}, t)}{\partial t}.$$

Any of the m reactions can alter the value of $p(\mathbf{x}, t)$ as specified by (Equation 4.1). While the probability $p(\mathbf{x}, t)$ is a scalar, we define *the reactional probability vector* $\mathbf{p}(\mathbf{x}, t)$ such that

$$\mathbf{p}(\mathbf{x}, t) = (p_1(\mathbf{x}, t), \ldots, p_m(\mathbf{x}, t)) \in \mathbb{R}^m, \tag{4.2}$$

with $p(\mathbf{x}, t) = \mathbf{p}(\mathbf{x}, t) \cdot \mathbf{1} = (p_1(\mathbf{x}, t), \ldots, p_m(\mathbf{x}, t)) \cdot (1, \ldots, 1)^T = \sum_{k=1}^{m} p_k(\mathbf{x}, t)$. We also define the *time-derivative of the probability vector* $\partial \mathbf{p}(\mathbf{x}, t)/\partial t$ as:

$$\frac{\partial \mathbf{p}(\mathbf{x}, t)}{\partial t} \equiv \left(\frac{\partial p_1(\mathbf{x}, t)}{\partial t}, \ldots, \frac{\partial p_m(\mathbf{x}, t)}{\partial t} \right),$$

and we have:

$$\begin{aligned}
\frac{\partial p(\mathbf{x}, t)}{\partial t} &= \left(\frac{\partial p_1(\mathbf{x}, t)}{\partial t}, \ldots, \frac{\partial p_m(\mathbf{x}, t)}{\partial t} \right) \cdot (1, \ldots, 1)^T \\
&= \frac{\partial \mathbf{p}(\mathbf{x}, t)}{\partial t} \cdot \mathbf{1} = \sum_{k=1}^{m} \frac{\partial p_k(\mathbf{x}, t)}{\partial t}.
\end{aligned}$$

4.2.1   Ordering Microstates, Directional Derivative, and Discrete Divergence

Ordering Microstates. As the microstates are discrete and the stochastic jumps are dictated by the discrete increments $\{\mathbf{s}_k\}$ of reactions, we introduce *discrete partial derivative* and *discrete divergence* to describe effect of specific reactions.

First, we imposed an unambiguous order relationship $'' \prec ''$ over all microstates. We impose an ascending order on the microstates $\mathbf{x}^0 \prec \mathbf{x}^1 \prec \ldots \prec \mathbf{x}^{|\Omega|}$ that is maintained at all time, such that for each pair of states $\mathbf{x}^i \neq \mathbf{x}^j$, either $\mathbf{x}^i \prec \mathbf{x}^j$ or $\mathbf{x}^j \prec \mathbf{x}^i$ holds, but not both. There are many ways to impose such an ordering. Without loss of generality, we can first use the lexicographic order so the microstates are initially sorted by species alphabetically, and then by increasing number of molecules of the species. Other ordering schemes are also possible.

Discrete Partial Derivative. We now consider reactional component $p_k(\mathbf{x}, t)$ of the probability of the state $\mathbf{x}$ (see (Equation 4.2)). For reaction R_k, the only possible change in $\mathbf{x}$ is determined by its discrete increment of $\mathbf{s}_k$.

We first consider the case when the state $\mathbf{x} - \mathbf{s}_k$ preceding the reaction R_k and the state $\mathbf{x}$ after the reaction have the order $\mathbf{x} - \mathbf{s}_k \prec \mathbf{x}$. This also implies $\mathbf{x} \prec \mathbf{x} + \mathbf{s}_k$. In this case, the direction of the reaction coincides with the direction of the imposed ordering of the
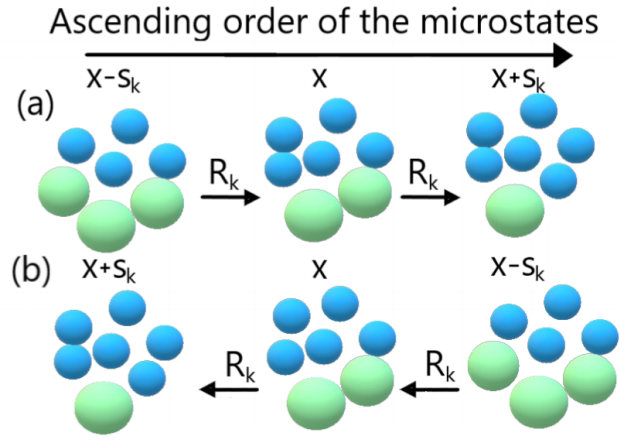
Figure 14. Ordering of microstates: a) when the order of the state preceeding the reaction R_k and the state after the reaction coincides with the imposed ascending order of microstates, we have $\mathbf{x} - \mathbf{s}_k \prec \mathbf{x} \prec \mathbf{x} + \mathbf{s}_k$; b) when the order of the state preceding the reaction R_k and the state after the reaction is in the opposite direction to the ascending order of the microstates, we have $\mathbf{x} + \mathbf{s}_k \prec \mathbf{x} \prec \mathbf{x} - \mathbf{s}_k$.

microstates (Figure 14a). We define the *discrete partial derivative* $\Delta p_k(\mathbf{x}, t)/\Delta \mathbf{x}_k$ of $p_k(\mathbf{x}, t)$ over the discrete states in the direction $\mathbf{s}_k$ of reaction R_k as:

$$\frac{\Delta p_k(\mathbf{x}, t)}{\Delta \mathbf{x}_k} \equiv p_k(\mathbf{x}, t) - p_k(\mathbf{x} - \mathbf{s}_k, t), \tag{4.3}$$

if $\mathbf{x} - \mathbf{s}_k \prec \mathbf{x} \prec \mathbf{x} + \mathbf{s}_k$.

We now consider the case when $\mathbf{x} \prec \mathbf{x} - \mathbf{s}_k$, namely, when the state $\mathbf{x} - \mathbf{s}_k$ preceding reaction R_k and the state $\mathbf{x}$ after R_k are ordered such that the after-reaction state $\mathbf{x}$ is placed prior to the before-reaction state $\mathbf{x} - \mathbf{s}_k$. This also implies $\mathbf{x} + \mathbf{s}_k \prec \mathbf{x}$ (Figure 14b). In this case, the discrete partial derivative $\Delta p_k(\mathbf{x}, t)/\Delta \mathbf{x}_k$ is defined as:

$$\frac{\Delta p_k(\mathbf{x}, t)}{\Delta \mathbf{x}_k} \equiv -(p_k(\mathbf{x}, t) - p_k(\mathbf{x} + \mathbf{s}_k, t)), \tag{4.4}$$

if $\mathbf{x} + \mathbf{s}_k \prec \mathbf{x} \prec \mathbf{x} - \mathbf{s}_k$. The negative sign "–" indicates that the direction of the reaction R_k is opposite to the direction of the imposed order of the states.

Discrete Divergence. We now introduce the *discrete divergence* $\nabla_d \cdot \mathbf{p}(\mathbf{x}, t) \in \mathbb{R}$ for the probability vector $\mathbf{p}(\mathbf{x}, t)$ over the m discrete increments $\{\mathbf{s}_k\}$ of the reactions. Applying (Equation 4.3)–(Equation 4.4) to each reactional component $p_i(\mathbf{x}, t)$ of $\mathbf{p}(\mathbf{x}, t)$ defined in (Equation 4.2), the discrete divergence $\nabla_d \cdot \mathbf{p}(\mathbf{x}, t)$ at $\mathbf{x}$ is the sum of all discrete partial derivatives along the directions of reactions:

$$\nabla_d \cdot \mathbf{p}(\mathbf{x}, t) \equiv \sum_{k=1}^{m} \frac{\Delta p_k(\mathbf{x}, t)}{\Delta \mathbf{x}_k}. \tag{4.5}$$

4.2.2 Discrete Flux and Velocity at a Fixed Microstate

Single-Reactional Flux. There are two types of reaction events affecting flux between two states $\mathbf{x}$ and $\mathbf{x}+\mathbf{s}_k$: reactions generating flux flowing from $\mathbf{x}$ to $\mathbf{x}+\mathbf{s}_k$, and reactions generating flux flowing from $\mathbf{x}+\mathbf{s}_k$ to $\mathbf{x}$. The ordering of the microstates enables unique definition of the type of events that the firing of a reaction R_k belongs to. For any two states $\mathbf{x}$ and $\mathbf{x}+\mathbf{s}_k$, only one of the two orderings is possible: we have either $\mathbf{x} \prec \mathbf{x}+\mathbf{s}_k$, or $\mathbf{x}+\mathbf{s}_k \prec \mathbf{x}$. We define the *single-reactional flux of probability* $J_k(\mathbf{x},t) \in \mathbb{R}$ for reaction R_k at microstate $\mathbf{x} \in \Omega$ as:

$$J_k(\mathbf{x},t) \equiv \begin{cases} A_k(\mathbf{x})p(\mathbf{x},t) & \mathbf{x} \prec \mathbf{x}+\mathbf{s}_k, \\[2mm] A_k(\mathbf{x}-\mathbf{s}_k)p(\mathbf{x}-\mathbf{s}_k,t) & \mathbf{x} \prec \mathbf{x}-\mathbf{s}_k. \end{cases} \tag{4.6}$$

$J_k(\mathbf{x},t)$ depicts the change in $p(\mathbf{x},t)$ at the state $\mathbf{x}$ due to one firing of reaction R_k. If $\mathbf{x} \prec \mathbf{x}+\mathbf{s}_k$, $J_k(\mathbf{x},t)$ depicts the outward flux (outflux) of probability due to one firing of reaction R_k at $\mathbf{x}$ to bring the system from $\mathbf{x}$ to $\mathbf{x}+\mathbf{s}_k$. If $\mathbf{x} \prec \mathbf{x}-\mathbf{s}_k$, $J_k(\mathbf{x},t)$ depicts the inward flux (influx) of probability due to one firing of reaction R_k at $\mathbf{x}-\mathbf{s}_k$ to bring the system from $\mathbf{x}-\mathbf{s}_k$ to $\mathbf{x}$. For any two states connected by a reaction R_k, only one of two orderings is possible as the imposed ordering of the states is unique. Therefore, the single-reactional flux can be applied to all microstates in a self-consistent manner. It also accounts for all reactions, as $J_k(\mathbf{x},t)$ can be defined for every reaction R_k. The *single-reactional R_k velocity* is defined correspondingly as:

$$v_k(\mathbf{x},t) \equiv J_k(\mathbf{x},t)/p(\mathbf{x},t).$$

Flux at Boundary States. No reactions are possible if any of the reactant molecules is unavailable, or if its copy number is inadequate. If $\mathbf{x} \prec \mathbf{x} + \mathbf{s}_k$ (Figure 14a), but $\mathbf{x} \in \partial\Omega_k$ ((Equation 4.1)), reaction R_k cannot happen, and we have $J_k(\mathbf{x}, t) = 0$. If $\mathbf{x} \prec \mathbf{x} - \mathbf{s}_k$ (Figure 14b), but $\mathbf{x} - \mathbf{s}_k \in \partial\Omega_k$ ((Equation 4.1)), reaction R_k cannot happen, and we have $J_k(\mathbf{x}, t) = 0$. We therefore have the following boundary conditions for $J_k(\mathbf{x}, t)$:

$$
J_k(\mathbf{x}, t) \equiv
\begin{cases}
0, & \mathbf{x} \prec \mathbf{x} + \mathbf{s}_k \text{ and } \mathbf{x} \in \partial\Omega_k \\
\\
0, & \mathbf{x} \prec \mathbf{x} - \mathbf{s}_k \text{ and } \mathbf{x} - \mathbf{s}_k \in \partial\Omega_k
\end{cases}
$$

Discrete Derivative of J_k. Similar to (Equation 4.3-Equation 4.4), the directional derivative of single-reactional flux $\Delta J_k(\mathbf{x}, t)/\Delta \mathbf{x}_k$ of $J_k(\mathbf{x}, t)$ along the direction $\mathbf{s}_k$ of reaction R_k is defined as follows:

$$
\frac{\Delta J_k(\mathbf{x}, t)}{\Delta \mathbf{x}_k} \equiv
\begin{cases}
A_k(\mathbf{x})p(\mathbf{x}, t) - A_k(\mathbf{x} - \mathbf{s}_k)p(\mathbf{x} - \mathbf{s}_k, t), & \text{if } \mathbf{x} - \mathbf{s}_k \prec \mathbf{x}, \\
\\
-(A_k(\mathbf{x} - \mathbf{s}_k)p(\mathbf{x} - \mathbf{s}_k, t) - A_k(\mathbf{x}\underline{-\mathbf{s}_k + \mathbf{s}_k})p(\mathbf{x}\underline{-\mathbf{s}_k + \mathbf{s}_k}, t)), & \text{if } \mathbf{x} \prec \mathbf{x} - \mathbf{s}_k.
\end{cases}
$$

With simplifications from the trivial identity $\underline{-\mathbf{s}_k + \mathbf{s}_k} = 0$, the two expressions of $\Delta J_k(\mathbf{x}, t)/\Delta \mathbf{x}_k$ can be combined into one:

$$
\begin{aligned}
\frac{\Delta J_k(\mathbf{x}, t)}{\Delta \mathbf{x}_k} &\equiv A_k(\mathbf{x})p(\mathbf{x}, t) - A_k(\mathbf{x} - \mathbf{s}_k)p(\mathbf{x} - \mathbf{s}_k, t) \\
&= -\frac{\partial p_k(\mathbf{x}, t)}{\partial t}.
\end{aligned}
\tag{4.7}
$$

Total Reactional Flux, Divergence and Continuity Equation. We now define the *total reactional flux* or *r-flux* $\mathbf{J}_r(\mathbf{x}, t)$, which describes the probability flux at a microstate $\mathbf{x}$ at time t:

$$\mathbf{J}_r(\mathbf{x}, t) \equiv (\, J_1(\mathbf{x}, t), .., \, J_m(\mathbf{x}, t)) \in \mathbb{R}^m. \tag{4.8}$$

Intuitively, the r-flux $\mathbf{J}_r(\mathbf{x}, t)$ is the vector of rate change of the probability mass at $\mathbf{x}$ in directions of all reactions. Similar to (Equation 4.5), we have the *discrete divergence* of $\mathbf{J}_r(\mathbf{x})$ at microstate $\mathbf{x}$:

$$\nabla_d \cdot \mathbf{J}_r(\mathbf{x}, t) \equiv \sum_{k=1}^{m} \frac{\Delta J_k(\mathbf{x}, t)}{\Delta \mathbf{x}_k} \tag{4.9}$$

From (Equation 4.7) we have:

$$\nabla_d \cdot \mathbf{J}_r(\mathbf{x}, t) = \sum_{k=1}^{m} [A_k(\mathbf{x}) p(\mathbf{x}, t) \\ - A_k(\mathbf{x} - \mathbf{s}_k) p(\mathbf{x} - \mathbf{s}_k, t)]. \tag{4.10}$$

Similar to its continuous version [45, 46] the discrete continuity equation for the probability mass insists that:

$$\nabla_d \cdot \mathbf{J}_r(\mathbf{x}, t) = -\frac{\partial p(\mathbf{x}, t)}{\partial t}. \tag{4.11}$$

From Eqs. (Equation 4.9), (Equation 4.11) and (Equation 1.1), it is clear that r-flux $\mathbf{J}_r(\mathbf{x}, t)$ satisfies the continuity equation. The probability mass flows simultaneously along all m directions, with the continuity equation satisfied at all time.

Single-Reactional Species Flux and Stoichiometric Projection. The reactional probability flux $J_k(\mathbf{x}, t)$ along the direction of reaction R_k defined in (Equation 4.6) can be further decomposed into components of individual species. With the predetermined stoichiometry $\mathbf{s}_k = (s_k^1, .., s_k^n)$, we define the *stoichiometric projection* of $J_k(\mathbf{x}, t)$ into the component of the $j-$th species X_j as:

$$J_k^j(\mathbf{x}, t) \equiv s_k^j J_k(\mathbf{x}, t).$$

The set of scalar components of all species $\{J_k^j(\mathbf{x}, t)\}$ can be used to form a vector $\mathbf{J}_k(\mathbf{x}, t) \in \mathbb{R}^n$, which we call *the single-reaction species flux* :

$$\mathbf{J}_k(\mathbf{x}, t) \equiv (J_k^1(\mathbf{x}, t), .., J_k^n(\mathbf{x}, t)) = \mathbf{s}_k J_k(\mathbf{x}, t) \in \mathbb{R}^n.$$

The single-reaction species velocity of probability is defined correspondingly as $\mathbf{v}_k(\mathbf{x}, t) \equiv \mathbf{J}_k(\mathbf{x}, t)/p(\mathbf{x}, t)$.

Total Species Flux and Velocity. The *total species flux* or *s-flux* $\mathbf{J}_s(\mathbf{x}, t) \in \mathbb{R}^n$ is the sum of all k single-reaction species flux vectors at a microstate $\mathbf{x} \in \mathbb{R}^n$:

$$\mathbf{J}_s(\mathbf{x}, t) \equiv \sum_{k=1}^{m} \mathbf{J}_k(\mathbf{x}, t) = \sum_{k=1}^{m} \mathbf{s}_k J_k(\mathbf{x}, t) \in \mathbb{R}^n. \tag{4.12}$$

The *total species velocity* for probability is defined accordingly as:

$$\mathbf{v}_s(\mathbf{x}, t) = \sum_{k=1}^{m} \mathbf{J}_s(\mathbf{x}, t)/p(\mathbf{x}, t). \tag{4.13}$$

The s-flux $\mathbf{J}_s(\mathbf{x}, t)$ is different from the r-flux $\mathbf{J}_r(\mathbf{x}, t)$ defined in (Equation 4.10). Reaction-centric $\mathbf{J}_r(\mathbf{x}, t) \in \mathbb{R}^m$ characterizes the total probability flux at current state in the directions of all reactions, while species-centric $\mathbf{J}_s(\mathbf{x}, t) \in \mathbb{R}^n$ sums up the contributions of every reaction to the probability flux at state $\mathbf{x}$ in the directions of all species.

4.2.3 Flux of Reversible Reaction

Flux of reversible reactions system. We now discuss probability flux in reversible reaction systems that has been previously studied [35, 130], and how they are related to fluxes formulated here. For a pair of the reactions, its directionality needs to be specified upfront, namely, which reaction is the forward reaction R^+, and which is the reversed reaction R^-:

$$R^+ : c_1 X_1 + \cdots + c_n X_n \xrightarrow{r^+} c_1' X_1 + \cdots + c_n' X_n,$$

$$R^- : c_1' X_1 + \cdots + c_n' X_n \xrightarrow{r^-} c_1 X_1 + \cdots + c_n X_n.$$
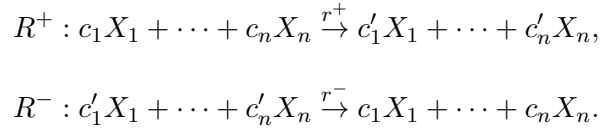
Let $\mathbf{s} = (c_1' - c_1, \ldots, c_n' - c_n)$ be the stoichiometry of reaction R^+, $-\mathbf{s}$ the stoichiometry of reaction R^-. The flux J described in [35, 130] is the net flux between $\mathbf{x}$ and $\mathbf{x} + \mathbf{s}$. It is specified as the difference between the forward flux at $\mathbf{x}$ $J^+(\mathbf{x}, t) = r^+ \prod_{l=1}^{n} \binom{x_l}{c_l} p(\mathbf{x}, t)$ generated by the forward reaction R^+ and the reverse flux at $\mathbf{x} + \mathbf{s}$ $J^-(\mathbf{x} + \mathbf{s}, t) = r^- \prod_{l=1}^{n} \binom{x_l + s_l}{c_l'} p(\mathbf{x} + \mathbf{s}, t)$ generated by the reverse reaction R^-, both connecting $\mathbf{x}$ and $\mathbf{x} + \mathbf{s}$ [35, 130]:

$$
\begin{aligned}
J(\mathbf{x}, t) = \quad & r^+ \prod_{l=1}^{n} \binom{x_l}{c_l} p(\mathbf{x}, t) \\
& - r^- \prod_{l=1}^{n} \binom{x_l + s_l}{c_l'} p(\mathbf{x} + \mathbf{s}, t).
\end{aligned}
\tag{4.14}
$$

Conversion between single-reactional species flux and flux in a pair of reversible reaction system. The flux $J(\mathbf{x}, t)$ for a pair of reversible reactions above can be related to the s-flux $\mathbf{J}_s(\mathbf{x}, t)$ of (Equation 4.12) by examining the projection of the $J(\mathbf{x}, t)$ in (Equation 4.14) to individual species. Specifically, with the stoichiometry $\mathbf{s}$, the projection of the flux of (Equation 4.14) to the component of the $j-$th species X_j is:

$$
\begin{aligned}
\mathbf{J}(\mathbf{x}, t) = \quad &\mathbf{s}J(\mathbf{x}, t) = \mathbf{s}r^+ \prod_{l=1}^{n} \binom{x_l}{c_l} p(\mathbf{x}, t) - \mathbf{s}r^- \\
&\times \prod_{l=1}^{n} \binom{x_l + s_l}{c_l'} p(\mathbf{x} + \mathbf{s}, t) \in \mathbb{R}^n.
\end{aligned}
\tag{4.15}
$$

When the direction of the forward reaction R^+ coincides with the ascending order of the states, one firing of R^+ with the stoichiometry vector $\mathbf{s}$ at the state $\mathbf{x}$ brings the system to the state $\mathbf{x} + \mathbf{s}$ in the direction of the ascending order. From (Equation 4.12), the s-flux $\mathbf{J}_s(\mathbf{x}, t)$ for (R^+, R^-) is $\mathbf{J}_s(\mathbf{x}, t) = \mathbf{s}r^+ \prod_{l=1}^{n} \binom{x_l}{c_l} p(\mathbf{x}, t) - \mathbf{s}r^- \prod_{l=1}^{n} \binom{x_l + s_l}{c_l'} p(\mathbf{x} + \mathbf{s}, t)$. In this case, the projection of the reversible reaction flux by (Equation 4.15) is identical to the s-flux by (Equation 4.12) at the state $\mathbf{x}$.

When the direction of the forward reaction R^+ is opposite to the ascending order of the states, one firing of R^- with the stoichiometry vector $-\mathbf{s}$ at the state $\mathbf{x} + \mathbf{s}$ brings the system to the state $\mathbf{x}$ in the direction of the ascending order. From (Equation 4.12), the s-flux $\mathbf{J}_s(\mathbf{x} + \mathbf{s}, t)$ for (R^+, R^-) is $\mathbf{J}_s(\mathbf{x} + \mathbf{s}, t) = \mathbf{s}r^+ \prod_{l=1}^{n} \binom{x_l}{c_l} p(\mathbf{x}, t) - \mathbf{s}r^- \prod_{l=1}^{n} \binom{x_l + s_l}{c_l'} p(\mathbf{x} + \mathbf{s}, t)$. In this case, the projection of the reversible reaction flux by (Equation 4.15) is identical to s-flux by (Equation 4.12) at the state $\mathbf{x} + \mathbf{s}$.

4.3 <u>Results</u>

Below we illustrate how time-evolving and steady-state flux and velocity fields of the probability mass can be computed for three model systems, namely, the birth-death process, the bistable Schlögl model, and the oscillating Schnakenberg system. The underlying discrete Chemical Master Equation (dCME) (Equation 1.1) of these models are solved using the recently developed ACME method [69, 84]. The resulting exact probability landscapes of these models are used to compute the flux and the velocity fields.

4.3.1 <u>The Birth and Death Process</u>

The birth-death process is a simple, but ubiquitous process of the synthesis and degradation of molecule of a single specie [69, 127]. The reaction schemes and rate constants examined in this study are specified as follows:

$$R_1: \quad \emptyset \xrightarrow{r_1} X, \quad r_1 = 1,$$

$$R_2: \quad X \xrightarrow{r_2} \emptyset, \quad r_2 = 0.025.$$
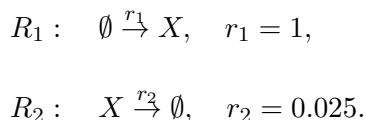
Below we use k as the index of the two reactions.

Ordering Microstates. The microstate in this system is defined by the copy number x of the molecular specie X. We order the microstates in the direction of increasing copy numbers of x, namely, $(x = 0) \prec (x = 1) \prec (x = 2) \cdots$.

Discrete Increment and Reaction Direction. Reaction R_1 brings the system from the state x to the state $x + 1$, in the direction of increasing order of the microstates. Its discrete increment

is $s_1 = 1$. Reaction R_2 brings the system from the state x to the state $x - 1$, in the direction of decreasing order of the microstates. Its discrete increment is therefore $s_2 = -1$.

Discrete Chemical Master Equation. Following (Equation 1.1), the discrete Chemical Master Equation for this system can be written as:

$$\partial p(x,t)/\partial t = \quad r_1 p(x,t) - r_1 p(x-1,t) - r_2(x+1)$$

$$\times p(x+1,t) + r_2 x p(x,t). \tag{4.16}$$

Single-Reactional Flux, Velocity and Boundary Conditions. The single-reactional flux $J_k(x,t) \in \mathbb{R}$ can be written as:

$$J_1(x,t) = r_1 p(x,t), \ \ J_2(x,t) = r_2(x+1)p(x+1,t). \tag{4.17}$$

Here $x = 0, 1, \ldots$ No special boundary conditions are required for this system, as $J_1(x,t)$ and $J_2(x,t)$ at the boundary $x = 0$ take the values specified by (Equation 4.17). The single-reactional velocity $v_k(x,t) \in \mathbb{R}$ can be written as: $v_1(x,t) = J_1(x,t)/p(x,t)$ and $v_2(x,t) = J_2(x,t)/p(x,t)$.

Discrete Partial Derivative. The imposed ordering of the microstates implies $x \prec x + s_1$, as $s_1 = 1$ and $x \prec x + 1$. By (Equation 4.3), the derivative $\Delta J_1(x, t)/\Delta x_1$ of the single-reactional flux function J_1 is:

$$
\begin{aligned}
\frac{\Delta J_1(x, t)}{\Delta x_1} &= J_1(x, t) - J_1(x - s_1, t) \\
&= r_1 p(x, t) - r_1 p(x - 1, t).
\end{aligned}
$$

The imposed ordering of the microstates also has $x \prec x - s_2$, as $s_2 = -1$ and $x \prec x + 1$. By (Equation 4.4), the derivative $\Delta J_2(x, t)/\Delta x_2$ of the single-reactional flux function J_2 is:

$$
\begin{aligned}
\frac{\Delta J_2(x, t)}{\Delta x_2} &= -(J_2(x, t) - J_2(x + s_2, t)) \\
&= -(r_2(x + 1)p(x + 1, t) - r_2(x)p(x, t)).
\end{aligned}
$$

Total Reactional Flux, Discrete Divergence, and Continuity Equation. Following (Equation 4.8), the total reactional flux $\mathbf{J}_r(x, t) \in \mathbb{R}^2$ is:

$$
\begin{aligned}
\mathbf{J}_r(x, t) &= (J_1(x, t), \ J_2(x, t)) \\
&= (r_1 p(x, t), \ r_2(x + 1)p(x + 1, t)).
\end{aligned}
$$

The total reactional velocity $\mathbf{v}_r(x, t) \in \mathbb{R}^2$ is: $\mathbf{v}_r(x, t) = \mathbf{J}_r(x, t)/p(x, t)$.

Following (Equation 4.5), the discrete divergence $\nabla_d \cdot \mathbf{J}_r(x,t)$ of $\mathbf{J}_r(x,t) \in \mathbb{R}^2$ over the discrete increments s_1 and s_2 can be written as:

$$\nabla_d \cdot \mathbf{J}_r(x,t) \equiv \sum_{k=1}^{2} \frac{\Delta J_k(x,t)}{\Delta x_k} = r_1 p(x,t) - r_1 p(x-1,t)$$
$$-r_2(x+1)p(x+1,t) + r_2(x)p(x,t). \tag{4.18}$$

Here the r-flux $J_r(x,t)$ indeed satisfies the continuity equation, as we have $\nabla_d \cdot \mathbf{J}_r(x,t) = -\partial p(x,t)/\partial t$ from Eqs. (Equation 4.11), (Equation 4.16), and (Equation 4.18).

Stoichiometry projection and single-reactional species flux. Since there is only one specie in this system, the stoichiometry projection of $J_k(x,t)$ to the specie X equals to the single-reactional species flux $\mathbf{J}_k(x,t) \in \mathbb{R}$, which can be written as:

$$\mathbf{J}_1(x,t) = r_1 p(x,t) \quad \text{and} \quad \mathbf{J}_2(x,t) = -r_2(x+1)p(x+1,t).$$

The single-reactional species velocity $\mathbf{v}_k(x,t) \in \mathbb{R}$ can be written as follows: $\mathbf{v}_1(x,t) = J_1(x,t)/p(x,t)$ and $\mathbf{v}_2(x,t) = J_2(x,t)/p(x,t)$.

Total Species Flux and Velocity. Following Eqs. (Equation 4.12)–(Equation 4.13), the s-flux $J_s(x,t)$ and the total velocity $v_s(x,t)$ are:

$$J_s(x,t) = r_1 p(x,t) - r_2(x+1)p(x+1,t),$$

$$v_s(x,t) = J_s(x,t)/p(x,t).$$

When $J_s(x,t) > 0$ and $v_s(x,t) > 0$, the probability mass moves in the direction of increasing copy number of X. This is the direction of the ascending order of microstates we imposed. When $J_s(x,t) < 0$ and $v_s(x,t) < 0$, the probability mass moves in the direction of the decreasing copy number of X. We will further use just simple flux instead of s-flux.

Overall Behavior of the Birth and Death System. We examine the behavior of the birth and death process under the initial conditions $p(x = 0)|_{t=0} = 1$ (Figure 15a, backside) and that of the uniform distribution (Figure 15d, backside).

For the initial condition of $p(x = 0)|_{t=0} = 1$, the probability landscape changes from that with a peak at $x = 0$ to that with a peak at $x = 40$ (Figure 15a). Figure 15b shows the heatmap of the flux $J_s(x,t)$, and Figure 15c the heatmap of the velocity $v_s(x,t)$. Yellow and red areas represent locations where the probability moves in the positive direction, while white areas represents locations where the flux and velocity both are close to be zero. The flux and velocity of probability mass (Figure 15b– Figure 15c) are positive at all time, indicating that the probability mass is moving only in the direction of increasing copy number of x. Moreover, when the probability is non-zero, the probability velocity remains constant at any fixed time t across different microstates. The blue line in Figure 15b– Figure 15c corresponds to the peak of the system, that changes its location from $x = 0$ to $x = 40$.

For the initial condition of the uniform distribution, the probability landscape changes from the constant line to that with a peak at $x = 40$ (Figure 15d). Figure 15e shows the heatmap of the flux $J_s(x,t)$, and Figure 15f the heatmap of the velocity $v_s(x,t)$. Blue areas represent locations where the probability mass moves in the negative direction, yellow and red areas

represent locations where the probability moves in the positive direction, while white areas represents locations where the flux and velocity both are equal to zero. Specifically, when $x < 40$, we have $J_s(x,t) > 0$ and $v_s(x,t) > 0$, namely, the probability mass moves in the direction of increasing copy number of x. In contrast, when $x > 40$, we have $J_s(x,t) < 0$ and $v_s(x,t) < 0$, indicating that the probability mass moves in the direction of decreasing copy number of x. When $x = 40$, we have $J_s(x,t) = 0$ and $v_s(x,t) = 0$. Furthermore, the probability velocity at a specific time t is different for different microstates, with the highest velocities located at the boundary of $x = 0$. The blue line in Figure 15e– Figure 15f $x = 40$ corresponds to the peak of the system, which appears starting at about $t = 5$.

To solve this problem using the ACME method, we introduced the buffer of capacity $x = 92$. At the state $x = 92$ when the buffer is exhausted, no synthesis reaction can occur. Therefore, the flux at the boundary $x = 92$ is set to zero.

Our birth and death system eventually reaches to a steady state. As expected, the same steady state probability distribution is reached from both initial conditions (shown in different scale in Figure 15a and Figure 15d). At the steady state, the probability landscape has a peak at $x = 40$. Both the velocity $v_s(x,t)$ and the flux $J_s(x,t)$ converge to zero at steady state.

4.3.2 Bistable Schlögl model

The Schlögl model is a one-dimensional bistable system consisting of an auto-catalytic network involving one molecular specie X and four reactions [128]. It is a canonical model for
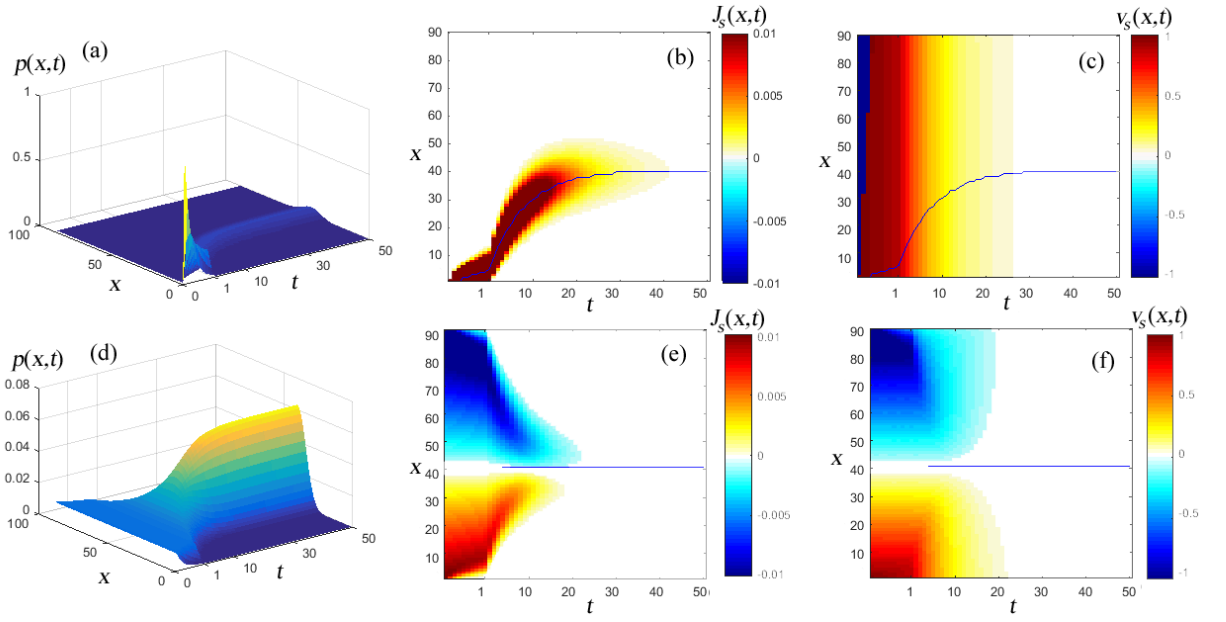
Figure 15. The time-evolving probability landscape, flux and velocity of the probability mass of the birth and death system starting from the initial conditions of $p(x = 0)|_{t=0} = 1$ (a–c) and from the initial conditions of the uniform distribution (d–f). a) and d): the probability landscape in $p(x,t)$; b) and e): the corresponding value of flux $J_s(x,t)$; c) and f): the value of velocity $v_s(x,t)$.

studying bistability and state-switching [10, 131]. The reaction schemes and kinetic constants examined in this study are specified as follows:

$$
\begin{aligned}
R_1 : \quad & A + 2X \xrightarrow{k_1} 3X, \quad k_1 = 6; \\
R_2 : \quad & 3X \xrightarrow{k_2} A + 2X, \quad k_2 = 3.6; \\
R_3 : \quad & B \xrightarrow{k_3} X, \quad k_3 = 0.25; \\
R_4 : \quad & X \xrightarrow{k_4} B, \quad k_4 = 2.95.
\end{aligned}
\tag{4.19}
$$
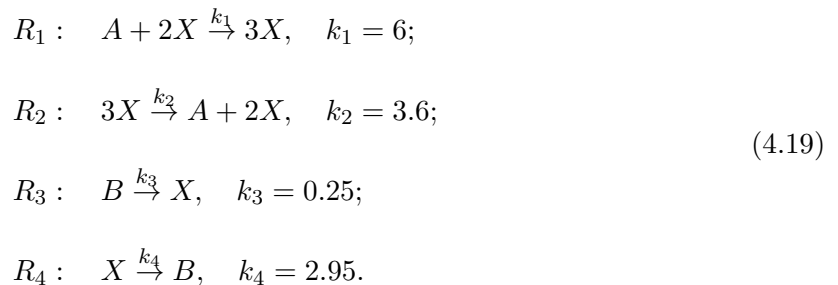
Here A and B have constant concentrations a and b, which are set to $a = 1$ and $b = 2$, respectively. We set the volume of the system to $V = 25$ [128]. The rate of reactions are specified as $r_1 = k_1/V$, $r_2 = k_2/V^2$, $r_3 = k_3 V$, $r_4 = k_4$.

Ordering Microstates. We define the microstates of this system using the copy number x of the molecular specie X. We order the microstates in the direction of increasing copy numbers of X, namely, $(x = 0) \prec (x = 1) \prec (x = 2) \cdots$.

Discrete Increment and Reaction Direction. Reactions R_1 and R_3 bring the system from the state x to the state $x + 1$, in the direction of increasing order of the microstates. Their discrete increments s_1 and s_3 are $s_1 = 1$ and $s_3 = 1$. Reactions R_2 and R_4 bring the system from the state $\mathbf{x}$ to the state $x - 1$, in the direction of decreasing order of the microstates. Their discrete increments s_2 and s_4 are therefore $s_2 = -1$ and $s_4 = -1$.

Discrete Chemical Master Equation. Following (Equation 1.1), the discrete Chemical Master Equation for this system can be written as:

$$
\begin{aligned}
\frac{\partial p(x,t)}{\partial t} =& r_1 a \frac{(x-1)(x-2)}{2} p(x-1,t) \\
&+ r_2 \frac{(x+1)x(x-1)}{6} p(x+1,t) \\
&+ r_3 b p(x-1,t) + r_4(x+1) \\
&\times p(x+1,t) - r_1 a \frac{x(x-1)}{2} p(x,t) \\
&- r_2 \frac{x(x-1)(x-2)}{6} p(x,t) \\
&- r_3 b P(x,t) - r_4 x p(x,t).
\end{aligned}
\tag{4.20}
$$

We compute the probability landscape $p(x,t)$ underlying (Equation 4.20) using the ACME method [69, 84].

Single-Reactional Flux, Velocity and Boundary Conditions. Following (Equation 4.6), the single-reactional flux $J_k(x,t) \in \mathbb{R}$ can be written as:

$$
\begin{aligned}
J_1(x,t) &= r_1 a \frac{x(x-1)}{2} p(x,t), \\
J_2(x,t) &= r_2 \frac{(x+1)x(x-1)}{6} p(x+1,t), \\
J_3(x,t) &= r_3 b p(x,t), \\
J_4(x,t) &= r_4(x+1) p(x+1,t).
\end{aligned}
$$

We have the single-reactional fluxes $J_1(x,t) = 0$ and $J_2(x,t) = 0$ on the boundarywith either $x = 0$ or $x = 1$, where reactions R_1 and R_2 cannot happen. The single-reactional fluxes $J_3(x,t)$ and $J_4(x,t)$ are as given above and do not vanish at the boundaries.

The single-reactional velocity $v_k \in \mathbb{R}$ can be written as: $v_k(x,t) = J_k(x,t)/p(x,t)$, with $k = 1, \ldots, 4$.

Discrete Partial Derivative. The imposed ordering of the microstates has $x \prec x + 1$, therefore, $x \prec x + s_1$, $x \prec x - s_2$, $x \prec x + s_3$, and $x \prec x - s_4$, as $s_1 = 1$, $s_2 = -1$, $s_3 = 1$, and $s_4 = -1$. According to Eqs. (Equation 4.3) – (Equation 4.4), the derivatives $\Delta J_k(x,t)/\Delta x_k$ of the single-reactional fluxes $\{J_k\}$ are:

$$
\begin{aligned}
\frac{\Delta J_1(x,t)}{\Delta x_1} &= J_1(x,t) - J_1(x - s_1, t) \\
&= r_1 a \frac{x(x-1)}{2} p(x,t) \\
&\quad - r_1 a \frac{(x-1)(x-2)}{2} p(x-1,t), \\
\frac{\Delta J_2(x,t)}{\Delta x_2} &= -(J_2(x,t) - J_2(x + s_2, t)) \\
&= -(r_2 \frac{(x+1)x(x-1)}{6} p(x+1,t) \\
&\quad - r_2 \frac{(x+2)(x+1)x}{6} p(x,t)), \\
\frac{\Delta J_3(x,t)}{\Delta x_3} &= J_3(x,t) - J_3(x - s_3, t) = \\
&\quad -(r_3 b p(x,t) - r_3 b p(x-1,t)), \\
\frac{\Delta J_4(x,t)}{\Delta x_4} &= -(J_4(x,t) - J_4(x + s_4, t)) \\
&= -(r_4(x+1)p(x+1,t) - r_4 x p(x,t)).
\end{aligned}
$$

Total Reactional Flux and Velocity, Discrete Divergence, and Continuity Equation. Following (Equation 4.8), the total reactional flux $\mathbf{J}_r(x, t) \in \mathbb{R}^4$ is:

$$
\begin{aligned}
\mathbf{J}_r(x, t) \quad &= (J_1(x, t), J_2(x, t), J_3(x, t), J_4(x, t)) \\
&= (r_1 a \frac{x(x-1)}{2} p(x, t), \ r_2 \frac{(x+1)x(x-1)}{6} \\
&\times p(x+1, t), \ r_3 b p(x, t), \ r_4(x+1)p(x+1, t)).
\end{aligned}
$$

The total reactional velocity $\mathbf{v}_r(x, t) \in \mathbb{R}^4$ is: $\mathbf{v}_r(x, t) = \mathbf{J}_r(x, t)/p(x, t)$.

The discrete divergence $\nabla_d \cdot \mathbf{J}_r(x, t)$ of $\mathbf{J}_r(x, t) \in \mathbb{R}^4$ over the discrete increments s_1, s_2, s_3, and s_4 can be written as:

$$
\begin{aligned}
\nabla_d \cdot \mathbf{J}_r(x, t) &= \sum_{k=1}^{4} \frac{\Delta J_k(x, t)}{\Delta x_k} \\
&= -\frac{(x-1)(x-2)}{2} r_1 a p(x-1, t) \\
&+ r_1 a \frac{x(x-1)}{2} p(x, t) \\
&- r_2 \frac{(x+1)x(x-1)}{6} p(x+1, t) \\
&+ r_2 \frac{x(x-1)(x-2)}{6} p(x, t) \\
&- r_3 b p(x-1, t) + r_3 b p(x, t) \\
&- r_4(x+1)p(x+1, t) + r_4 x p(x, t).
\end{aligned}
\tag{4.21}
$$

The flux $\mathbf{J}_R(x, t)$ indeed satisfies the continuity equation, as we have: $\nabla_d \cdot \mathbf{J}_r(x, t) = -\partial p(x, t)/\partial t$ from Eqs. (Equation 4.11), (Equation 4.20), and (Equation 4.21).

Stoichiometry projection and single-reactional species flux. Since there is only one specie x in this system, the stoichiometry projection of single-reactional flux $J_k(x,t)$ to x equals to the single-reactional species flux $\mathbf{J}_k(x,t) \in \mathbb{R}$, which can be written as:

$$\mathbf{J}_1(x,t) = r_1 a \frac{x(x-1)}{2} p(x,t),$$

$$\mathbf{J}_2(x,t) = -r_2 \frac{(x+1)x(x-1)}{6} p(x+1,t),$$

$$\mathbf{J}_3(x,t) = r_3 b p(x,t),$$

$$\mathbf{J}_4(x,t) = -r_4(x+1)p(x+1,t).$$

The single-reactional species velocities $\mathbf{v}_k \in \mathbb{R}$ is $\mathbf{v}_k(x,t) = \mathbf{J}_k(x,t)/p(x,t)$, with $k = 1,\ldots,4$.

Total Species Flux and Velocity. Following Eqs. (Equation 4.12)–(Equation 4.13), the total species flux $\mathbf{J}_s(x,t)$ and velocity $\mathbf{v}_s(x,t)$ for the four reactions are :

$$J_s(x,t) = r_1 a \frac{x(x-1)}{2} p(x,t) - r_2 \frac{(x+1)x(x-1)}{6}$$

$$\times p(x+1,t) + r_3 b p(x,t) - r_4(x+1)p(x+1,t),$$

and $v_s(x,t) = J_s(x,t)/p(x,t)$.

Overall Behavior of the Schlögl System. For the set of parameter values used in Eqs. (Equation 4.19), Schlögl model is bistable. It has two peaks at $x = 4$ and $x = 92$. In order to study how switching between the two peaks occur, we examine the behavior of the model under the initial

conditions of $p(x = 4)|_{t=0} = 1$ (Figure 16a) and the initial condition of $p(x = 92)|_{t=0} = 1$ (Figure 16d).

For the initial distribution of $p(x = 4)|_{t=0} = 1$, the probability landscape changes from that with a single peak at $x = 4$ to that with two maximum peaks at $x = 4$ and $x = 92$ (Figure 16a). Figure 16b shows the heatmap of the flux $J_s(x, t)$, and Figure 16c the heatmap of the velocity $v_s(x, t)$. Yellow and red areas represent locations where the probability moves in the positive direction, while white areas represents locations where the flux and velocity both are close to be zero. The lower blue lines in Figure 16b– Figure 16c correspond to the peak at $x = 4$. They are straight lines as the location of the peak does not change over time. Another blue line starts to appear at $x = 92$ at about $t = 3$ and corresponds to the second peak. At the same time, at around $t = 3$, we observe the appearance of a minimum of the probability landscape (red line), separating the two maximum peaks. We have $J_s(x, t) > 0$ and $v_s(x, t) > 0$, indicating that the probability moves in the direction of increasing copy number of molecules (Figure 16b– Figure 16c) in the majority of the states. In the white region, we have $J_s(x, t) = 0$ and $v_s(x, t) = 0$.

For the first initial condition of $p(x = 92)|_{t=0} = 1$, the probability landscape changes from that with a single peak at $x = 92$ to that of two peaks at $x = 92$ and $x = 4$ (Figure 16d). Figure 16e shows the heatmap of the flux $J_s(x, t)$, and Figure 16f the heatmap of the velocity $v_s(x, t)$. Blue areas represent locations where the probability mass moves in the negative direction, while white areas represents locations where the flux and velocity both are equal to zero. The top blue lines in Figure 16e– Figure 16f correspond to the peak at $x = 92$. These are
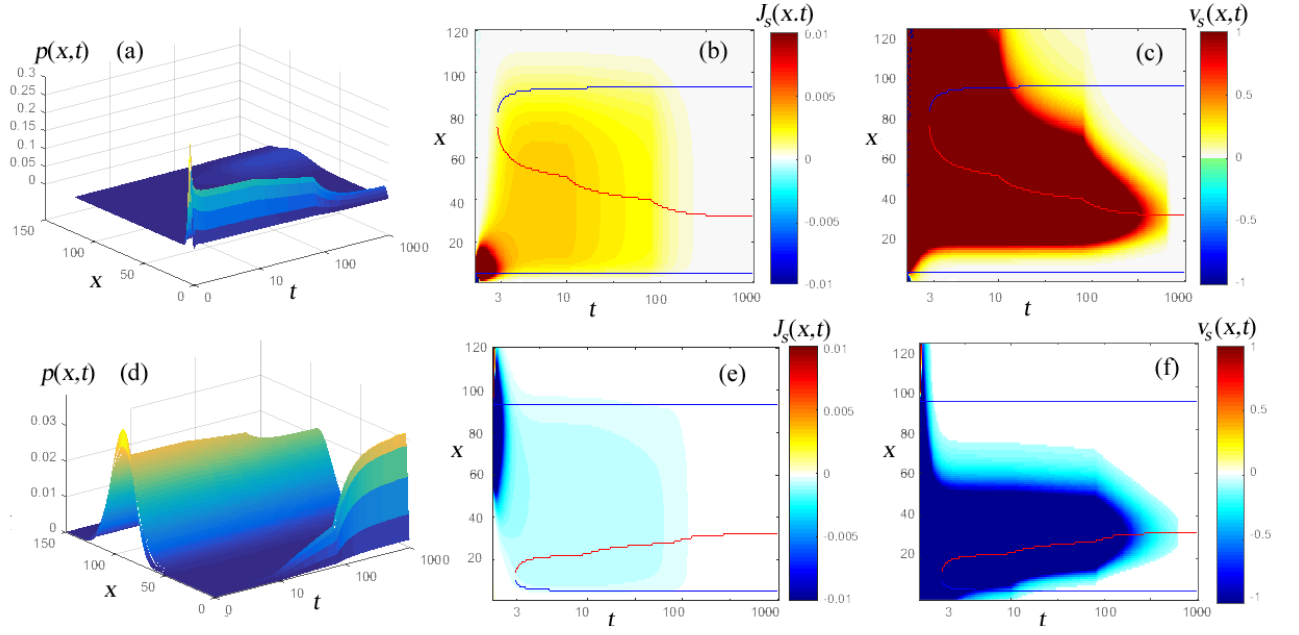
Figure 16. The time-evolving probability landscape, flux and velocity of the probability mass in the Schlögl system starting from the initial conditions of $p(x = 4)|_{t=0} = 1$ (a–c) and from the initial conditions of $p(x = 92)|_{t=0} = 1$ (d–f). a) and d): the probability landscape in $p(x, t)$; b) and e): the corresponding value of flux in $J_s(x, t)$; c) and f): the value of velocity $v_s(x, t)$.

straight lines as the location of this peak does not change over time. Another blue line starting to appear at $x = 4$ at around $t = 3$ and corresponds to the second peak. At around $t = 3$, we also observe the appearance of a minimum on the probability landscape (red line) separating the two maximum peaks. In the blue region, we have $J_s(x, t) < 0$ and $v_s(x, t) < 0$, and the probability moves in the direction of increasing copy number of molecules (Figure 16e– Figure 16f) in the majority of states. In the white region, we have $J_s(x, t) = 0$ and $v_s(x, t) = 0$.

In both cases (Figure 16), the second peak appears after about $t = 3$. We also observe that the absolute values of the flux driving the system from the system with one peak at $x = 4$ to the emergence of the second peak at $x = 92$, and from the system with one peak at $x = 92$ to the emergence of the second peak at $x = 4$ are of the same scale.

The Schlögl process eventually reaches to a steady state. As expected, the same steady state probability distribution is reached from both initial conditions. At the steady state, the probability landscape has two peaks at $x = 4$ and $x = 92$. Both the velocity $v_s(x, t)$ and the flux $J_s(x, t)$ converge to zero at the steady state.

4.3.3 Schnakenberg Model

The Schnakenberg model is a simple chemical reaction system originally constructed to study the behavior of limit cycle [3]. It provides an important model for analyzing oscillating

behavior in reaction systems [37, 90, 129]. The reaction scheme and rate constants examined in this study are specified as follows:

$$R_1: \quad A \xrightarrow{k_1} X_1, \quad k_1 = 1;$$

$$R_2: \quad X_1 \xrightarrow{k_2} \emptyset, \quad k_2 = 1;$$

$$R_3: \quad B \xrightarrow{k_3} X_2, \quad k_3 = 1;$$

$$R_4: \quad X_2 \xrightarrow{k_4} \emptyset, \quad k_4 = 10^{-2};$$

$$R_5: \quad 2X_1 + X_2 \xrightarrow{k_5} 3X_1, \quad k_5 = 1;$$

$$R_6: \quad 3X_1 \xrightarrow{k_6} 2X_1 + X_2, \quad k_6 = 10^{-2}.$$
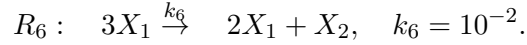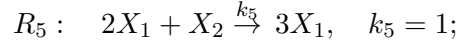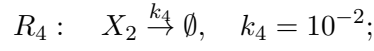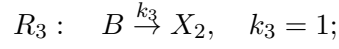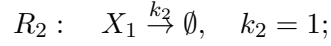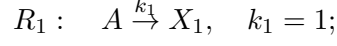
Here X_1 and X_2 are molecular species whose copy numbers x_1 and x_2 oscillate, A and B are reactants of fixed copy numbers of a and b, respectively. The volume of the system V is set to $V = 10^{-2}$ [3]. The rate of reactions are specified as $r_1 = k_1$, $r_2 = k_2$, $r_3 = k_3$, $r_4 = k_4$, $r_5 = k_5/V^2$, $r_6 = k_6/V^2$.

Ordering Microstates. The microstate $\mathbf{x} = (x_1, x_2)$ in this system is defined by the ordered pair of copy numbers x_1 and x_2 of the molecular species X_1 and X_2. We impose the ascending order of the microstates first in the direction of the increasing copies of X_1. At fixed value of X_1, we then sort the states in the order of increasing copy number of X_2. We therefore have $(x_1 = 0, x_2 = 0) \prec (x_1 = 0, x_2 = 1) \prec (x_1 = 0, x_2 = 2) \prec \cdots \prec (x_1 = 1, x_2 = 0) \prec (x_1 = 1, x_2 = 1) \cdots$.

TABLE VI. Schnakenberg system reactions stoichiometry

Reactions	R_1	R_3	R_5	R_2	R_4	R_6
Increments	$\mathbf{s}_1 = (1,0)$	$\mathbf{s}_3 = (0,1)$	$\mathbf{s}_5 = (1,-1)$	$\mathbf{s}_2 = (-1,0)$	$\mathbf{s}_4 = (0,-1)$	$\mathbf{s}_6 = (-1,1)$

Discrete Increment and Reaction Direction. The discrete increments $\mathbf{s}_1$, $\mathbf{s}_3$, and $\mathbf{s}_5$ of reactions R_1, R_3, and R_5 that bring the system in the direction of increasing order of the microstates and the discrete increments $\mathbf{s}_2$, $\mathbf{s}_4$, and $\mathbf{s}_6$ of reactions R_2, R_4, and R_6 that bring the system in the direction of the decreasing order of the microstates are listed in Table Table VI.

Discrete Chemical Master Equation. Following (Equation 1.1), the discrete Chemical Master Equation for the system can be written as:

$$
\begin{aligned}
\frac{\partial p(\mathbf{x}, t)}{\partial t} =\ & -r_1 a p(x_1, x_2, t) + r_1 a p(x_1 - 1, x_2, t) \\
& - r_2 x_1 p(x_1, x_2, t) + r_2(x_1 + 1)p(x_1 + 1, x_2, t) \\
& - r_3 b p(x_1, x_2, t) + r_3 b p(x_1, x_2 - 1, t) \\
& + r_4(x_2 + 1)p(x_1, x_2 + 1, t) - r_4 x_2 p(x_1, x_2, t) \\
& + r_5 \frac{(x_1 - 1)(x_1 - 2)x_2}{2} p(x_1 - 1, x_2 + 1, t) \\
& - r_5 \frac{x_1(x_1 - 1)x_2}{2} p(x_1, x_2, t) \\
& + r_6 \frac{(x_1 - 1)x_1(x_1 + 1)}{6} p(x_1 + 1, x_2 - 1, t) \\
& - r_6 \frac{x_1(x_1 - 1)(x_1 - 2)}{6} p(x_1, x_2, t).
\end{aligned}
\tag{4.22}
$$

We compute the probability landscape $p(\mathbf{x}, t)$ underlying (Equation 4.20) using the ACME method [69, 84].

Single-Reactional Flux, Velocity and Boundary Conditions. The single-reactional flux $J_k(\mathbf{x}, t) \in \mathbb{R}$ can be written as:

$$J_1(\mathbf{x}, t) = r_1 a p(x_1, x_2, t),$$

$$J_2(\mathbf{x}, t) = r_2(x_1 + 1)p(x_1 + 1, x_2, t),$$

$$J_3(\mathbf{x}, t) = r_3 b p(x_1, x_2, t),$$

$$J_4(\mathbf{x}, t) = r_4(x_2 + 1)p(x_1, x_2 + 1, t),$$

$$J_5(\mathbf{x}, t) = r_5 \frac{(x_1 - 1)(x_1 - 2)x_2}{2}$$

$$\times p(x_1 - 1, x_2 + 1, t),$$

$$J_6(\mathbf{x}, t) = r_6 \frac{(x_1 - 1)x_1(x_1 + 1)}{6}$$

$$\times p(x_1 + 1, x_2 - 1, t).$$

(4.23)

We have the single-reactional fluxes $J_5(\mathbf{x}, t) = 0$ and $J_6(\mathbf{x}, t) = 0$ on the boundary with either $\mathbf{x} = (0, 0)$ or $\mathbf{x} = (1, 0)$, where reactions R_5 and R_6 cannot happen. The other single-reactional fluxes are as given above and do not vanish at the boundaries.

The single-reactional velocity $v_k(\mathbf{x}, t) \in \mathbb{R}$ can be written as: $v_k(\mathbf{x}, t) = J_k(\mathbf{x}, t)/p(\mathbf{x}, t)$.

Discrete Partial Derivative. The imposed ordering of the microstates has $\mathbf{x} \prec \mathbf{x} + \mathbf{s}_1$, $\mathbf{x} \prec \mathbf{x} - \mathbf{s}_2$, $\mathbf{x} \prec \mathbf{x} + \mathbf{s}_3$, $\mathbf{x} \prec \mathbf{x} - \mathbf{s}_4$, $\mathbf{x} \prec \mathbf{x} + \mathbf{s}_5$, and $\mathbf{x} \prec \mathbf{x} - \mathbf{s}_6$. According to Eqs. (Equation 4.3)–

(Equation 4.4), the derivatives $\Delta J_k(\mathbf{x}, t)/\Delta \mathbf{x}_k$ of the single-reactional fluxes J_k can be written

as:

$$\frac{\Delta J_1(\mathbf{x}, t)}{\Delta \mathbf{x}_1} = J_1(\mathbf{x}, t) - J_1(\mathbf{x} - \mathbf{s}_1, t)$$

$$= r_1 a p(x_1, x_2, t) - r_1 a p(x_1 - 1, x_2, t),$$

$$\frac{\Delta J_2(\mathbf{x}, t)}{\Delta \mathbf{x}_2} = -(J_2(\mathbf{x}, t) - J_2(\mathbf{x} + \mathbf{s}_2, t)) = -(r_2(x_1 + 1)$$

$$\times p(x_1 + 1, x_2, t) - r_2 x_1 p(x_1, x_2, t)),$$

$$\frac{\Delta J_3(\mathbf{x}, t)}{\Delta \mathbf{x}_3} = J_3(\mathbf{x}, t) - J_3(\mathbf{x} - \mathbf{s}_3, t)$$

$$= r_3 b p(x_1, x_2, t) - r_3 b p(x_1, x_2 - 1, t)),$$

$$\frac{\Delta J_4(\mathbf{x}, t)}{\Delta \mathbf{x}_4} = -(J_4(\mathbf{x}, t) - J_4(\mathbf{x} + \mathbf{s}_4, t)) = -(r_4(x_2 + 1)$$

$$\times p(x_1, x_2 + 1, t) - r_4 x_2 p(x_1, x_2, t)),$$

$$\frac{\Delta J_5(\mathbf{x}, t)}{\Delta \mathbf{x}_5} = J_5(\mathbf{x}, t) - J_5(\mathbf{x} - \mathbf{s}_5, t)$$

$$= r_5 \frac{x_1(x_1 - 1)x_2}{2} p(x_1, x_2, t)$$

$$- r_5 \frac{(x_1 - 1)(x_1 - 2)x_2}{2} p x_1 - 1, x_2 + 1, t)/2,$$

$$\frac{\Delta J_6(\mathbf{x}, t)}{\Delta \mathbf{x}_6} = -(J_6(\mathbf{x}, t) - J_6(\mathbf{x} + \mathbf{s}_6, t))$$

$$= -(r_6 \frac{(x_1 - 1)x_1(x_1 + 1)}{6} p(x_1 + 1, x_2 - 1, t)$$

$$- r_6 \frac{x_1(x_1 - 1)(x_1 - 2)}{6} p(x_1, x_2, t)).$$

Total Reactional Flux and Velocity, Discrete Divergence, and Continuity Equation. Following (Equation 4.8), the total reactional flux $\mathbf{J}_r(\mathbf{x}, t) \in \mathbb{R}^6$ is:

$$\mathbf{J}_r(\mathbf{x}, t) = (\quad J_1(\mathbf{x}, t),\ J_2(\mathbf{x}, t),\ J_3(\mathbf{x}, t),$$

$$J_4(\mathbf{x}, t),\ J_5(\mathbf{x}, t),\ J_6(\mathbf{x}, t)),$$

where $\{J_k(\mathbf{x}, t)\}$ are as specified in (Equation 4.23). The total reactional velocity $\mathbf{v}_r(\mathbf{x}, t) \in \mathbb{R}^6$ is: $\mathbf{v}_r(\mathbf{x}, t) = \mathbf{J}_r(\mathbf{x}, t)/p(\mathbf{x}, t)$.

The discrete divergence $\nabla_d \cdot \mathbf{J}_r(\mathbf{x}, t)$ of the r-flux $\mathbf{J}_r(\mathbf{x}, t) \in \mathbb{R}^6$ over the discrete increments $\mathbf{s}_k$ can be written as:

$$\nabla_d \cdot \mathbf{J}_r(\mathbf{x}, t) = \sum_{k=1}^{6} \frac{\Delta J_k(\mathbf{x}, t)}{\Delta \mathbf{x}_k}. \tag{4.24}$$

The r-flux $\mathbf{J}_r(\mathbf{x}, t)$ indeed satisfies the continuity equation, as we have $\nabla_d \cdot \mathbf{J}_r(\mathbf{x}, t) = -\partial p(\mathbf{x}, t)/\partial t$ from Eqs. (Equation 4.11), (Equation 4.22), and (Equation 4.24)

Stoichiometry projection and single-reactional species flux. The single-reactional flux $J_k(\mathbf{x}, t)$ along the direction of reaction R_k can be decomposed into components of individual species using the predetermined stoichiometry $\mathbf{s}_k = (s_k^1,\ s_k^2)$. The x_1 and x_2 components of *stoichiometric projections* of $J_k(\mathbf{x}, t)$ are listed in Table Table VII. The single-reactional species flux is formed as follows:

$$\mathbf{J}_k(\mathbf{x}, t) \equiv (J_k^1(\mathbf{x}, t),\ J_k^2(\mathbf{x}, t)), \quad k = 1, \ldots, 6, \tag{4.25}$$

TABLE VII. Schnakenberg system reactional flux stoichiometry projections

Reaction	$J_k^1(x_1, x_2, t) = s_k^1 J_k(x_1, x_2, t)$	$J_k^2(x_1, x_2, t) = s_k^2 J_k(x_1, x_2, t)$
R_1	$r_1 a p(x_1, x_2, t)$	0
R_2	$-r_2(x_1 + 1)p(x_1 + 1, x_2, t)$	0
R_3	0	$r_3 b p(x_1, x_2, t)$
R_4	0	$-r_4(x_2 + 1)p(x_1, x_2 + 1, t)$
R_5	$r_5 \frac{(x_1-1)(x_1-2)x_2}{2} p(x_1 - 1, x_2 + 1, t)$	$-r_5 \frac{(x_1-1)(x_1-2)x_2}{2} p(x_1 - 1, x_2 + 1, t)$
R_6	$-r_6 \frac{(x_1-1)x_1(x_1+1)(x_1-2)}{6} p(x_1 + 1, x_2 - 1, t)$	$r_6 \frac{(x_1-1)x_1(x_1+1)(x_1-2)}{6} p(x_1 + 1, x_2 - 1, t)$

where $J_k^1(\mathbf{x}, t)$ and $J_k^2(\mathbf{x}, t)$ listed in Table Table VII. The single-reactional species velocity $\mathbf{v}_k(\mathbf{x}, t) \in \mathbb{R}^{\not\models}$ is $\mathbf{v}_k(\mathbf{x}, t) \equiv \mathbf{J}_k(\mathbf{x}, t)/p(\mathbf{x}, t)$.

Total Species Flux and Velocity. Following Eqs. (Equation 4.12)–(Equation 4.13), the total flux $\mathbf{J}_s(\mathbf{x}, t) \in \mathbb{R}^2$ is $\mathbf{J}_s(\mathbf{x}, t) = \sum_{k=1}^{m} \mathbf{J}_k(\mathbf{x}, t)$, where $\{\mathbf{J}_k\}$ as specified in (Equation 4.25). The total species velocity $\mathbf{v}_s(\mathbf{x}, t) \in \mathbb{R}^2$ is: $\mathbf{v}_s(\mathbf{x}, t) = \mathbf{J}_s(\mathbf{x}, t)/p(\mathbf{x}, t)$.

Overall Behavior of Schnakenberg System. We examine the behavior of the Schnakenberg system with $(a, b) = (10, 50)$ under two initial conditions, namely, that of the uniform distribution and $p(\mathbf{x} = (0, 0))|_{t=0} = 1$. We computed the time-evolving probability landscape $p = p(\mathbf{x}, t)$ using the ACME method [69, 84].

For the uniform distribution, the probability landscape in $-\log p(\mathbf{x}, t)$ at time $t = 0.5$ is shown in Figure 17a, where high probability regions are in blue. Its overall shape takes the
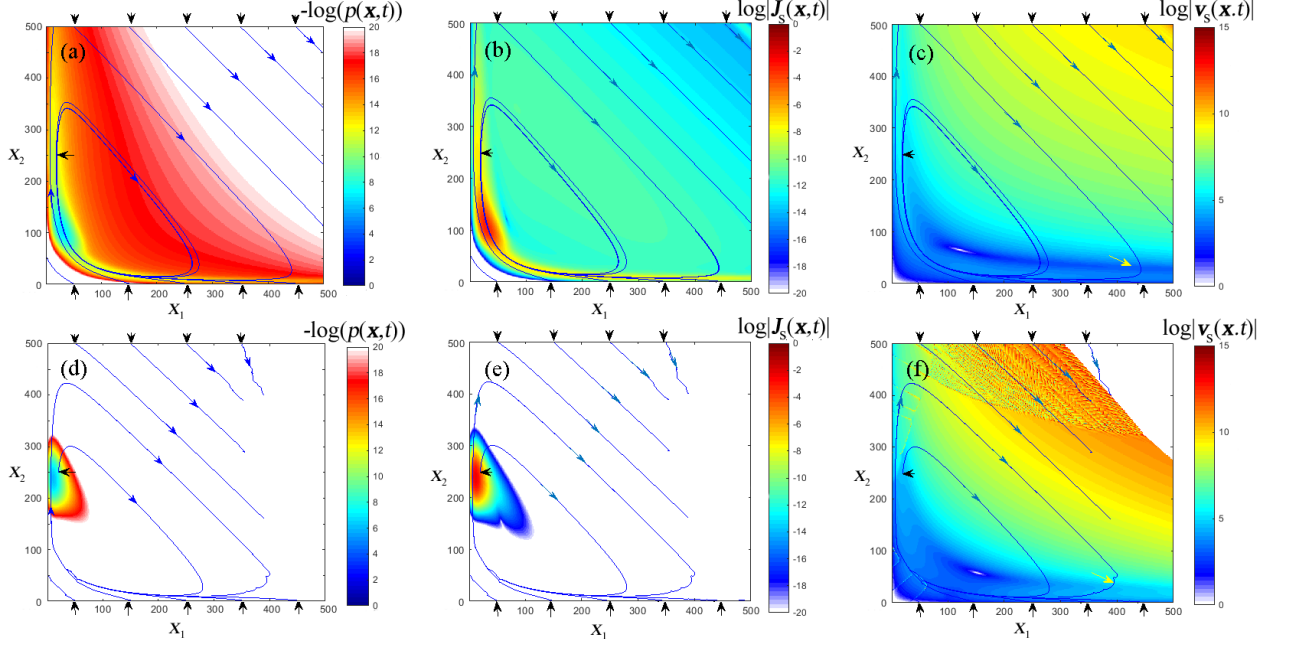
Figure 17. The time-evolving probability landscape, flux, and velocity of probability mass in the Schnakenberg system with $(a,\ b) = (10,\ 50)$ at $t = 0.5$, starting from the uniform distribution (a–c) and from the initial conditions of $p(\mathbf{x} = (0,0))|_{t=0} = 1$ (d–f). a) and d): the probability landscape in $-\log(p(\mathbf{x}, t))$; b) and e): the corresponding value of flux in $\log|\mathbf{J}_s(\mathbf{x}, t)|$; c) and f): the log absolute value of velocity $\log|\mathbf{v}_s(\mathbf{x}, t)|$.
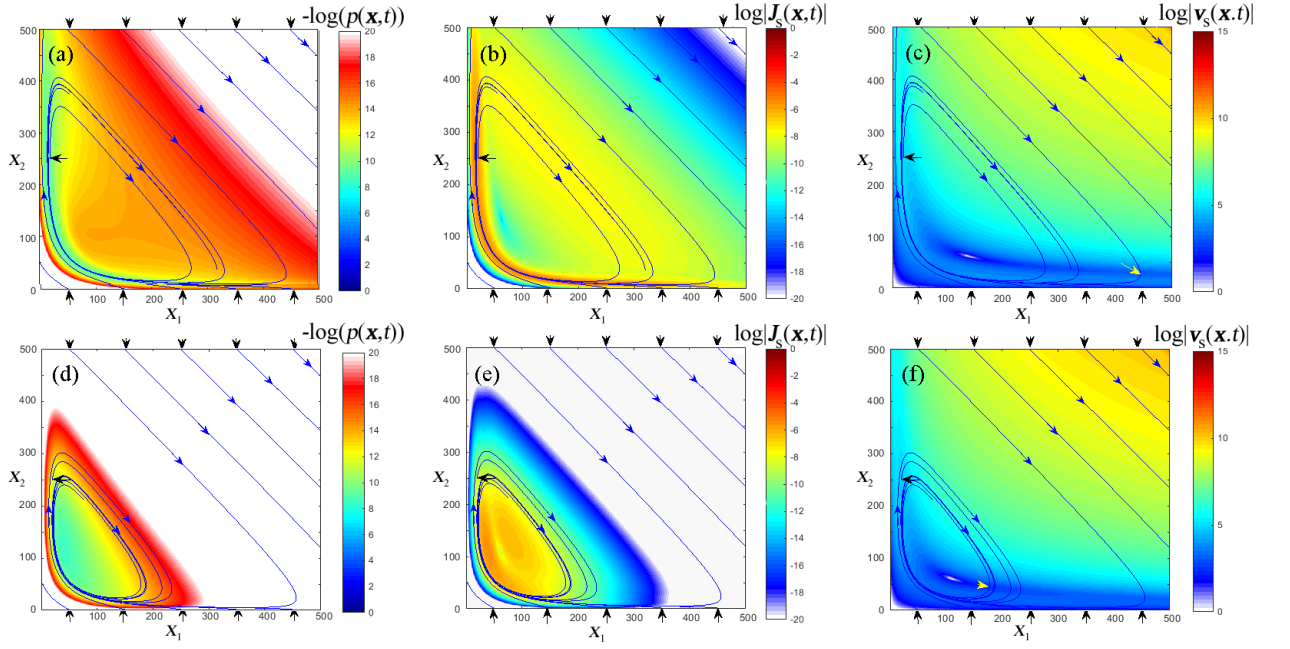
Figure 18.   The steady-state probability landscape, flux, and velocity of probability mass in the Schnakenberg system with $(a,\ b) = (10,\ 50)$ (a–c) and $(a, b) = (20, 40)$ (d–f). a) and d): the probability landscape in $-\log(p(\mathbf{x}, t))$; b) and e): the corresponding values of flux in $\log|\mathbf{J}_s(\mathbf{x}, t)|$; c) and f): the log absolute value of velocity $\log|\mathbf{v}_s(\mathbf{x}, t)|$.

form of closed valley, which is similar to an earlier study based on a Fokker-Planck model [37]. The trajectories of the flux field $\mathbf{J}_s(\mathbf{x}, t)$ at time $t = 0.5$ in the space of the copy-numbers from different starting locations (marked by black arrows at top and bottom) are shown in blue on Figure 17- Figure 18. These trajectories depict the directions of the movement of the probability mass at different locations after traveling from the starting points. The heatmaps of the flux in $\log|J_s(\mathbf{x}, t)|$ and the velocity in $\log|v_s(\mathbf{x}, t)|$ are shown in Figure 17b and Figure 17c, respectively. The flux lines are closed curves and are overall smooth. These closed flux lines reflect the oscillatory nature of the reaction system. The velocity has larger values at locations where the flux trajectories are straight lines (green and yellow region in the upper right corner, Figure 17c), but drops significantly when the trajectories make down-right turns (light and dark blue in the lower right corner, marked with an yellow arrow).

For the initial conditions of $p(\mathbf{x} = (0,0))|_{t=0} = 1$, $-\log p(\mathbf{x}, t)$ at time $t = 0.5$ is shown in Figure 17d, where high probability regions (blue) is located at a small neighborhood around $\mathbf{x} = (0, 250)$. The heatmaps of the flux in $\log|J_s(\mathbf{x}, t)|$ and the velocity in $\log|v_s(\mathbf{x}, t)|$ are shown in Figure 17e and Figure 17f, respectively. The flux lines are closed curves and are overall smooth. The oscillating flux lines appear again (Figs Figure 17d– Figure 17f), but not all form closed curves. Specifically, all flux lines which start at the upper region ($x_2 = 500$) become broken-off in the mid-region, where the probability mass becomes negligible, resulting in negligible flux as well, with its absolute value close to be zero. The maximum of the flux is reached at the peak of the probability landscape (Figure 17e). The heatmap of the probability velocity exhibits a similar pattern as that of uniform distribution (Figure 17f vs. Figure 17c).

The color palettes encoding the values of the velocity $\log |v_s(\mathbf{x}, t)|$ are not-smooth (Figure 17f). This is likely due to small numerical values of probability in this region.

We then examined the steady state behavior of the system at two conditions of the copy numbers of species A and B: $(a, b) = (10, 50)$ and $(a, b) = (20, 40)$. The probability landscape in $-\log(p(\mathbf{x}, t))$ for $(a, b) = (10, 50)$ shown in Figure 18a exhibits similar shape to that of Fig Figure 17. The probability values are higher in locations near the left $(x_1 = 0)$ and lower $(x_2 = 0)$ boundaries. The flux lines (Figure 18a- Figure 18c) move from the upper left corner to the lower right corner, and then make sharp right turns until reaching the neighborhood near the origin. Subsequently, they make right turns again and move upward, until the cycles are closed. These closed flux curves move along the contours on the probability landscape. The absolute values of the flux (Figure 18b) are largest near the boundaries of the probability surfaces $(x_1 = 0$ and $x_2 = 0$, red/orange colored ridge) and nextly along the flux lines on the diagonal. The flux has small values in the region above the diagonal (cyan and blue). The heatmap of the velocity (Figure 18c) exhibit a different pattern, with its value dropping significantly in the small blue arch (see region pointed by the yellow arrow), where flux lines make turns in the lower region.

The probability landscape in $-\log(p(\mathbf{x}, t))$ for $(a, b) = (20, 40)$ is shown in Figure 18d. While exhibiting overall similar pattern to that of $(a, b) = (10, 50)$, the high probability regions is more concentrated in locations near the lower-left (Figure 18d). The flux lines (Figure 18d– f) are similar to those of $(a, b) = (10, 50)$ corner, but oscillate around much smaller contour,

where $x_1 \leq 200$ and $x_2 \leq 300$. The close cycles of flux lines also move along the contours on the probability landscape.

The results obtained here are generally consistent with that obtained using a Fokker-Planck flux model computed from a landscape constructed using Gillespie simulations [7, 37]. For example, the directions of the flux lines are the same. However, there are some differences. While the flux lines from the Fokker-Planck model exhibit oscillating behavior even in the boundary regions where $x_1 < 2$ or $x_2 < 2$, where reactions R_5 and R_6 cannot occur hence no oscillating flux are physically possible. No such inconsistency exist in our model. Furthermore, the system considered here is much larger, with hundreds of copies of X_1 and X_2 involed, whereas < 10 copies of X_1 and X_2 were considered in [37].

4.4   Conclusions

In this study, we introduce new formulations of discrete flux and discrete velocity for an arbitrary mesoscopic reaction system. Specifically, we redefine the derivative and divergence operators based on the discrete nature of chemical reactions. We then introduce the discrete form of continuity equation for the systems of reactions. We define two types of discrete flux, with their relationship specified. The reactional discrete flux satisfies the continuity equation and describes the behavior of the system evolving along directions of reactions. The species flux directly describes the dynamic behavior of the reactions such as the transfer of probability mass in the state space. Our discrete flux model enables the construction of the global time-evolving and steady-state flow-maps of fluxes in all directions at every microstate. Furthermore, it can be used to tag the fluxes of outflow and inflow of probability mass as reactions proceeds.

In addition, we can now impose boundary conditions, allowing exact quantification of vector fields of the discrete flux and discrete velocity anywhere in the discrete state space, without the difficulty of enforcing artificial reflecting conditions at the boundaries [126]. We note that the accurate construction of the discrete probability flux, velocity, and their global flow-maps requires the accurate calculation of the time-evolving probability landscape of the reaction network. This is made possible by using the recently developed ACME method [69, 84].

As a demonstration, we computed the time-evolving probability flux and velocity fields for three model systems, namely, the birth-death process, the bistable Schlögl model, and the oscillating Schnakenberg system. We showed how flux and velocities converge to zero when the system reaches the steady-state in the birth-death process and the Schlögl models. We also showed that the flux and velocity trajectories in the Schnakenberg system converge to the oscillating contours of the steady-state probability landscape, similar to an earlier study [37], although there are important differences. Overall, the general framework of discrete flux and velocity and the methods introduced here can be applied to other networks and dynamical processes involving stochastic reactions. These applications can be useful in quantification of dynamic changes of probability mass, identification as well as characterization of mechanism where movement of probability mass drives the system towards the steady-state. They may also aid in our understanding of the mechanisms that determined the non-equilibrium steady state of many reaction systems.

CHAPTER 5

DISCRETE AND CONTINUOUS MODELS OF PROBABILITY FLUX ON SWITCHING DYNAMICS: A CASE STUDY OF THE TOGGLE-SWITCH SYSTEM

5.1 Introduction

The toggle switch network plays important roles in molecular decision-making and is widely found in nature [13, 132–135]. Toggle switch has been studied extensively, with its stability, dynamics, switching mechanisms, and most-probable paths analyzed through outlfow probability fluxes [31], quasi-potential landscapes reconstruction [136], as well as weighted-ensemble trajectory simulations using the string-method [32]. Modeling of toggle switch network remains of significant interest, and in this chapter we will apply discrete and continuous models of probability flux to study switching dynamics in toggle switch.

While continuous and discrete models have been used to analyze gene regulatory networks, it is important to understand their applicability and limitations. For analysis of probability landscape, models based on ordinary differential equations generally are not applicable to stochastic systems, for example, those with low copy numbers of molecules or with large differences in reaction rates [16, 49, 137, 138]. Models based on continuous approximations of the discrete Markov jump processes also have limitations. For example, Fokker-Planck models may fail to capture certain important properties of a stochastic network, such as the presence

of multistability in networks with slow switching between the ON and the OFF states [30]. When systems are far from equilibrium, the probability landscape constructed using models based on continuous approximations is also of inadequate accuracy [75]. In general, the applicability and validity of the type of the model for a specific network model to be investigated individually [5, 11, 16, 30, 75, 126, 137–139]. However, assessing the applicability and limitations of different models in analysis of probability flux and velocity is more challenging. A major difficulty is to examine fluxes and velocities in a consistent manner across different models.

In this study, we examine applicability and limits of three classes of flux models. The first class of flux is the universal discrete flux models based on dCME developed in [38]. It enables the construction of the global time-evolving and steady-state flow-maps of fluxes in all directions at every microstate, while satisfying the discrete version of the continuity equation. Furthermore, it can be used to tag the fluxes of outflow and inflow of probability mass as reactions proceeds. Previous discrete models of probability flux and velocity introduced in [31, 119–121, 124] have limitations: some are applicable only to analysis of single reactional trajectories [119, 120], some can only specify partial flux functions [31, 121], and some are restricted to special systems of simple single-species reactions [124]. Flux and velocity fields can also be obtained in self-consistent manner using Fokker-Planck models [36, 37, 39, 41, 118, 122], where the continuity equation of probability is satisfied [45, 46]. Our second class of models are the Fokker-Planck models, which are obtained from the Kramers-Moyal expansion of the discrete Chemical Master Equation following [37]. Our third class of models is a new probability based on ordinary differential equations novel deterministic approach called the Liouville flux model. Models

based on ordinary differential equations (ODEs) are often used in analysis of metabolic networks such as the difference between forward and backward reaction fluxes [140–142], although these are concentration fluxes rather than probability fluxes. While deterministic models of flux are generally not applicable to gene regulatory networks, Liouville flux approach, based on the law of mass action, models the probability flux using precomputed probability distribution at individual states. This model of the flux can be directly compared with flux model based on SDE formulations such as Fokker-Planck models of probability flux.

For computing the probability landscape, we employ the recently developed ACME method [69, 84] to solve the dCME underlying the stochastic network and obtain its exact time-evolving probability landscapes. This eliminates potential problems arising from inadequate sampling, where rare events of low probability are difficult to quantify using techniques such as the stochastic simulations algorithm (SSA) [7, 9, 10, 77].

In this work we examine the details of the probability fluxes obtained with these three models, using the network model of the toggle switch system as an example. We examine the behavior of fluxes in this network, obtained under two conditions, namely, i) when the binding rates of the genes by transcription factors are much larger than the unbinding rates, with which the system exhibiting three stable states, and ii) when the unbinding rates are of the same magnitude as binding rates, with which the system exhibiting four stable states at the steady state. Our results show that the fluxes computed with these three differenting models all exhibit similar behavior under the first condition, but exhibit markedly different behavior under the second condition, where the stochastic fluctuations are significant. Furthermore, we

show that the behavior of universal discrete stochastic flux can uncover oscillating behavior at the non-equilibrium steady state of the system due to fluctuations between binding and unbinding events, while Fokker-Planck and Liouville models fail to capture this phenomenon. We further show oscillations in well known oscillating negative feedback motif. We also study the phenomena of gene duplication in two level toggle switch network with transcription and translation reactions explicitely modeled.

This chapter is organized as follows. We first introduce the three flux models: the Liouville flux model for an arbitrary biochemical reaction system, the Fokker-Planck flux model, based on the Kramers-Moyal expansion of dCME, and the universal discrete flux model. We study analytically the origin of differences among these three models of fluxes. We then illustrate the differences in probability fluxes for the examples of toggle switch and negative feedback.

5.2   Models of Probability Flux

5.2.1   Liouville Flux Model

Here we introduce a Liouville flux model based on the ordinary differential equations for mean concentrations of molecules from mass action. It is a set of forward differential equation, in which the increment in the mean concentration of molecular specie over time $\partial \langle \mathbf{X} \rangle / \partial t$, given $\partial t \rightarrow 0$, defines the Liouville velocity $\mathbf{v}_L(\langle \mathbf{X} \rangle, t)$ of reactional mass of the average molecular concentration $\langle \mathbf{X} \rangle$:

$$\mathbf{v}_L(\langle \mathbf{X} \rangle, t) = \mathbf{F}(\langle \mathbf{X} \rangle, t),$$

where the components of $\mathbf{F}(\langle \mathbf{X} \rangle, t)$ are defined by (Equation 1.5).

To compare with other flux models, we now restrict the values of the function $\mathbf{v}_L = \mathbf{v}_L(\langle \mathbf{X} \rangle, t)$ to the discrete state space Ω, where the probability values are computed using the ACME method [69, 84]. We use the notation $\mathbf{v}_L \equiv \mathbf{v}_L(\mathbf{x}, t)$.

The Liouville flux is defined in the discrete subset Ω of the continuous space U as:

$$\mathbf{J}_L(\mathbf{v}, t) \equiv \mathbf{v}_L(\mathbf{v}, t)p(\mathbf{x}, t). \tag{5.1}$$

5.2.2 Fokker-Planck Flux Model

We rewrite the right hand side of (Equation 1.6) by taking the operator $\nabla_{\mathbf{x}}(\cdot)$ outside the parenthesis:

$$\frac{\partial p(\mathbf{x}, t)}{\partial t} = -\nabla_{\mathbf{x}} \sum_{k=1}^{m} \frac{\mathbf{s}_k}{V} [A_k(\mathbf{x})p(\mathbf{x}, t)$$

$$-\frac{\mathbf{s}_k}{2V} \nabla_{\mathbf{x}} A_k(\mathbf{x})p(\mathbf{x}, t)].$$

From (Equation 4.10), the flux for the Fokker-Planck model $J_{FP}(\mathbf{x}, t)$ can be written as follows:

$$J_{FP}(\mathbf{x}, t) \equiv \sum_{k=1}^{m} \frac{\mathbf{s}_k}{V} [A_k(\mathbf{x})p(\mathbf{x}, t) - \frac{\mathbf{s}_k}{2V} \nabla_{\mathbf{x}} A_k(\mathbf{x})p(\mathbf{x}, t)]. \tag{5.2}$$

The Fokker-Plank flux (Equation 5.2) has two components: the drift term of $\sum_{k=1}^{m} \mathbf{s}_k A_k(\mathbf{x})$ $\times p(\mathbf{x}, t)/V$ and the diffusion term of $\sum_{k=1}^{m} \mathbf{s}_k \nabla_{\mathbf{x}} A_k(\mathbf{x})p(\mathbf{x}, t)/(2V^2)$. The drift term is driven by chemical reactions occurring at $\mathbf{x}$. The diffusion term approximates linearly the stochastic fluctuations of the system.

5.2.3   Universal Discrete Flux Model

A model of discrete flux was recently introduced in reference [38]. As it can account for both reactional flux and species flux, we call it *the universal discrete flux model*. Briefly, we define an unambiguous order of ascending relationship " $\prec$ " over all microstates, and have them ordered as $\mathbf{x}^0 \prec \mathbf{x}^1 \prec \ldots \prec \mathbf{x}^{|\Omega|}$ [38]. The *single-reactional flux of probability* $J_k(\mathbf{x}, t) \in \mathbb{R}$ for reaction R_k is:

$$J_k(\mathbf{x}, t) \equiv \begin{cases} A_k(\mathbf{x})p(\mathbf{x}, t), & \mathbf{x} \prec \mathbf{x} + \mathbf{s}_k, \\ \\ A_k(\mathbf{x} - \mathbf{s}_k)p(\mathbf{x} - \mathbf{s}_k, t), & \mathbf{x} \prec \mathbf{x} - \mathbf{s}_k. \end{cases}$$

$J_k(\mathbf{x}, t)$ depicts the change in $p(\mathbf{x}, t)$ at the state $\mathbf{x}$ due to one firing of reaction R_k. If $\mathbf{x} \prec \mathbf{x} + \mathbf{s}_k$, $J_k(\mathbf{x}, t)$ describes the outflux at $\mathbf{x}$ due to one firing of reaction R_k. If $\mathbf{x} \prec \mathbf{x} - \mathbf{s}_k$, $J_k(\mathbf{x}, t)$ describes the influx to $\mathbf{x}$ due to one firing of reaction R_k.

The *total reactional flux* or *r-flux* $\mathbf{J}_r(\mathbf{x}, t)$, which describes the probability flux at a microstate $\mathbf{x}$ at time t, is defined as [38]: $\mathbf{J}_r(\mathbf{x}, t) \equiv (J_1(\mathbf{x}, t), \cdots, J_m(\mathbf{x}, t)) \in \mathbb{R}^m$. Intuitively, the r-flux $\mathbf{J}_r(\mathbf{x}, t)$ is the vector of rate change of the probability mass at $\mathbf{x}$ in directions of all reactions. $J_r(\mathbf{x}, t)$ satisfies the discrete continuity equation (**??**). Details can be found in [38].

The *total species flux*, or *s-flux*, $\mathbf{J}_s(\mathbf{x}, t) \in \mathbb{R}^n$ is the sum of the stoichiometry projections of m single-reaction species flux vectors at a microstate $\mathbf{x} \in \mathbb{R}^n$:

$$\mathbf{J}_s(\mathbf{x}, t) = \sum_{k=1}^{m} \mathbf{s}_k J_k(\mathbf{x}, t) \in \mathbb{R}^n. \tag{5.3}$$

5.2.4   Differences between flux models

We now compare the three flux models and define analytically their differences.

5.2.4.1   Difference between Discrete Flux and Fokker-Planck Flux

The difference between the universal discrete flux of (Equation 5.3) and the Fokker-Planck flux of (Equation 5.2) at $V = 1$ is:

$$
\begin{aligned}
\mathbf{J}_s(\mathbf{x}, t) - \mathbf{J}_{FP}(\mathbf{x}, t) = & \sum_{\substack{k:\, \mathbf{x} \prec \\ \mathbf{x} + \mathbf{s}_k}} \mathbf{s}_k [A_k(\mathbf{x})p(\mathbf{x}, t) - A_k(\mathbf{x})p(\mathbf{x}, t) + \frac{\mathbf{s}_k}{2}\nabla_{\mathbf{x}} A_k(\mathbf{x})p(\mathbf{x}, t)] \\
& + \sum_{\substack{k:\, \mathbf{x} \prec \\ \mathbf{x} - \mathbf{s}_k}} [\mathbf{s}_k A_k(\mathbf{x} - \mathbf{s}_k)p(\mathbf{x} - \mathbf{s}_k, t) - A_k(\mathbf{x})p(\mathbf{x}, t) + \frac{\mathbf{s}_k}{2}\nabla_{\mathbf{x}} A_k(\mathbf{x})p(\mathbf{x}, t)] \\
= & \sum_{\substack{k:\, \mathbf{x} \prec \\ \mathbf{x} + \mathbf{s}_k}} \mathbf{s}_k \left[\frac{1}{2}\mathbf{s}_k \nabla_{\mathbf{x}} A_k(\mathbf{x})p(\mathbf{x}, t) \right] \\
& + \sum_{\substack{k:\, \mathbf{x} \prec \\ \mathbf{x} - \mathbf{s}_k}} \mathbf{s}_k \left[A_k(\mathbf{x} - \mathbf{s}_k)p(\mathbf{x} - \mathbf{s}_k, t) - A_k(\mathbf{x})p(\mathbf{x}, t) + \frac{\mathbf{s}_k}{2}\nabla_{\mathbf{x}} A_k(\mathbf{x})p(\mathbf{x}, t) \right].
\end{aligned}
$$

$$(5.4)$$

For reactions generating discrete flux out-flowing from $\mathbf{x}$ to $\mathbf{x} + \mathbf{s}_k$, the values of the discrete flux and Fokker-Planck flux differ only in the diffusion term $\mathbf{s}_k \left[\mathbf{s}_k \nabla_{\mathbf{x}} A_k(\mathbf{x})p(\mathbf{x}, t) \right]/2$ of the Fokker-Planck flux. For reactions generating flux flowing-in from $\mathbf{x} - \mathbf{s}_k$ to $\mathbf{x}$, the discrete flux and Fokker-Planck flux differs in both the diffusion term and the drift term.

We examine the difference further by taking the linear Taylor expansion: $A_k(\mathbf{x} - \mathbf{s}_k)p(\mathbf{x} - \mathbf{s}_k, t) \approx A_k(\mathbf{x})p(\mathbf{x}, t) - \mathbf{s}_k \nabla_{\mathbf{x}} A_k(\mathbf{x})p(\mathbf{x}, t)$. While the gradient of the flux defines the change of

the probability with time from the continuity equation, we now skip the second-order term of the Taylor expansion. (Equation 5.4) now becomes:

$$
\begin{aligned}
\mathbf{J}_s(\mathbf{x}, t) - \mathbf{J}_{FP}(\mathbf{x}, t) = & \sum_{\substack{k:\, \mathbf{x} \prec \\ \mathbf{x}+\mathbf{s}_k}} \mathbf{s}_k \left[\frac{1}{2} \mathbf{s}_k \nabla_{\mathbf{x}} A_k(\mathbf{x}) p(\mathbf{x}, t) \right] \\
& + \sum_{\substack{k:\, \mathbf{x} \prec \\ \mathbf{x}-\mathbf{s}_k}} \mathbf{s}_k \left[A_k(\mathbf{x}) p(\mathbf{x}, t) - \mathbf{s}_k \nabla_{\mathbf{x}} A_k(\mathbf{x}) p(\mathbf{x}, t) \right. \\
& \qquad \left. - A_k(\mathbf{x}) p(\mathbf{x}, t) + \frac{1}{2} \mathbf{s}_k \nabla_{\mathbf{x}} A_k(\mathbf{x}) p(\mathbf{x}, t) \right] \\
= & \sum_{\substack{k:\, \mathbf{x} \prec \\ \mathbf{x}+\mathbf{s}_k}} \mathbf{s}_k \left[\frac{1}{2} \mathbf{s}_k \nabla_{\mathbf{x}} A_k(\mathbf{x}) p(\mathbf{x}, t) \right] - \sum_{\substack{k:\, \mathbf{x} \prec \\ \mathbf{x}-\mathbf{s}_k}} \mathbf{s}_k \left[\frac{1}{2} \mathbf{s}_k \nabla_{\mathbf{x}} A_k(\mathbf{x}) p(\mathbf{x}, t) \right].
\end{aligned}
$$

Hence, the drift terms for both fluxes are the same and equal to $A_k(\mathbf{x}) p(\mathbf{x}, t)$. The difference in these two flux models resides only in the noise encoded by the diffusion term.

5.2.4.2 Difference between Liouville Flux and Fokker-Planck Flux

The difference between the Fokker-Planck flux from (Equation 5.2) and the Liouville flux from (Equation 5.1), given $V = 1$, is:

$$
\mathbf{J}_{FP}(\mathbf{x}, t) - \mathbf{J}_L(\mathbf{x}, t) = \sum_k \left[\mathbf{s}_k \left(A_k(\mathbf{x}) p(\mathbf{x}, t) - \frac{1}{2} \mathbf{s}_k \nabla_{\mathbf{x}} A_k(\mathbf{x}) p(\mathbf{x}, t) \right) - \mathbf{F}(\mathbf{x}, t) p(\mathbf{x}, t) \right]. \tag{5.5}
$$

In this case, difference exists in both the drift term and the diffusion terms.

However, for the special case when there is only one type of reactant and $|\mathbf{s}_k| = 1$, we have $\mathbf{F}(\mathbf{x}, t) p(\mathbf{x}, t) = \mathbf{s}_k A_k(\mathbf{x}) p(\mathbf{x}, t)$. In this case, the drift terms of the two fluxes are the same.

5.2.4.3   Difference between Discrete Flux and Liouville Flux

The difference between the discrete universal flux ((Equation 5.3)) and the Liouville flux ((Equation 5.1)) is:

$$
\begin{aligned}
\mathbf{J}_s(\mathbf{x}, t) - \mathbf{J}_L(\mathbf{x}, t) = &\sum_{\substack{k: \, \mathbf{x} \prec \\ \mathbf{x} + \mathbf{s}_k}} [\mathbf{s}_k A_k(\mathbf{x}) p(\mathbf{x}, t) - \mathbf{F}(\mathbf{x}, t) p(\mathbf{x}, t)] \\
&+ \sum_{\substack{k: \, \mathbf{x} \prec \\ \mathbf{x} - \mathbf{s}_k}} [\mathbf{s}_k A_k(\mathbf{x} - \mathbf{s}_k) p(\mathbf{x} - \mathbf{s}_k, t) - \mathbf{F}(\mathbf{x}, t) p(\mathbf{x}, t)].
\end{aligned}
\tag{5.6}
$$

We consider the special case of reactions involving only a single molecules species of reactants with $|\mathbf{s}_k| = 1$. We have $\mathbf{F}(\mathbf{x}, t) p(\mathbf{x}, t) = \mathbf{s}_k A_k(\mathbf{x}) p(\mathbf{x}, t)$. For reactions with probability flux flowing from $\mathbf{x}$ to $\mathbf{x} + \mathbf{s}_k$ ($\mathbf{x} - \mathbf{s}_k \prec \mathbf{x}$) both fluxes are the same. For reactions with probability flux flowing from $\mathbf{x} - \mathbf{s}_k$ to $\mathbf{x}$, we can examine this difference by taking the linear terms of the Taylor expansion of $A_k(\mathbf{x} - \mathbf{s}_k) p(\mathbf{x} - \mathbf{s}_k, t) \approx A_k(\mathbf{x}) p(\mathbf{x}, t) - \mathbf{s}_k \nabla_{\mathbf{x}} A_k(\mathbf{x}) p(\mathbf{x}, t)$. (Equation 5.6) now becomes:

$$
\begin{aligned}
\mathbf{J}_s(\mathbf{x}, t) - \mathbf{J}_L(\mathbf{x}, t) = &\sum_{\substack{k: \, \mathbf{x} \prec \\ \mathbf{x} - \mathbf{s}_k}} [\mathbf{s}_k A_k(\mathbf{x} - \mathbf{s}_k) p(\mathbf{x} - \mathbf{s}_k, t) - \mathbf{F}(\mathbf{x}, t) p(\mathbf{x}, t)] \\
= &\sum_{\substack{k: \, \mathbf{x} \prec \\ \mathbf{x} - \mathbf{s}_k}} [\mathbf{s}_k (A_k(\mathbf{x}) p(\mathbf{x}, t) - \mathbf{s}_k \nabla_{\mathbf{x}} A_k(\mathbf{x}) p(\mathbf{x}, t) - \mathbf{F}(\mathbf{x}, t) p(\mathbf{x}, t)].
\end{aligned}
$$

In this case, under the assuption $\mathbf{F}(\mathbf{x}, t) p(\mathbf{x}, t) = \mathbf{s}_k A_k(\mathbf{x}) p(\mathbf{x}, t)$, the drift terms are the same. The fluxes differ only in the diffusion term $\mathbf{s}_k \nabla_{\mathbf{x}} A_k(\mathbf{x}) p(\mathbf{x}, t)$.

5.3   The Multistable Toggle Switch Model

5.3.1   Network and Reactions

In this study, we employ a detailed model of toggle switch [17, 143], where the binding and unbinding reactions are explicitly modeled. This is different from the simplified model used in several other studies [13, 144, 145].

There are six molecular species in our model: genes G_x and G_y, which express proteins P_X and P_Y, as well as protein-DNA complexes $\overline{G}_x$ and $\overline{G}_y$, with protein P_Y bound on gene G_x and protein P_X bound on gene G_y, respectively (Figure 19). The dimer of protein product P_X of gene G_x inhibits the activity of gene G_y and the dimer of protein product P_Y of gene G_y inhibits the activity of gene G_x.
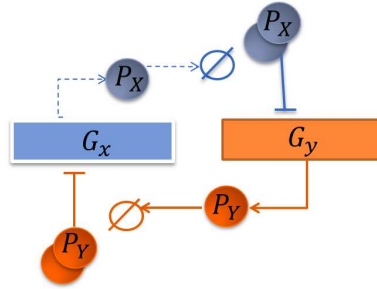
Figure 19.   Schematic representation of the toggle switch genetic network.

The molecular reactions of the network are listed below:

$$R_1 : G_x \xrightarrow{s_X} G_x + P_X, \quad R_2 : G_y \xrightarrow{s_Y} G_y + P_Y,$$

$$R_3 : P_X \xrightarrow{d_X} \emptyset, \quad\quad\quad R_4 : P_Y \xrightarrow{d_Y} \emptyset,$$

$$R_5 : 2P_X + G_y \xrightarrow{b_y} \overline{G}_y, \quad R_6 : 2P_Y + G_x \xrightarrow{b_x} \overline{G}_x,$$

$$R_7 : \overline{G}_y \xrightarrow{u_y} 2P_X + G_y, \quad R_8 : \overline{G}_x \xrightarrow{u_x} 2P_Y + G_x.$$

(5.7)
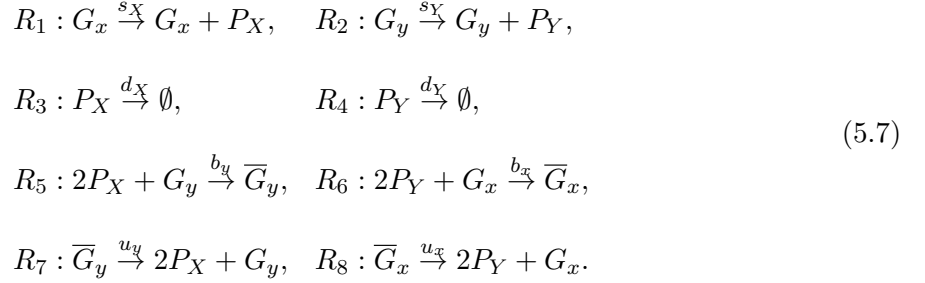
The microstate of the system is defined as an ordered quadruplet (X, Y, x, y) of copy numbers

of P_X, P_Y, G_x, and G_y, respectively. The copy numbers of bound genes $\overline{G}_x$ and $\overline{G}_y$ are denoted

as $\overline{x}$ and $\overline{y}$. Correspondingly, $x = 1 - \overline{x}$ and $y = 1 - \overline{y}$, as there is only one copy of each of genes

x and y in this system. The binding states of the two operator sites are denoted as "On-On"

when $x = 1$ and $y = 1$, "On-Off" when $x = 1$ and $y = 0$, "Off-On" when $x = 0$ and $y = 1$, and

"Off-Off", when $x = 0$ and $y = 0$.

There are a number of stochastic processes encoded in this network. The synthesis of

proteins P_X and P_Y from gene G_x and gene G_y are represented by reactions R_1 and R_2,

respectively, with the rates of $s_x = s_y$. The degradation of proteins P_X and P_Y are represented

by reactions R_3 and R_4, respectively, with the rates $d_x = d_y$. Reaction R_5 represents the

binding of two copies of protein P_X to the promoter site of G_y to form a protein-DNA complex

$\overline{G}_y$, with rate b_y. Reaction R_7 represents the unbinding of the complex $\overline{G}_y$, at a rate of u_y.

Similarly, reaction R_6 represents the binding of two copies of protein P_Y to the promoter site

of G_x to form a protein-DNA complex $\overline{G}_x$, with rate b_x. Reaction R_8 represents the unbinding

of the complex $\overline{G}_x$ at a rate of u_x.

Here we consider the scenario where gene regulation is much slower than protein synthesis and degradation. In eukaryotic cells, epigenetics processes such as histone modification and DNA methylation can reduce the binding rates of transcription factors to their targeting DNA sites. Recent findings in the genetic switch of bacteriophage λ showed that slower binding and unbinding also occur in bacterials cells [146]. In the regime of slow binding and unbinding reactions, where b_y and b_x (reactions R_5 and R_6) and u_y and u_x (reactions R_7 and R_8) are smaller than synthesis rates s_x and s_y (reactions R_1 and R_2), there are up to four peaks of probability over certain regions of protein copy numbers, in which one of the two genes is expressed and the other gene repressed, as well as two genes being either expressed or repressed simultaneously, as reported in [17].

A well-known phenomenon in genetic switches such as the toggle switch system is the extreme stability of the "On-Off" or the "Off-On" states: it is exceedingly rare for the system to switch from one of these two stable states to the other, even in the presence of perturbations [135, 147]. In this study, we show that the toggle switch can switch frequently between these two stable states without external perturbations. Further, these switching events can turn the toggle switch into an stochastically oscillating system.

5.3.2   Fluxes in the Toggle Switch Network

For the universal discrete flux, we first impose an ascending order on the microstates in the direction of the increasing copies of X. At a fixed value of X, we then order the states in increasing copy number of Y. Subsequently, we order the states in increasing copy number of x, and lastly, in the order of increasing copy number of y. Following (Equation 5.3), components

of the universal discrete stochastic fluxes at the microstate (X, Y, x, y) in the directions of X and Y are:

$$J_s(X, Y, x, y)_X = s_X x p(X, Y, x, y) - d_X(X+1)p(X+1, Y, x, y) + 2u_y(1-y)p(X, Y, x, y)$$

$$- b_y(1-y)(X+1)(X+2)p(X+2, Y, x, 1-y),$$

$$J_s(X, Y, x, y)_Y = s_Y y p(X, Y, x, y) - d_Y(Y+1)p(X, Y+1, x, y) + 2u_x x p(X, Y, x, y)$$

$$- b_x(1-x)(Y+1)(Y+2)p(X, Y+2, 1-x, y)).$$

Following (Equation 5.1), the Liouville flux at the microstate (X, Y, x, y) is:

$$\mathbf{J}_L(X, Y, x, y)_X = p(X, Y, x, y)(s_X x - d_x X + u_y(1-y) - b_y X^2 y),$$

$$\mathbf{J}_L(X, Y, x, y)_Y = p(X, Y, x, y)(s_Y y - d_y Y + u_x(1-x) - b_x Y^2 x).$$

Following (Equation 5.2), the Fokker-Planck flux for $V = 1$ at the microstate (X, Y, x, y) is:

$$\mathbf{J}_{FP}(X, Y, x, y)_X = s_X x - d_X X + 2u_y(1-y) - b_y X(X-1)y)p(X, Y, x, y)$$

$$+ \frac{1}{2}\nabla_X[s_X x + d_X X + 2u_y(1-y) + 2b_y X(X-1)y)p(X, Y, x, y)],$$

$$\mathbf{J}_{FP}(X, Y, x, y)_Y = s_Y y - d_Y Y + 2u_x(1-x) - b_x Y(Y-1)x)p(X, Y, x, y)$$

$$+ \frac{1}{2}\nabla_Y[s_Y y + d_Y Y + 2u_x(1-x) + 2b_x Y(Y-1)x)p(X, Y, x, y)].$$

5.3.3   Probability flux and velocity in toggle switch with strong promoter binding

We first consider the system with strong promoter binding. The binding rates are $b_x = b_y = 1 \times 10^{-2}$, the synthesis rates $s_x = s_y = 50$, the degradation rates $d_x = d_y = 1$, and unbinding rates $u_x = u_y = 0.1$. At the steady state, there are three probability peaks located at $(X, Y) = (0, 0)$, $(50, 0)$, $(0, 50)$, corresponding to the states of the genes G_x and G_y of "Off-Off" ($x = 0$, $y = 0$), "On-Off" ($x = 1$, $y = 0$), and "Off-On" ($x = 0$, $y = 1$) (Figure 20A, Figure 20D and Figure 20G).

The steady state probability distribution of reactions R_1, R_3 given $x = 1$ ((Equation 5.7)), which are birth-and-death processes, is the Poisson distribution with the maximum at its expected value of $X = s_X/d_X = 50$ [148]. Similarly, the steady state probability distribution for the birth-and-death process of reactions R_2, R_4, given $y = 1$, ((Equation 5.7)), is the Poisson distribution with the maximum at its expected value of $Y = s_Y/d_Y = 50$. When the binding reaction has a higher propensity than unbinding, the genetic state "On-On" where ($x = 1$, $y = 1$) disappears. With the multiplication factor of the copy number of molecules, this occurs even when b_y is an order of magnitude smaller than u_y. From computed $p(X, Y, x, y)$, we show its projection to the plane of (X, Y) in Figure 20, namely, we show $p(X, Y) = p(X, Y, 0, 0) + p(X, Y, 1, 0) + p(X, Y, 0, 1) + p(X, Y, 1, 1)$. Similarly, $\boldsymbol{J}_s(X, Y)$, $\boldsymbol{J}_L(X, Y)$, $\boldsymbol{J}_{FP}(X, Y)$, $\boldsymbol{v}_s(X, Y)$, $\boldsymbol{v}(X, Y)$, and $\boldsymbol{v}_{FP}(X, Y)$ are shown as projected in Figure 20.

The steady-state probability landscapes in $-\log p(\mathbf{x}, t)$ is shown in Figure 20A, Figure 20D and Figure 20G, with high probability regions in red, and regions where probability is close

to zero in white. The trajectories of the flux field at the steady state are shown in blue for the universal discrete flux field $\mathbf{J}_s(\mathbf{x}, t)$ in Figure 20A– Figure 20C, for the Liouville flux field $\mathbf{J}_L(\mathbf{x}, t)$ in Figure 20D– Figure 20F, and for the Fokker-Planck flux field $\mathbf{J}_{FP}(\mathbf{x}, t)$ in Figure 20G– Figure 20I. In Figures Figure 20B, Figure 20E and Figure 20H, regions with large absolute values of flux are shown in purple, and regions with small absolute values of flux are shown in turquoise blue. In Figures Figure 20C, Figure 20F and Figure 20I, regions with large absolute values of flux are shown in turquoise blue regions with small absolute values of velocity are shown in purple.

5.3.3.1 Universal Discrete Stochastic Flux and Velocity fields

The heatmaps of the universal discrete probability flux in $\log|J_s(\mathbf{x}, t)|$ and velocity in $\log|v_s(\mathbf{x}, t)|$ (Figure 20B and Figure 20C, respectively) show that locations with larger flux values also have higher probability. The states "Off-Off", "On-Off", and "Off-On" can be regarded as attractors of the probability flux. The flux lines converge to the states "On-Off" and "Off-On", after first reaching the state "Off-Off". Figure 20C of $\log|\boldsymbol{v}_s(X, Y)|$ shows that the velocity has larger values at locations where the flux trajectories are close to be straight lines (purple regions, Figure 20C), but drops significantly when the trajectories make turns (turquoise regions, Figure 20C).

5.3.3.2 Liouville Flux for the Toggle Switch Network

In the heat map of Liouville flux, larger values are associated with higher probabilities (Figure 20D – Figure 20E). The states "On-Off" and "Off-On" are the sinks. The velocity and flux lines converge to the states "On-Off" and "Off-On", after first reaching towards the
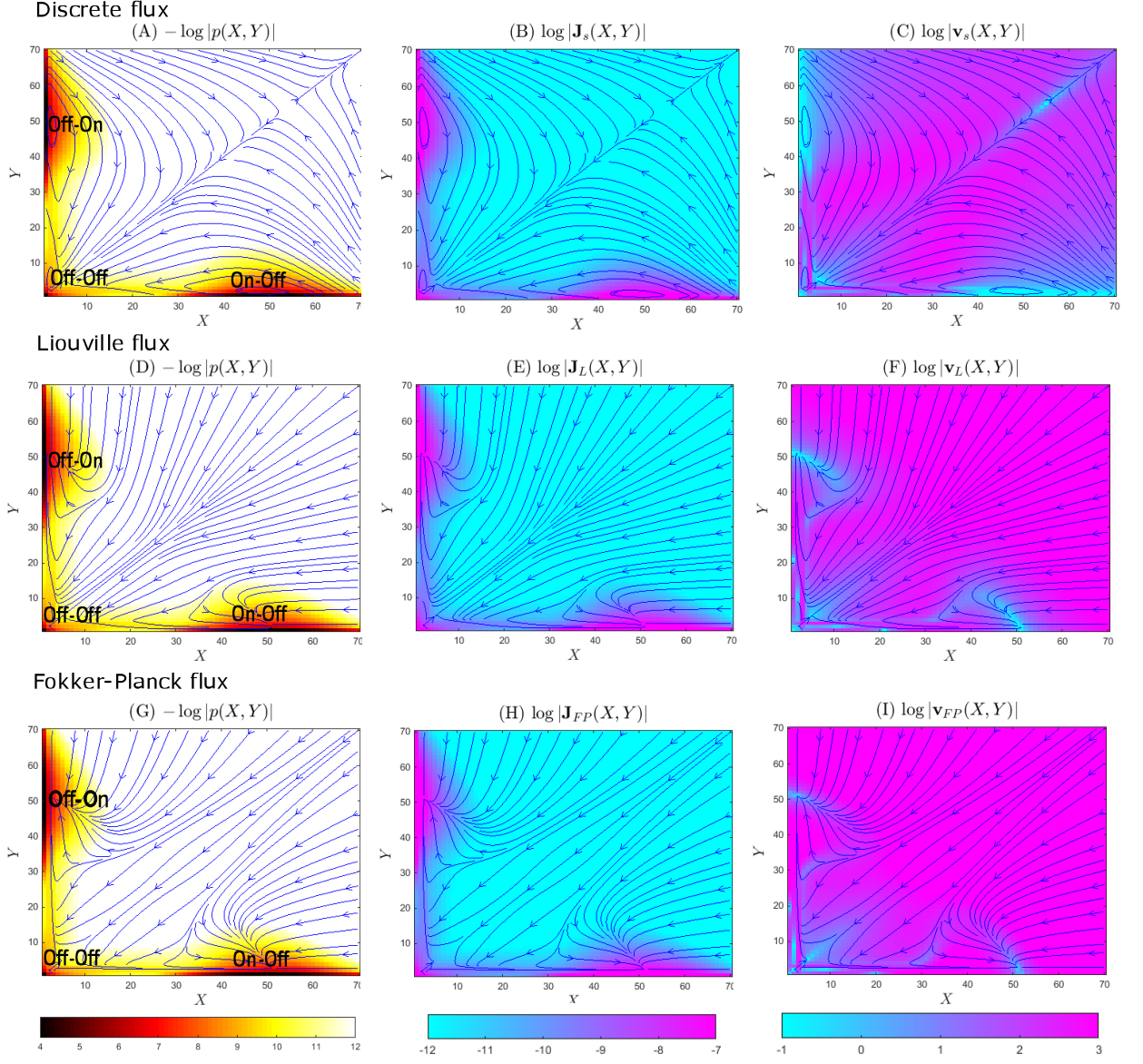
Figure 20. The probability landscapes, fluxes, and velocities of the toggle switch system with strong promoter binding ($b = 1 \times 10^{-2}$) at the steady state. Probability value is given by the color scale, and the fluxes/velocities are shown in blue solid lines. The discrete stochastic flux model with landscape in $-\log(p(x,y))$ (A), flux in $\log|\mathbf{J}_s(x,y)|$ (B), and velocity in $\log|\mathbf{v}_s(x,y)|$ (C); the Liouville flux model with landscape in $-\log(p(x,y))$ (D), flux in $\log|\mathbf{J}_L(x,y)|$ (E), and velocity in $\log|\mathbf{v}_L(x,y)|$ (F); and the Fokker-Planck flux model with landscape in $-\log(p(x,y))$ (G), flux in $\log|\mathbf{J}_{FP}(x,y)|$ (H), and velocity in $\log|\mathbf{v}_{FP}(x,y)|$ (I).

state "Off-Off". These patterns are the same as that of the universal discrete flux (Figure 20A).

Detailed examination shows that the flux sinks are located at the states $(X = 50, Y = 0)$ and $(X = 0, Y = 50)$. These are local maxima of the probability landscape. The absolute value of velocity function $\log |\boldsymbol{v}_L(X, Y)|$ shows that the probability velocity has larger values at locations where the flux trajectories are close to be straight lines (purple regions, Figure 20F), but drops significantly when the trajectories make turns (turquoise regions, Figure 20F).

The Liouville flux trajectories and the universal discrete flux trajectories depict similar behavior of the system. The flux lines converge to the states "Off-On" and "On-Off" after going through the state "Off-Off", an intermediate attractor of the flux.

However, there are significant differences. The states "Off-On" and "On-Off" are single states with $(X = 50, Y = 0)$ and $(X = 0, Y = 50)$ in Liouville flux (Figure 20F),but they are set of states in discrete flux close to $(X = 50, Y = 0)$ and $(X = 0, Y = 50)$, where the flux trajectories fluctuate (Figure 20C). The flux trajectories for the Liouville flux start at the source located at $(+\infty, +\infty)$. This is different from the discrete flux, where the trajectories starting from the states with sufficiently large copy numbers and zero probability converge to a sink at $(+\infty, +\infty)$.

5.3.3.3   Fokker-Planck flux for the Toggle Switch Network

In the heat map of the Fokker-Planck probability flux, larger values are associated with higher probabilities (Figure 20G – Figure 20I). The states "Off-Off", "On-Off", and "Off-On" are attractors of the flux. The velocity and flux lines converges to the states "On-Off" and "Off-On", after first reaching the state "Off-Off". These are the same as the universal discrete

flux and the Liouville flux (Figure 20A and Figure 20D). Flux sinks are located at the states "On-Off" and "Off-On", represented by a single states $(X = 50, Y = 0)$ and $(X = 0, Y = 50)$ as in the case of Liouville flux. These two states correspond to the maxima of the Poisson distribution of the birth-and-death process (Equation 5.7) of reactions $R_1 - R_3$ given $x = 1$, and $R_2 - R_4$ given $y = 1$, respectively. The absolute value of velocity function $\log |\boldsymbol{v}_L(X, Y)|$ shows that the velocity has larger values at locations where the flux trajectories are close to be straight lines (purple regions on Figure 20F), but drops significantly when the trajectories make turns (turquoise regions on Figure 20I).

There are also significant differences between the Fokker-Planck flux and the discrete stochastic flux. The states "Off-On" and "On-Off" are single states with $(X = 50, Y = 0)$ and $(X = 0, Y = 50)$ in Fokker-Planck flux (Figure 20F)), but they involve sets of the states close to $(X = 50, Y = 0)$ and $(X = 0, Y = 50)$ in discrete flux (Figure 20C).The source of the flux for the Fokker-Planck flux is located at $(+\infty, +\infty)$ at the infinity. This is different from the universal discrete stochastic flux, where a sink is at $(+\infty, +\infty)$.

The Liouville flux trajectories and the Fokker-Planck trajectories depict similar behavior, but with some differences. Starting from the same initial locations, for instance, $(X = 70, Y = 40)$ or $(X = 40, Y = 70)$, the Liouville trajectories first tend to reach the state "Off-Off" and then converge to the states "On-Off" or "Off-On". In contrast, the Fokker-Planck flux starting from the same states tends to converge to the "Off-On" or the "On-Off" directly.

5.3.3.4   Flux in Different Genetic States

While previous discussions are based on projections in the (X, Y) plane with different genetic states of (x, y) marginalized, we now examined fluxes in each of the specific genetic states of genes x and y, namely, the "Off-Off" state at the gene copy number of $(x = 0, y = 0)$ (Figure 21A, Figure 21D, Figure 21G), the "On-Off" state at $(x = 1, y = 0)$ (Figure 21B, Figure 21E, Figure 21H), and the "On-On" state at $(x = 1, y = 1)$ (Figure 21C, Figure 21F, Figure 21I). We neglect the case of $(x = 0, y = 1)$ as it is symmetric to that of $(x = 1, y = 0)$.

At the "Off-Off" state $(x = 0, y = 0)$, we observe the existence of a sink at $(X = 0, Y = 0)$ for all three models of fluxes (Figure 21A, Figure 21D, and Figure 21G). This is expected, as it is the state where both genes are bound, and the probability distribution has a peak. The Fokker-Planck and the Liouville flux trajectories converge to the state $(X = 0, Y = 0)$ (Figure 21D) following straight lines evenly spread out in the $X - Y$ plane, whereas the discrete flux trajectories bend toward the axes of $X = 0$ and $Y = 0$.

At the "On-Off" state $(x = 1, y = 0)$, we observe the existence of the flux sink at $(X = 50, Y = 0)$ for the Liouville and Fokker-Planck models (Figure 21E and Figure 21H). The discrete stochastic flux trajectories converge to an area consisting states near $(X = 50, Y = 0)$.

At the"On-On" state, where both $X \in [40, 60]$ and $Y \in [40, 60]$, both genes are unbound and there is overall a small amount of probability mass associated with this genetic state. The three flux models give markedly different results, with sinks located at different locations. The discrete flux has the sink at $(+\infty, +\infty)$ (Figure 21C). The Liouville flux has the sink at $(X = 39, Y = 39)$ (Figure 21F). There are three sinks for the Fokker-Planck flux (Figure 21I).

It is informative to examine the behavior of the system with high copy number of P_X and P_Y in the regime where the law of mass action applies. We can obtain that critical points for each of the four genetic states. For the "On-On" state, we have $\langle X \rangle = (-d_X + \sqrt{d_X^2 + 4s_X b_y})/(2b_y d_X) \approx 37$, $\langle Y \rangle = (-d_Y + \sqrt{d_Y^2 + 4s_Y b_x})/(2b_x d_Y) \approx 37$. For the "On-Off" state, we have $\langle X \rangle = (s_X + u_y)/d_X \approx 50$, $\langle Y \rangle = 0$. For the "Off-On" state, we have $\langle X \rangle = 0$, $\langle Y \rangle = (s_Y + u_x)/d_Y \approx 50$. For the "Off-Off" state, we have $\langle X \rangle = (u_x)/d_X \approx 0$, $\langle Y \rangle = u_y/d_Y \approx 0$. The eigenvalues for all four critical points are negative, indicating that all four are sinks.

These critical points are exactly where the sinks of Liouville flux located. The sink $(X = 0, Y = 0)$ at the state "Off-Off" exists for all flux models. The sink at $(X = 50, Y = 0)/(X = 0, Y = 50)$ for the "On-Off"/"Off-On" state exists for the Liouville and Fokker-Planck models. In contrast the discrete flux lines converge to a broader set of states near the peak $(X = 50, Y = 0)$ $((X = 0, Y = 50))$. The Liouville flux converges to the sink at $(X \approx 37, Y \approx 37)$ for the "On-On" state, while there are mulitple sinks for Fokker-Planck flux. The discrete flux does not converge to a single sink.

5.3.4 Flux and Velocity Fields in the Toggle Switch with Weak Promoter Binding

We now consider the system with weak promoter binding. The binding rates are $b_x = b_y = 1 \times 10^{-4}$, the synthesis rates $s_x = s_y = 50$, the degradation rates $d_x = d_y = 1$, and unbinding rates $u_x = u_y = 0.1$. At the steady state, there are four probability peaks located at $(X, Y) = (0, 0)$, $(50, 0)$, $(0, 50)$, $(50, 50)$, corresponding to the states of genes G_x and G_y
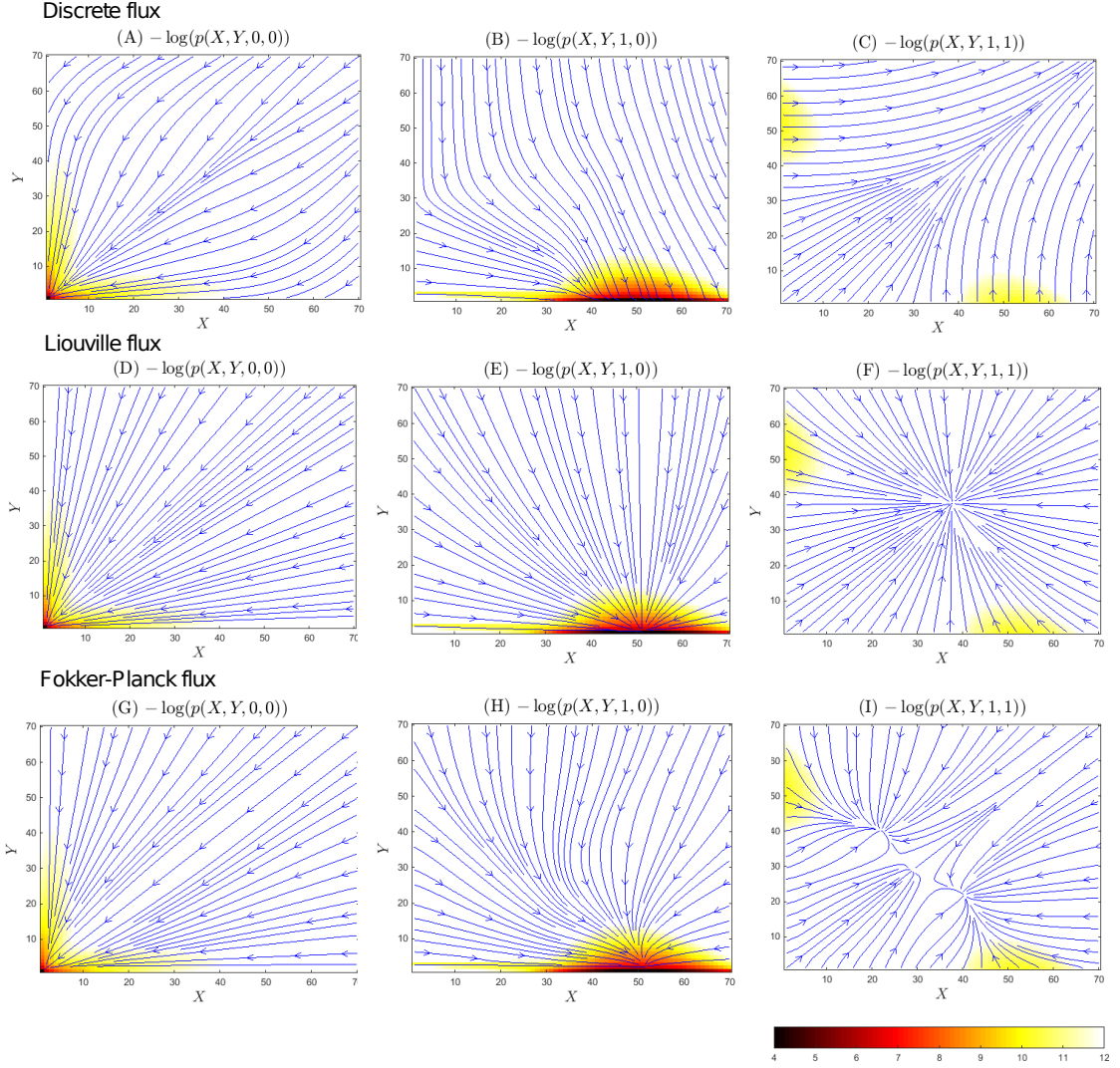
Figure 21. Fluxes of the toggle switch system described at strong promoter binding of $b = 1 \times 10^{-2}$. The "Off-Off"gene state ($x = 0$, $y = 0$): (A) heat map of $-\log p(X,Y,0,0)$ and flux lines of $\boldsymbol{J}_s(X,Y,0,0)$, (D) heat map of $-\log p(X,Y,0,0)$ and flux lines of $\boldsymbol{J}_L(X,Y,0,0)$, and (G) heat map of $-\log p(X,Y,0,0)$ and flux lines of $\boldsymbol{J}_{FP}(X,Y,0,0)$; The "On-Off"gene state ($x = 1$, $y = 0$): (B) heat map of $-\log p(X,Y,1,0)$ and flux lines of $\boldsymbol{J}_s(X,Y,1,0)$, (E) heat map of $-\log p(X,Y,1,0)$ and flux lines of $\boldsymbol{J}_L(X,Y,1,0)$, and (H) heat map of $-\log p(X,Y,1,0)$ and flux lines of $\boldsymbol{J}_{FP}(X,Y,1,0)$; The "On-On"gene state ($x = 1$, $y = 1$): (C) heat map of $-\log p(X,Y,1,1)$ and flux lines for $\boldsymbol{J}_s(X,Y,1,1)$, (F) heat map of $-\log p(X,Y,1,1)$ and flux lines for $\boldsymbol{J}_L(X,Y,1,1)$, (I) heat map of $-\log p(X,Y,1,1)$ and flux lines for $\boldsymbol{J}_{FP}(X,Y,1,1)$.

of "Off-Off" ($x = 0$, $y = 0$), "On-Off" ($x = 1$, $y = 0$), "Off-On" ($x = 0$, $y = 1$), and "On-On" ($x = 1$, $y = 1$) (Figure 22A, Figure 22D and Figure 22G). The steady state probability distribution for the birth-and-death process of reactions R_1, R_3 of (Equation 5.7, given $x = 1$, is the Poisson distribution with the maximum at its expected value of $X = s_X/d_X = 50$ [148]. Similarly, the steady state probability distribution for the birth-and-death process of reactions R_2, R_4, given $y = 1$, is the Poisson distribution with the maximum at its expected value of $Y = s_Y/d_Y = 50$. From computed $p(X, Y, x, y)$, we show $p(X, Y)$, $\boldsymbol{J}_s(X, Y)$, $\boldsymbol{J}_L(X, Y)$, $\boldsymbol{J}_{FP}(X, Y)$, $\boldsymbol{v}_s(X, Y)$, $\boldsymbol{v}_L(X, Y)$, and $\boldsymbol{v}_{FP}(X, Y)$ projected on the plane of (X, Y) in Figure 22.

The steady-state probability landscapes in $-\log p(\mathbf{x}, t)$ is shown in Figure 22A, Figure 22D and Figure 22G, where high probability regions in red, and regions where probability is close to zero in white. The trajectories of the flux field at the steady state are shown in blue for the universal discrete flux field $\mathbf{J}_s(\mathbf{x}, t)$ in Figure 22A– Figure 22C, for the Liouville flux field $\mathbf{J}_L(\mathbf{x}, t)$ in Figure 22D– Figure 22F, and for the Fokker-Planck flux field $\mathbf{J}_{FP}(\mathbf{x}, t)$ in Figure 22G– Figure 22I. In Figure 22B, Figure 22E and Figure 22H, regions with large absolute values of flux are shown in purple, and regions with low absolute values of flux are shown in turquoise blue. In Figure 22C, Figure 22F and Figure 22I, regions with large absolute values of velocity are shown in turquoise blue. In Figure 22B, Figure 22E and Figure 22I, regions with small absolute values of velocity are shown in purple.

5.3.4.1 Universal Discrete Stochastic Flux and Velocity fields

The heatmaps of the universal discrete probability flux in $\log |J_s(\mathbf{x}, t)|$ and velocity in $\log |v_s(\mathbf{x}, t)|$ are shown in Figure 22B and Figure 22C, respectively. We observe that loca-

tions with larger flux values also have higher probability. Unlike in the previous case of strong promoter binding, we observe the presence of stochastic oscillations around both "On-Off" and "Off-On" states. In addition to the oscillations between the states "Off-On" ("On-Off") and "On-On", the system also fluctuates from the state "On-On" to "Off-Off", and then to "Off-On"/"On-Off". Figure 22C of $\log |\boldsymbol{v}_s(X,Y)|$ shows that the velocity drops significantly when the trajectories make turns (turquoise regions, Figure 22C).

There are more states with large flux values compared to the condition of strong promoter binding, *i.e.*, there are more purple regions of higher probability mass in Figure 22B than in Figure 20B. With more distributed probability mass and the observation of oscillations, the steady state of the toggle switch system with weak promoter binding is overall markedly less stable than that with strong promoter binding.

5.3.4.2   Liouville Flux

In the heat map of Liouville flux, larger values are associated with higher probabilities (Figure 22D – Figure 22E). The states "Off-Off", "On-Off", "Off-On" and "On-On" are again the attractors of the flux. While stochastic discrete flux exhibits strong oscillations, Liouville flux trajectories converge to the probability peak at the "On-On" state after travelling through peaks at "On-Off", "Off-On", and "Off-Off" states. The source of the flux is at both infinity and at the state $(X = 35, Y = 35)$. The sink is located at the states $(X = 49, Y = 49)$. The absolute value of velocity function $\log |\boldsymbol{v}_L(X,Y)|$ are larger at locations where the flux trajectories are close to straight lines (purple regions, Figure 22F), but drop significantly when the trajectories make turns (turquoise regions on Figure 22F).
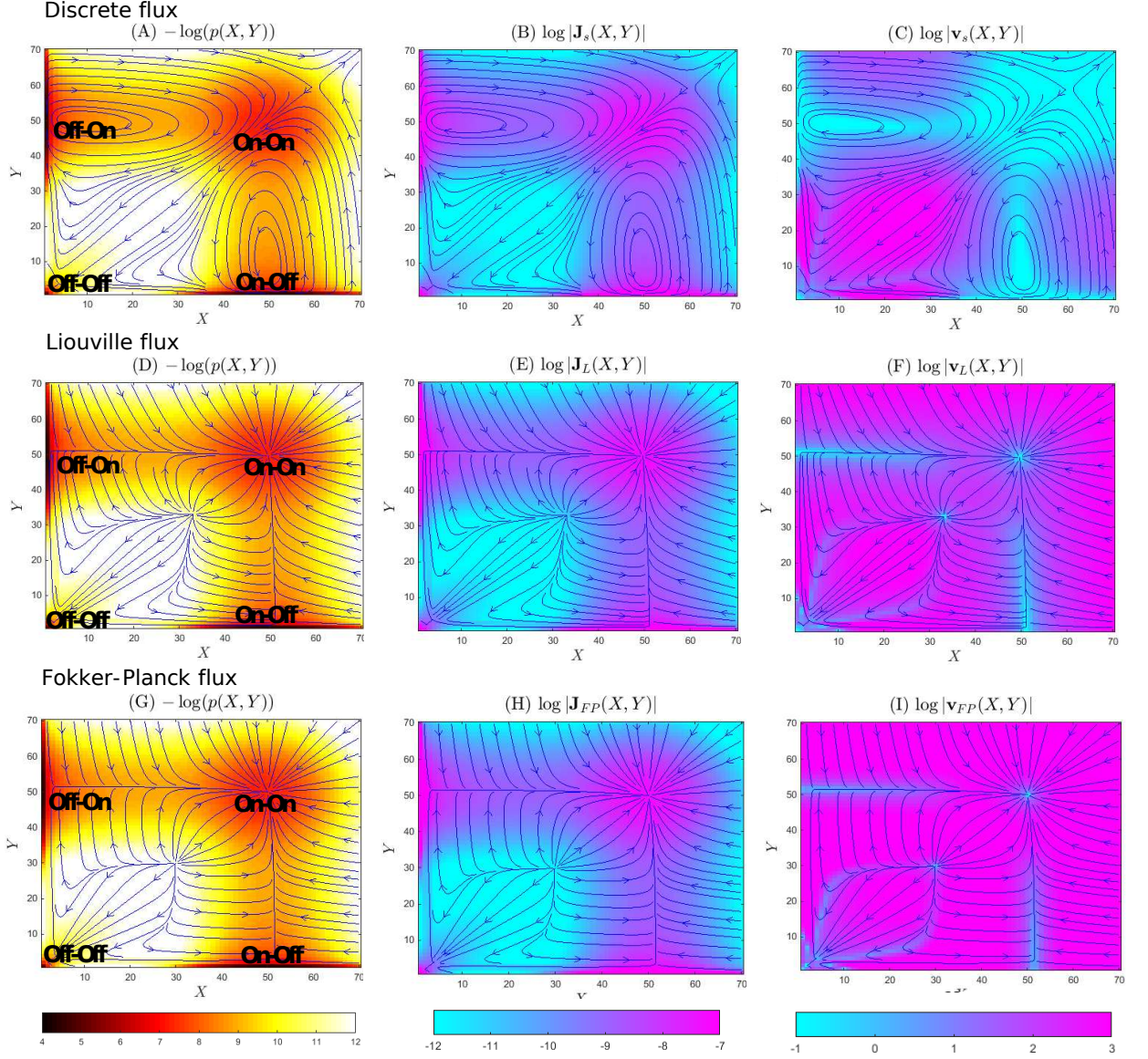
Figure 22. The probability landscapes, fluxes, and velocities of the toggle switch system with weak promoter binding ($b = 1 \times 10^{-4}$) at the steady state. Probability value is given by the color scale, and the fluxes/velocities are shown in blue solid lines. The discrete stochastic flux model with landscape in $-\log(p(x,y))$ (A), flux in $\log|\mathbf{J}_s(x,y)|$ (B), and velocity in $\log|\mathbf{v}_s(x,y)|$ (C); the Liouville flux model with landscape in $-\log(p(x,y))$ (D), flux in $\log|\mathbf{J}_L(x,y)|$ (E), and velocity in $\log|\mathbf{v}_L(x,y)|$ (F); and the Fokker-Planck flux model with landscape in $-\log(p(x,y))$ (G), flux in $\log|\mathbf{J}_{FP}(x,y)|$ (H), and velocity in $\log|\mathbf{v}_{FP}(x,y)|$ (I).

The Liouville flux trajectories and the universal discrete flux trajectories exhibit significantly different behavior. Due to fast unbinding relative to binding at this condition of prominent stochasticity, the toggle switch system constantly alternate between the bounded and unbounded states for genes x and y. However, this phenomena is not captured by the Liouville flux.

5.3.4.3 Fokker-Planck Flux for the Toggle Switch Network

In the heat map of the Fokker-Planck probability flux, larger values are associated with higher probabilities (Figure 22G– Figure 22I). The states "Off-Off", "On-Off", "Off-On" and "On-On" are the attractors of the flux. While stochastic discrete flux exhibits strong oscillations, Fokker-Planck flux trajectories, as Liouville flux, converge to the probability peak at the "On-On" state after travelling through peaks at "On-Off", "Off-On", and "Off-Off" states. The source of the flux is at both infinity and at the state $(X = 30, Y = 30)$. The sink is located at the states $(X = 50, Y = 50)$. The absolute value of velocity function $\log |\boldsymbol{v}_L(X, Y)|$ are larger at locations where the flux trajectories are close to straight lines (purple regions on Figure 22I), but drop significantly when the trajectories make turns (turquoise regions on Figure 22I).

The Liouville flux trajectories and the Fokker-Planck trajectories depict almost identical behavior of the system. There are some small differences. The sink for the gene state ($x = 1, y = 1$) for the Liouville flux is at $(X = 49, Y = 49)$, which is different for the sink for the Fokker-Planck flux, which is at $(X = 50, Y = 50)$ (Figure 22G – Figure 22I). There are significant differences between the Fokker-Planck flux and the discrete stochastic flux. Whereas

stochastic discrete flux exhibits oscillations, Fokker-Planck flux trajectories converge to the

system probability peak at the state "On-On" ($X = 50, Y = 50$)

5.3.4.4   Flux in Different Genetic States

We now examined the fluxes in each of the specific genetic states. At the "Off-Off" state

$(x = 0, y = 0)$ (Figure 23A, Figure 23D, Figure 23G), we observe the existence of the sink at

$(X = 0, Y = 0)$ for all three models of fluxes (Figure 23A, Figure 23D, Figure 23G). This is

expected, as it is the state where both genes are bound, and the probability peak is located at

$(X = 0, Y = 0)$. The Fokker-Planck and the Liouville flux trajectories converge to this state

$(X = 0, Y = 0)$ following straight lines, which are evenly spread off in the $X - Y$ plane, whereas

the discrete flux trajectories bend toward the axes of $X = 0$ and $Y = 0$.

At the "On-Off" state $(x = 1, y = 0)$ (Figure 23B, Figure 23E, Figure 23H), we observe the

existence of a flux sink at $(X = 50, Y = 0)$ for the Liouville and Fokker-Planck models (Fig-

ure 23D and Figure 23E). The discrete stochastic flux trajectories converge to an area of states

near $(X = 50, Y = 0)$.

At the "On-On" state where both genes are unbound (Figure 23C, Figure 23F, Figure 23I),

the three flux models give markedly different results, with sinks at different locations. The dis-

crete flux has a sink at $(+\infty, +\infty)$ (Figure 23C). The Liouville flux has the sink at $(X = 50, Y =

50)$ (Figure 23F), and the Fokker-Planck flux has the sink at $(X = 49, Y = 49)$ (Figure 23I).

It is interesting to examine the condition of high copy numbers of P_X and P_Y, where the law

of mass action applies. We can obtain the critical points for each of the four genetic states. For

the state "Off-Off", we have $\langle X \rangle = u_x/d_X \approx 0$, $\langle Y \rangle = u_y/d_Y \approx 0$. For the state "On-Off", we

have $\langle X \rangle = (s_X + u_y)/d_X \approx 50$, $\langle Y \rangle = 0$. For the state "Off-On", we have $\langle X \rangle = 0$, $\langle Y \rangle = (s_Y + u_x)/d_Y \approx 50$. For the state "On-On", we have $\langle X \rangle = (-d_X + \sqrt{d_X^2 + 4s_X b_y})/(2b_y d_X) \approx 50$, $\langle Y \rangle = (-d_Y + \sqrt{d_Y^2 + 4s_Y b_x})/(2b_x d_Y) \approx 50$. The eigenvalues at all four critical points are negative, indicating that they are sinks.

These critical points are where the sinks of Liouville and Fokker-Planck fluxes located. The sink $(X = 0, Y = 0)$ at the state "Off-Off" exists for all flux models. For the "On-Off"/"Off-On" state, the sink at $(X = 50, Y = 0)/((X = 0, Y = 0))$ exists for the Liouville and Fokker-Planck fluxes, while the discrete flux lines converge to a set of the states near $(X = 50, Y = 0)$ $((X = 0, Y = 50))$. For the "On-On" state, the Liouville and Fokker-Planck fluxes converge to $(X = 50, Y = 50)$ and $(X = 49, Y = 49)$, respectively. The discrete stochastic flux does not converge to any sink.

5.3.5   Stochastic Fluctuations and Oscillations in Toggle Switch

5.3.5.1   Strong Promoter Binding

With strong promoter binding ($b = 1 \times 10^{-2}$), the three flux models are overall similar, but with important differences in details. Discrete flux trajectories exhibit small fluctuations around the "On-Off" peak at $(X = 50, Y = 0)$ (and symmetrically at $(X = 0, Y = 50)$, Figure 24A). While changes in Y are just a handful copies of molecule, the amount of molecules of X fluctuates more significantly (Figure 24A).

To gain better understanding of the observed fluctuations, we examine reaction trajectories sampled using the SSA algorithm from the initial state of $(X = 50, Y = 0, x = 1, y = 0)$, where the "On-Off" peak is located. Figure 24B shows how trajectories of copy numbers of protein
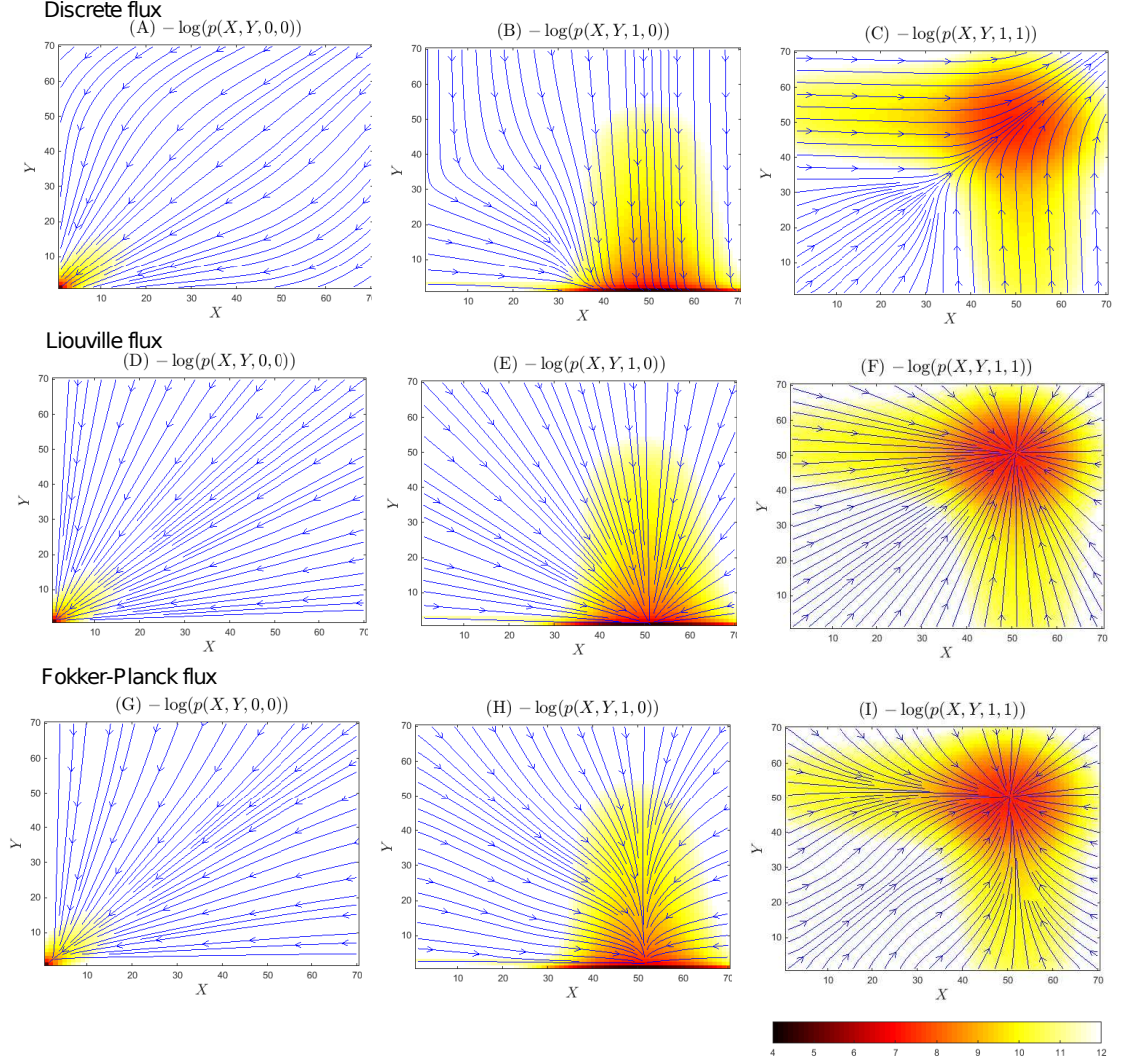
Figure 23. Fluxes of the toggle switch system described at weak promoter binding of $b = 1 \times 10^{-4}$. The "Off-Off" gene state ($x = 0$, $y = 0$): (A) heat map of $-\log p(X, Y, 0, 0)$ and flux lines of $\boldsymbol{J}_s(X, Y, 0, 0)$, (D) heat map of $-\log p(X, Y, 0, 0)$ and flux lines of $\boldsymbol{J}_L(X, Y, 0, 0)$, and (G) heat map of $-\log p(X, Y, 0, 0)$ and flux lines of $\boldsymbol{J}_{FP}(X, Y, 0, 0)$; The "On-Off" gene state ($x = 1$, $y = 0$): (B) heat map of $-\log p(X, Y, 1, 0)$ and flux lines of $\boldsymbol{J}_s(X, Y, 1, 0)$, (E) heat map of $-\log p(X, Y, 1, 0)$ and flux lines of $\boldsymbol{J}_L(X, Y, 1, 0)$, and (H) heat map of $-\log p(X, Y, 1, 0)$ and flux lines of $\boldsymbol{J}_{FP}(X, Y, 1, 0)$; The "On-On" gene state ($x = 1$, $y = 1$): (C) heat map of $-\log p(X, Y, 1, 1)$ and flux lines for $\boldsymbol{J}_s(X, Y, 1, 1)$, (F) heat map of $-\log p(X, Y, 1, 1)$ and flux lines for $\boldsymbol{J}_L(X, Y, 1, 1)$, (I) heat map of $-\log p(X, Y, 1, 1)$ and flux lines for $\boldsymbol{J}_{FP}(X, Y, 1, 1)$.
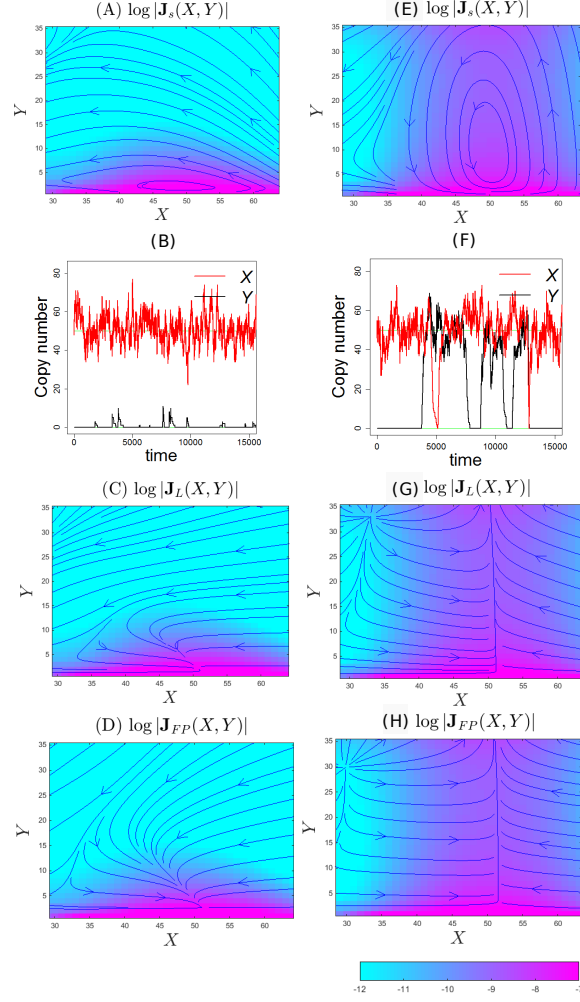
Figure 24. The flow maps and trajectories of the probability fluxes of the toggle switch system near the state "On-Off", with strong promoter binding ($b = 1 \times 10^{-2}$) shown in $\log|\mathbf{J}_s(x,y)|$ (A), $\log|\mathbf{J}_L(x,y)|$ (C), $\log|\mathbf{J}_{FP}(x,y)|$ (D); and with weak promoter binding ($b = 1 \times 10^{-4}$) shown in $\log|\mathbf{J}_s(x,y)|$ (E), $\log|\mathbf{J}_L(x,y)|$ (G), $\log|\mathbf{J}_{FP}(x,y)|$ (H). Sampled Gillespie trajectories starting from the state ($X = 50$, $Y = 0$, $x = 1$, $y = 0$) are shown for strong binding (B) and for weak binding (F).

P_X (red lines) and protein P_Y (black lines) fluctuate. P_X fluctuates around $X = 50$. This is due to stochasticity in the synthesis and the degradation of P_X at the genetic state of $x = 1$. The trajectories of copy number of protein P_Y (black lines) also fluctuate around $Y = 0$, but with overall much smaller magnitude. This is because gene G_y occasionally becomes unbound ($X > 0$), upon which P_Y is synthesized. However, since promoter binding is strong and at this condition P_X is in much larger amount then P_Y, gene G_y rapidly becomes inhibited by P_X again.

The fluctuations observed in reaction trajectories are well explained by the flux lines shown in Figure 24A, which form closed, x-axis-oriented horizontal ellipses around the state ($X = 50, Y = 0$) (Figure 24A). The major axis of the ellipse corresponds to the stochastic fluctuations with larger magnitude in copies of P_X, and the minor axis to fluctuation with smaller magnitude in copies of P_Y.

While the behavior of stochastic fluctuation observed in reaction trajectories are well captured in the flowmap computed discrete stochastic flux, these fluctuations, however, are not captured by either the Liouville flux (Figure 24C) or the Fokker-Planck flux (Figure 24D), where both converge to a single state ($X = 50, Y = 0$) (and symmetrically to ($X = 0, Y = 50$)).

5.3.5.2 <u>Weak Promoter Binding</u>

With weak promoter binding ($b = 1 \times 10^{-4}$), there are significant differences between the discrete flux and fluxes based on continuum approximations. The discrete flux lines (Figure 22A) exhibit strong oscillations between ($X = 50, Y = 50$) and ($X = 50, Y = 0$), and symmetrically between ($X = 50, Y = 50$) and ($X = 0, Y = 50$). Furthermore, probability flux also flows from

($X = 50$, $Y = 50$) to ($X = 0$, $Y = 0$), then to ($X = 50$, $Y = 0$), and back to ($X = 50$, $Y = 50$). Symmetric oscillatory pattern is also seen, where flux lines flow back to ($X = 50$, $Y = 50$) via ($X = 0$, $Y = 0$) and ($X = 0$, $Y = 50$). In addition, occasionally oscillation can be seen between ($X = 50$, $Y = 0$) and ($X = 0$, $Y = 50$) via the state of ($X = 50$, $Y = 50$).

To gain better understanding of the stochastic oscillations uncovered from the discrete flux model, we examine reaction trajectories sampled from the initial state of ($X = 50, Y = 0, x = 1, y = 0$), where the "On-Off" peak is located. Figure 24F shows trajectories of copy number of protein P_X (red lines) and protein P_Y (black line). P_X fluctuates with small magnitude around $X = 50$. This is due to stochasticity in P_X synthesis and degradation at $x = 1$. This is similar to the fluctuation in P_X shown in Figure 24B where promoter binding is fast. P_Y exhibit similar fluctuation around $Y = 50$.

However, there is significant oscillation in P_Y (black line) of larger magnitude between $Y = 50$ and $Y = 0$. This is due to stochastic switching between the gene state of $y = 1$ and $y = 0$. Similarly, P_X (red) also oscillates between $X = 50$ and $X = 0$ due to switching between $x = 1$ and $x = 0$. Unlike that of strong promoter binding (Figure 24B), trajectory of P_Y (blackline) exhibit no fluctuations around $Y = 0$ (Figure 24F). This is because when gene G_y becomes unbound ($y = 1$), the system has sufficient time to transit from ($Y = 0$) to ($Y = 50$) before gene G_y becomes bound again ($y = 0$), as promoter binding of P_X to G_y is slow. Furthermore, the durations of simultaneous high copies of P_X and P_Y ($X = 50$, $Y = 50$) are relatively short.

The oscillations observed in reaction trajectories are well-explained by the flowmap of the discrete flux (Figure 24E and Figure 22A). The closed vertical ellipses with foci at states $(X = 50, Y = 0)$ and $(X = 50, Y = 50)$ correspond to the larger stochastic fluctuations in Y (blackline) and smaller magnitute fluctuations in X (redline) (Figure 24F). Shown in Figure 22A but not in Figure 24E for clarity, the closed horizontal ellipses with foci at states $(X = 0, Y = 50)$ and $(X = 50, Y = 50)$ correspond to the larger stochastic fluctuations in X (redline) and smaller magnitute fluctuations in Y (blackline). Furthermore, corresponding to the shorter durations in trajectories when both P_X and P_Y are high at 50 (Figure 24F), the state $(X = 50, Y = 50)$ indeed is a transient state in the flow maps of the discrete flux (Figure 22A– Figure 22C).

Overall, the behavior of stochastic oscillations and fluctuations observed in reaction trajectories are well captured in the computed discrete stochastic flux. These oscillating behaviors, however, are not captured by either the Liouville flux (Figure 24C) or the Fokker-Planck flux (Figure 24D), where in either case the system converges to a single state of $(X = 50, Y = 50)$.

5.4   Oscillations in Feedback Network Motifs

The results obtained in the previous section showed the oscillations in toggle-switch network motif with weak promoter binding which were not reported before. Oscillations are known to happen in repressiator [149–151], which has three nodes, delayed positive feedback [152, 153], and negative feedback with positive and negative regulations [154, 155].

We further show the discrete flux for negative and positive feedback networks with the binding and unbinding regimes described before, and compare the nature of flux in these two systems with the flux in toggle switch network.

First, we consider a negative feedback network consisting of two genes, G_x and G_y, expressing proteins P_X and P_Y, correspondingly. The dimer of protein X inhibits G_y, and the dimer of protein Y activates G_x (Figure 25A). G_x is expressed with basal expression rate $s_X = 5$, but it is expression rate is increased to $s_X = 50$ when activated. G_y is expressed with a basal expression rate $s_Y = 50$, and it is not expressed when inhibited by P_X dimer. Both proteins P_X and P_Y degrade with the rate of $d_Y = 1$.

5.4.1 Weak Promoter Binding

When the binding rates of both G_x and G_y rate of $b = b_x = b_y = 0.0001$, and unbinding rate is $u = u_x = u_y = 0.1$ for both genes, the system has slow promoter dynamics. These binding and unbinding rates are identical to the rates of toggle-switch system with weak promoter binding we examined earlier. Due to such large differences in the rates b and u, the behavior of toggle switch system is highly stochastic. We obtained the steady state probability landscape of this system by solving discrete Chemical Master Equation with ACME method (Figure 25B) [69, 84]. This probability landscape has four peaks, corresponding to the specific G_x and G_y states. We have (0, 0): G_x is activated and G_y is inhibited, (1, 0): G_x is unbound, G_y is inhibited. We further study how the transitions between these important phenotypic states occur in the steady state. Hence, we compute probability flux for this discrete highly stochastic system.
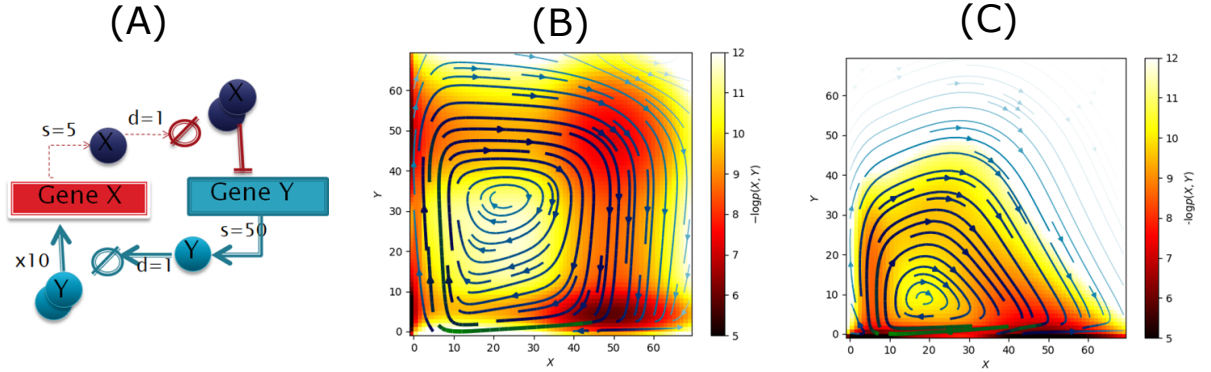
Figure 25. Feedback genetic network: schematic representation (A), the heatmap $-\log p(X, Y)$ and flux trajectories of probability (B) the system with weak promoter binding of $b = 1 \times 10^{-4}$, (C) the system with weak promoter binding of $b = 1 \times 10^{-2}$.

We can see oscillating trajectories between the states (1, 1)-(0, 1)-(0, 0)-(1, 0) (Figure 25B). When the system is at the state (1, 1) where both genes are unbound, the copy number of P_Y is high, and its dimer activates G_x and the system transits to the state (0, 1), where both proteins have high copy numbers. At the state (0, 1), once the dimer of X binds to G_y, its inhibition occurs, the systems transits from the state (0, 1) to the state (0, 0). At (0, 0) the copy number of Y is low, and G_x gets unbound and deactivated, therefore, transits to the state (1, 0). At the state (1, 0) both protein X and Y copy numbers are low, and the inhibited G_x becomes unbound, the system transits to the state (1, 1). Hence, the cycle happens again.

5.4.2   Strong Promoter Binding

When the binding of both G_x and G_y rate of $b = b_x = b_y = 0.01$ and unbinding rate is $u = u_x = u_y = 0.1$ for both genes, the system has strong promoter dynamics. These binding and unbinding rates are identical to the rates of toggle-switch system with strong promoter binding studied before. We obtained the steady state probability landscape of this system by solving discrete Chemical Master Equation with ACME method (Figure 25C) [69, 84]. This probability landscape has only two peaks, corresponding to the specific G_x and G_y states, (1,1) and (0,1) correspondigly. We have (1, 1) state: both G_x and G_y are unbound; (0, 1): G_x is activated, G_y is unbound; (0, 0): G_x is activated and G_y is inhibited, (1, 0): G_x is unbound, G_y is inhibited. We further study how the transitions between these important phenotypic states occur in the steady state. Hence, we compute probability flux for this discrete highly stochastic system.

We can observe oscillating trajectories between the states (1, 0) and (1, 0) Figure 25C. At the state (1, 0) both protein X and Y copy numbers are low. However due to large binding rate, G_x becomes bound and system transitions into the state (0, 0). Due to strong inhibition G_y is inhibited, and at (0, 0) the copy number of P_Y is low, and G_x becomes unbound, and therefore not activated. Thus the system transitions to the state (1, 0) occurs. The cycle happens again.

With the example of such a simple genetic feedback system, we showed how complex behavior of the oscillation in highly stochastic system can be easily understood with the discrete probability flux model. These results are consistent with the known phenomena of oscillations in negative feedback loop [154]. Unlike in the toggle switch, oscillations happen in both

cases of strong and weak promoter binding. Moreover, the oscillation trajectories sequentially connect all the important phenotypic states, whereas in the toggle-switch oscillations multiple trajectories connect subsets of the important phenotypic states.

5.5   Probability Flux and Velocity to the Study of Problem of Gene Duplication

Probability velocity and flux fields can be used for studying of a wide range of important biological problems. Here we apply them to the problem of gene duplication in toggle switch networks, where the processes of transcription and translations are explicitly modeled.

The process of gene duplication is widely studied. In [156] it is suggested that after gene duplication the amount of expression of each of daughter genes is reduced, relative to the expression of progenitor gene. It prohibits the loss of either of daughters genes, and daughter copies retain all the ancestral functions.

Here we study how different outcomes of gene duplication affect the behavior of the toggle switch network. Particularly, we study gene duplication in the toggle switch network with and without expression reduction. We consider three cases of gene expression reduction with different levels of expression of daughter genes.

5.5.1   Two-level Toggle Switch Model

We employ a detailed model of two level toggle switch, where the binding and unbinding reactions are explicitly modeled and the synthesis is modeled as two step process involving translation and transcription.

There are eight molecular species in our model: genes G_x and G_y, which express proteins P_X and P_Y, messenger RNAs, $mRNA_X$, and $mRNA_Y$, as well as protein-DNA complexes $\overline{G}_x$ and $\overline{G}_y$ with protein P_Y bound to gene G_x and protein P_X bound to gene G_y, respectively (Figure 26). The dimer of the product P_X inhibits the activity of gene G_y, as well as the dimer of protein P_Y inhibits the activity of gene G_x.
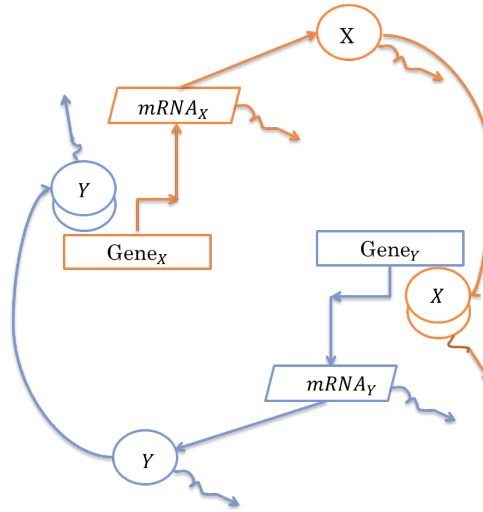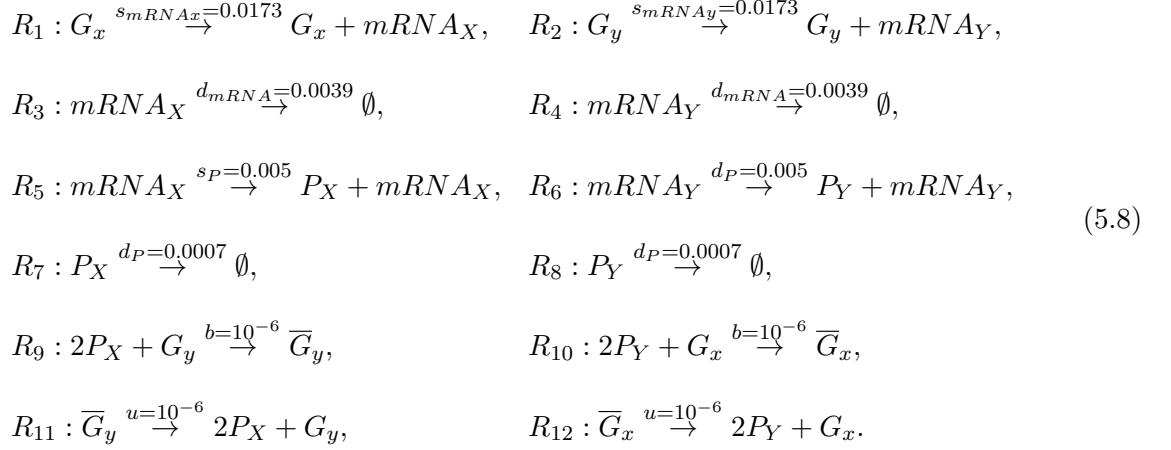

Figure 26.   Schematic representation of the two level toggle switch genetic network.

The molecular reactions and corresponding reaction rates of the network are listed below:

$$
\begin{aligned}
&R_1 : G_x \overset{s_{mRNAx}=0.0173}{\rightarrow} G_x + mRNA_X, \quad &&R_2 : G_y \overset{s_{mRNAy}=0.0173}{\rightarrow} G_y + mRNA_Y,\\
&R_3 : mRNA_X \overset{d_{mRNA}=0.0039}{\rightarrow} \emptyset, \quad &&R_4 : mRNA_Y \overset{d_{mRNA}=0.0039}{\rightarrow} \emptyset,\\
&R_5 : mRNA_X \overset{s_P=0.005}{\rightarrow} P_X + mRNA_X, \quad &&R_6 : mRNA_Y \overset{d_P=0.005}{\rightarrow} P_Y + mRNA_Y,\\
&R_7 : P_X \overset{d_P=0.0007}{\rightarrow} \emptyset, \quad &&R_8 : P_Y \overset{d_P=0.0007}{\rightarrow} \emptyset,\\
&R_9 : 2P_X + G_y \overset{b=10^{-6}}{\rightarrow} \overline{G}_y, \quad &&R_{10} : 2P_Y + G_x \overset{b=10^{-6}}{\rightarrow} \overline{G}_x,\\
&R_{11} : \overline{G}_y \overset{u=10^{-6}}{\rightarrow} 2P_X + G_y, \quad &&R_{12} : \overline{G}_x \overset{u=10^{-6}}{\rightarrow} 2P_Y + G_x.
\end{aligned}
\tag{5.8}
$$

The microstate of the system is defined as an ordered sextuplet (X, Y, mX, mY, x, y) of copy numbers of species P_X, P_Y, $mRNA_X$, $mRNA_Y$, G_x, and G_y, respectively. The copy numbers of bound genes $\overline{G}_x$ and $\overline{G}_y$ are denoted as $\overline{x}$ and $\overline{y}$. Correspondingly, $x = n_x - \overline{x}$ and $y = n_y - \overline{y}$, where n_x and n_y denote the total number of copies of genes G_x and G_y in this system. There are a number of stochastic processes encoded in this network. The transcriptions of $mRNA_X$ and $mRNA_Y$ from gene G_x and gene G_y are represented by reactions R_1 and R_2, respectively. The translations of proteins P_X and P_Y from gene mRNAs $mRNA_X$ and gene $mRNA_y$ are represented by reactions R_5 and R_6, respectively. The degradations of $mRNA_X$, $mRNA_y$, P_X, and P_Y are represented by reactions R_3, R_4, R_7, and R_8, respectively. Reaction R_9 represents the binding of two copies of protein P_X to the promoter site of G_y to form a protein-DNA complex $\overline{G}_y$. Reaction R_{10} represents the unbinding of the complex $\overline{G}_y$. Similarly, reaction

R_{11} represents the binding of two copies of protein P_Y to the promoter site of G_x to form a protein-DNA complex $\overline{G}_x$. Reaction R_{12} represents the unbinding of the complex $\overline{G}_x$.

Probability landscape and corresponding flux trajectories for the case of $n_x = 1$ and $n_y = 1$. The probability projected to the species P_X, P_Y (Figure 27A) shows that the system has four peaks: at $(X = 30, Y = 30)$, corresponding to the state $(x = 1, y = 1)$, when both of the genes are expressed, at $(X = 30, Y = 0)$, corresponding to the state $(x = 1, y = 0)$, when the gene G_x is expressed and G_y is inhibited, at $(X = 0, Y = 30)$, corresponding to the state $(x = 0, y = 1)$, when the gene G_x is inhibited and G_y is expressed, and at $(X = 0, Y = 0)$, corresponding to the state, corresponding to the state $(x = 0, y = 0)$, when both of the genes are inhibited. The flux lines show the oscillations around the states with $(X = 30, Y = 0)$ and $(X = 0, Y = 30)$, where the oscillation trajectories are going through the state $(X = 0, Y = 0)$. There are also small fluctuation around the state $(X = 30, Y = 30)$, with the source of the probability flux at $(+\infty, +\infty)$.

5.5.2 Case of Gene Duplication with no Expression Reduction

We consider the case, when G_y is duplicated $(n_y = 2)$ and transcription rates of daughter genes are the same as the transcription rate of the ancestral gene s_{mRNAy}. The system has five peaks of protein copy numbers at $(X = 0, Y = 0)$, $(X = 0, Y = 30)$, $(X = 0, Y = 60)$, $(X = 30, Y = 0)$, $(X = 30, Y = 30)$ (Figure 27B). The peak at $(X = 30, Y = 30)$ is of very small size. Probability flux oscillatory trajectories connect the state $(X = 30, Y = 30)$ with two peaks $(X = 0, Y = 30)$, $(X = 0, Y = 0)$. There are also oscillations between the states of $(X = 0, Y = 30)$, $(X = 0, Y = 60)$. In contrast to the case of $n_x = n_y = 1$ (Figure 27A),

state $(X = 30, Y = 30)$ is a transient state for probability mass trajectories, and there is no probability flux from the peak $(X = 30, Y = 30)$ in the direction of increase of copy numbers of X and Y.
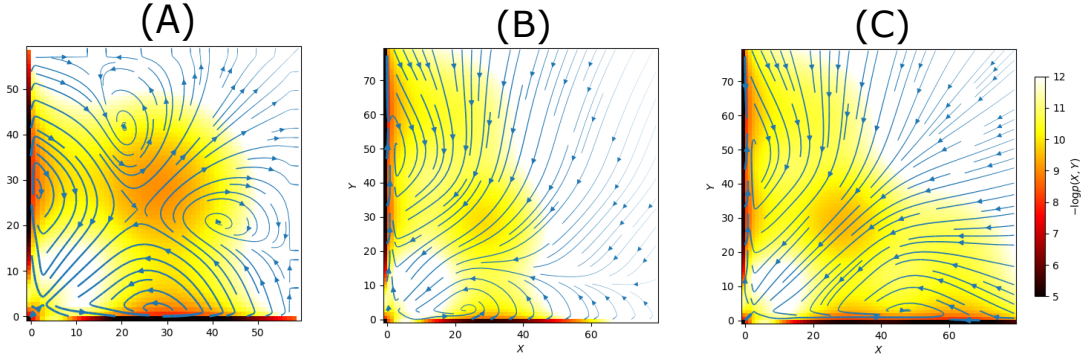

Figure 27.   The steady-state probability landscape $-\log(p(X, Y))$ and flux trajectories for the system in (Equation 5.8): (A) one copy of both genes $(n_x = 1, n_y = 1)$, (B) two copies of gene G_y $(n_x = 1, n_y = 2)$, (C) two copied of both genes $(n_x = 2, n_y = 2)$.
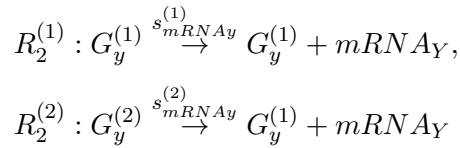
We then consider the case, when both G_x and G_y are duplicated, so that $(n_x = 2, n_y = 2)$. The transcription rates of both daughter genes are the same as the transcription rate of the ancestral gene s_{mRNAx} and s_{mRNAy}, correspondingly. The system has six peaks of protein copy numbers at $(X = 0, Y = 0)$, $(X = 0, Y = 30)$, $(X = 0, Y = 60)$, $(X = 30, Y = 0)$, $(X = 60, Y = 0)$, $(X = 30, Y = 30)$ (Figure 27C). The peak at $(X = 30, Y = 30)$ is larger,

comparing to the case of single copy of each gene (Figure 27B), but it is still a transient state for the flux. The oscillations trajectories between the states of $(X = 0, Y = 30)$ and $(X = 0, Y = 60)$ and between the states of $(X = 30, Y = 0)$ and $(X = 60, Y = 0)$ are going through the peak at $(X = 30, Y = 30)$.

The behavior of the system with $(n_x = 1, n_y = 1)$ is very different comparing to the behavior of the toggle switch system with $(n_x = 1, n_y = 2)$ or $(n_x = 2, n_y = 2)$. In both cases of gene duplication, the peak at $(X = 30, Y = 30)$ is a transient peak for a probability flux, and there is no oscillations at this peak, unlike in the system with one copy of each gene (Figure 27B). It possibly suggests that the behavior of the system with one copy of each gene is the most noisy.

5.5.3   Case of Expression Reduction of Daughters Genes

We further consider the case when the gene G_y was duplicated and two daughter genes $G_y^{(1)}$ and $G_y^{(2)}$ were created in result of such duplication. We further model the system, where the transcription rates of two daughter genes are different, and the their total rate is equal to the initial rate of expression of gene G_y, which is s_{mRNAy}. In this case, the process can be described by the system of the reactions (Equation 5.8) with R_2 being substituted with two reactions $R_2^{(1)}$ and $R_2^{(2)}$:

$$R_2^{(1)} : G_y^{(1)} \overset{s_{mRNAy}^{(1)}}{\rightarrow} G_y^{(1)} + mRNA_Y,$$

$$R_2^{(2)} : G_y^{(2)} \overset{s_{mRNAy}^{(2)}}{\rightarrow} G_y^{(1)} + mRNA_Y$$

We first find probability landscape and flux for the case, when $s_{mRNAy}^{(1)}/s_{mRNAy}^{(2)} = 2.25$, meaning that transcription rates of one daughter genes is 2.25 times larger than the other daughter gene. Probability landscape (Figure 28A) shows three peaks, at $(X = 0, Y = 0)$,
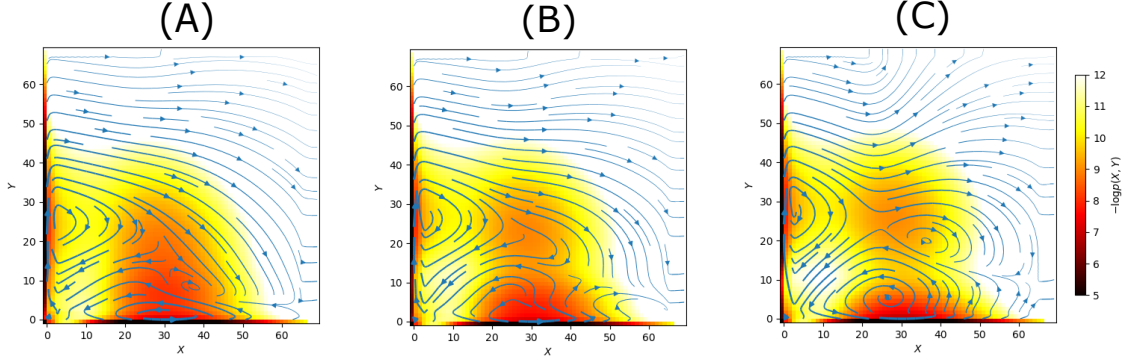
Figure 28. The steady-state probability landscape $-\log(p(X,Y))$ and flux trajectories for the toggle switch system with asymmetric transcription rates of two daughters genes after duplication (A) $s^{(1)}_{mRNAy}/s^{(2)}_{mRNAy} = 2.25$, (B) $s^{(1)}_{mRNAy}/s^{(2)}_{mRNAy} = 4.0$, (C) $s^{(1)}_{mRNAy}/s^{(2)}_{mRNAy} = 9.0$.

$(X=30, Y=0)$, and $(X=0, Y=30)$. The peak at $(X=30, Y=30)$ (Figure 27A), merges with the peak at $(X=30, Y=0)$. The behavior of the system in this case is significantly different to the behavior of the system with one copy of each gene (Figure 27A). Similarly to the case of one copy of each gene (Figure 27A), there are oscillatory trajectories around $(X=30, Y=0)$ and $(X=0, Y=0)$, as well as $(X=0, Y=30)$ and $(X=0, Y=0)$. Unlike in the in the case of one copy of each gene (Figure 27A), the oscillating trajectories on (Figure 28A) are asymmetric. Moreover there is a sink at the state $(+\infty, +\infty)$, however the trajectories approaching this state are asymmetric, and only indicate the increase of X.

We find probability landscape and flux for the case, when $s^{(1)}_{mRNAy}/s^{(2)}_{mRNAy} = 4.0$, meaning that transcription rates of one daughter genes is four times larger than the other daughter gene. Probability landscape (Figure 28B) shows four peaks, at $(X = 0, Y = 0)$, $(X = 30, Y = 0)$, $(X = 0, Y = 30)$, and $(X = 30, Y = 30)$. The peak at $(X = 30, Y = 30)$ (Figure 28B) exists, but it is very close to the peak at $(X = 30, Y = 0)$. The behavior of the system in this case is different to the behavior of the system with one copy of each gene (Figure 27A). Similarly to the case of one copy of each gene (Figure 27A), there are oscillatory trajectories around $(X = 30, Y = 0)$ and $(X = 0, Y = 0)$, as well as $(X = 0, Y = 30)$ and $(X = 0, Y = 0)$, moreover these oscillating trajectories on (Figure 28B) are quite symmetric. In addition, there is a sink at the state $(+\infty, +\infty)$, however the trajectories approaching this state are asymmetric, and only indicate the increase of X. Unlike on Figure 27A the he peak at $(X = 30, Y = 30)$ is a transient peak for the probability flux.

We next find probability landscape and flux for the case, when $s^{(1)}_{mRNAy}/s^{(2)}_{mRNAy} = 9.0$, meaning that transcription rates of one daughter genes is nine times larger than of the other daughter gene. Probability landscape (Figure 28C) shows four peaks, at $(X = 0, Y = 0)$, $(X = 30, Y = 0)$, $(X = 0, Y = 30)$, and $(X = 30, Y = 30)$. The peak at $(X = 30, Y = 30)$ (Figure 28C) is emerging in this case. The behavior of the system in this case is even more similar to the behavior of the system with one copy of each gene (Figure 27A). Similarly to the case of one copy of each gene (Figure 27A), there are oscillatory trajectories around $(X = 30, Y = 0)$ and $(X = 0, Y = 0)$, as well as $(X = 0, Y = 30)$ and $(X = 0, Y = 0)$, moreover, like in the case of one copy of each gene (Figure 27A), the oscillating trajectories

on (Figure 28C) show more symmetry comparing to the cases on Figure 27A-B. Moreover there is a sink at the state $(+\infty, +\infty)$, and there are trajectories reaching to this state from both directions of increase X and Y. The flux around the peak fluctuates.

The system with the closest behavior to the original system is the system with asymmetric transcription rates with the largest difference between these rates. It is natural, because the large difference of the reaction rates of both genes indicates that the effect of one gene is much more significant, therefore the behavior of this system is close to the behavior of the system with one copy of each gene. In contrast, the system with the smallest differences in transcription rates of daughter genes is less similar to the system with one copy of each gene: the peak at $(X = 30, Y = 30)$ is merged with the peak at $(X = 30, Y = 0)$, and there is no significant oscillations around this peak, which may indicate that this system overall is less noisy.

5.6   Conclusions

In this study, we constructed global flow maps of probability flux over the state space in all possible directions simultaneously for three types of flux models, namely, 1) the Discrete Universal Stochactic flux; 2) the Liouville flux; 3) and the Fokker-Planck flux. While flux in stochastic models has been commonly based on Fokker-Planck formulations, we introduced here the models based on mass-action kinetics and studied with relation to Fokker-Planck and universal discrete flux. While Fokker-Planck model and universal discrete flux model behaved similarly in several well-studied examples, including Schnakenberg system [37, 38], this study reveals the difference between these two models in highly stochastic system of toggle switch with slow promoter binding. We first showed theoretical differences between these three types

of fluxes. We showed that the differences between the models are due to the differences of the second order terms or so called diffusion terms of the Kramers-Moyal expension. Moreover, when the reactions are defined with directions, the flux for forward reactions may overlap, but the reverse reactions fluxes are always different for the universal discrete flux.

We further studied details of the probability fluxes using the network model of the toggle switch system. We examine the behavior of these fluxes, under two conditions, namely, i) when the binding rates of the genes by transcription factors are much further than the unbinding rates, with which the system exhibiting three stable states, and ii) when the unbinding rates are of the same magnitude as binding rates, with which the system exhibiting strong stochastic fluctuations and four stable states at the steady state. Our results show that fluxes computed with these three differenting models exhibit significantly different results. We show that the universal discrete stochastic flux exhibits strong oscillating behavior at the non-equilibrium steady state, which is due to strong fluctuations between binding and unbinding events. In contrast, Fokker-Planck and Liouville models fail to capture this phenomenon. Simulated stochastic trajectories fully confirmed findings obtained using the universal discrete models.

In addition, we applied the developed flux method to studies of the oscillations in negative feedback and the problem of gene duplication. We confirmed the occurrence of oscillations in negative feedback, and showed oscillatory trajectories for the system with two and four peaks. We built two level toggle-switch model, where the reactions of transcription and translation are modeled explicitly. We showed that the behavior of the system after duplication is closest to the

behavior of the system with one copy of both genes, when the expression rates are asymmetric and the difference in their values is largest.

CHAPTER 6

SUMMARY AND FUTURE WORK

In this work we developed methods that facilitate accurate computation of probability, as well as finding the velocity and flux of probability in stochastic gene regulatory networks, that were previously infeasible. We applied these methods to study different examples, motivated by real world biological problems of significant importance.

Solving the discrete Chemical Master Equation (dCME) is of fundamental importance for studying stochasticity in reaction networks. The main challenges are the discrete nature of the states and the difficulty in enumerating these states, as the size of the state space expands rapidly when the network becomes more complex. The method developed in this work allows exact computation of probability landscape within the predefined error bound, and assessment of the error *a priori* and after the computations. Such accurate modeling is important for studying the rare events, such as the spontaneous switch from lysogeny of phage lambda into lysis, or the cancerogenesis of a normal cell. The theorems proved here could be used for developing new truncation methods, involving reflecting boundaries, when the probability mass is conserved within the system, and there is no state absorbing the probability mass involved. Here we developed the upper bound truncation for the elementary species participating in the synthesis and degradation from the buffer. The further development of the theory for the lower bound truncation of the elementary species copy number is in the progress. It will allow us to eliminate the states with the small copy number of molecules, which have low

probability. Further, we plan to introduce upper and lower bound for copy number of every specie, participating in synthesis and degradation. Such truncation can possibly allow to have more efficient truncation and larger savings of the state space.

We also studied feed-forward loop network motifs as one of the most ubiquitous three node network motifs, which has high significance in mammalian cells. The results of our computational experiments suggest that feed-forward loop can exhibit multitude of cellular phenotypes due to stochastic fluctuations in between distinct expression levels given slow promoter binding. The regulation intensities of feed-forward loop are the key determinants, which can be fine-tuned in order to achieve specific phenotypic behavior. We further studied the sensitivity of these regulation intensities. Results obtained suggest that the steady state probability landscape of feed-forward loop with less peaks is more robust to the changes of its parameters. Overall, these findings can be useful in biological studies, in which synthetic feed-forward loops are constructed, and can help to overcome the challenge of selecting experimental parameters of the system according to particular programmed behavior.

We introduced new formulations of discrete flux and discrete velocity for a general mesoscopic reaction system. Specifically, we redefined the derivative and divergence operators based on the discrete nature of chemical reactions. We then introduced the discrete form of continuity equation for the systems of reactions. We defined two types of discrete flux: i) the reactional flux, and ii) the species flux, with their relationship specified. The reactional discrete flux satisfies the continuity equation and describes the behavior of the system evolving along directions of reactions. The species flux directly describes the dynamic behavior of the reactions such

as the transfer of probability mass in the state space. Our discrete flux model enables the construction of the global time-evolving and steady-state flow-maps of fluxes in all directions at every microstate. We showed how velocity and flux field can be computed for modeling of simple biochemical reaction systems, such as birth and death process, bistable Schlogl model, and oscillatory Schnakenberg system. Results we obtained for Schnakenberg system are consistent with the results obtained with other methods such as the widely used Fokker-Planck flux.

Developed in this work, discrete probability flux and velocity fields are of great importance. Indeed, they address the problem of modeling systems with low copy numbers and large differences in reaction rates, where the probability flux methods based on continuous approximations are problematic and stochasticity is prominent. For instance, we showed that widely used the Fokker-Planck flux based on continuous approximation of dCME, and the Liouville flux based on ODEs, generate the flux trajectories that are similar to each other for the toggle-switch model with slow promoter dynamics and weak promoter binding. However, the discrete stochastic flux trajectories are different for both. Particularly, the discrete stochastic flux exhibits strong oscillating behavior at the non-equilibrium steady state, which is due to strong fluctuations between binding and unbinding events. In contrast, Fokker-Planck and Liouville models fail to capture this phenomenon. We further investigated the oscillations in feedback loop, which were known before. We showed that in toggle switch model oscillatory trajectories connect subsets of important phenotypic states. Whereas in negative feedback loop all the important phenotypic states are connected with the oscillatory trajectories sequentially.

We also applied the discrete probability velocity and flux to analyze the effect of the phenomena of gene duplication in toggle switch system. We showed probability flux field for different cases of the expression level in daughter genes after duplication. Our results suggest that when daughter gene transcription level is reduced after duplication, the behavior of the system is closest to that before the duplication, when the expression rates are asymmetric and the difference in their values is largest.

CITED LITERATURE

1. Stewart-Ornstein, J. and El-Samad, H.: Stochastic modeling of cellular networks. In *Methods in cell biology* , volume 110, pages 111–137. Elsevier, 2012.

2. Qian, H.: Cooperativity in cellular biochemical processes: noise-enhanced sensitivity, fluctuating enzyme, bistability with nonlinear feedback, and other mechanisms for sigmoidal responses. *Annual review of biophysics* , 41:179–204, 2012.

3. Schnakenberg, J.: Network theory of microscopic and macroscopic behavior of master equation systems. *Reviews of Modern Physics* , 48(4):571, 1976.

4. Gillespie, D. T.: A rigorous derivation of the chemical master equation. *Physica A: Statistical Mechanics and its Applications* , 188(1-3):404–425, 1992.

5. Van Kampen, N. G.: *Stochastic processes in physics and chemistry* , volume 1. Elsevier, 1992.

6. Gillespie, D. T.: A general method for numerically simulating the stochastic time evolution of coupled chemical reactions. *Journal of computational physics* , 22(4):403–434, 1976.

7. Gillespie, D. T.: Exact stochastic simulation of coupled chemical reactions. *The journal of physical chemistry* , 81(25):2340–2361, 1977.

8. Gillespie, D. T.: The chemical langevin equation. *The Journal of Chemical Physics* , 113(1):297–306, 2000.

9. Daigle Jr, B. J., Roh, M. K., Gillespie, D. T., and Petzold, L. R.: Automated estimation of rare event probabilities in biochemical systems. *The Journal of Chemical Physics* , 134(4):01B628, 2011.

10. Cao, Y. and Liang, J.: Adaptively biased sequential importance sampling for rare events in reaction networks with comparison to exact solutions from finite buffer dcme method. *The Journal of Chemical Physics* , 139(2):07B605_1, 2013.

11. Karlebach, G. and Shamir, R.: Modelling and analysis of gene regulatory networks. *Nature Reviews Molecular Cell Biology* , 9(10):770, 2008.

12. Gillespie, D. T.: The chemical langevin and fokker- planck equations for the reversible isomerization reaction. *The Journal of Physical Chemistry A* , 106(20):5063–5071, 2002.

13. Gardner, T. S., Cantor, C. R., and Collins, J. J.: Construction of a genetic toggle switch in escherichia coli. *Nature* , 403(6767):339, 2000.

14. Kepler, T. B. and Elston, T. C.: Stochasticity in transcriptional regulation: origins, consequences, and mathematical representations. *Biophysical journal* , 81(6):3116–3136, 2001.

15. Goodwin, B. C. et al.: Temporal organization in cells. a dynamic theory of cellular control processes. *Temporal organization in cells. A dynamic theory of cellular control processes.* , 1963.

16. McAdams, H. H. and Arkin, A.: It?sa noisy business! genetic regulation at the nanomolar scale. *Trends in Genetics* , 15(2):65–69, 1999.

17. Cao, Y. and Liang, J.: Optimal enumeration of state space of finitely buffered stochastic molecular networks and exact computation of steady state landscape probability. *BMC Systems Biology* , 2(1):30, 2008.

18. Cao, Y., Lu, H.-M., and Liang, J.: Probability landscape of heritable and robust epigenetic state of lysogeny in phage lambda. *Proceedings of the National Academy of Sciences* , 107(43):18445–18450, 2010.

19. Alon, U.: *An introduction to systems biology: design principles of biological circuits* . CRC press, 2006.

20. Sorrells, T. R. and Johnson, A. D.: Making sense of transcription networks. *Cell* , 161(4):714–723, 2015.

21. Papatsenko, D., Darr, H., Kulakovskiy, I. V., Waghray, A., Makeev, V. J., MacArthur, B. D., and Lemischka, I. R.: Single-cell analyses of escs reveal alternative pluripotent cell states and molecular mechanisms that control self-renewal. *Stem cell reports* , 5(2):207–220, 2015.

22. Boyer, L. A., Lee, T. I., Cole, M. F., Johnstone, S. E., Levine, S. S., Zucker, J. P., Guenther, M. G., Kumar, R. M., Murray, H. L., Jenner, R. G., et al.: Core transcriptional regulatory circuitry in human embryonic stem cells. *cell* , 122(6):947–956, 2005.

23. Tsang, J., Zhu, J., and van Oudenaarden, A.: Microrna-mediated feedback and feedforward loops are recurrent network motifs in mammals. *Molecular cell* , 26(5):753–767, 2007.

24. Ivey, K. N. and Srivastava, D.: Micrornas as regulators of differentiation and cell fate decisions. *Cell stem cell* , 7(1):36–41, 2010.

25. Re, A., Corá, D., Taverna, D., and Caselle, M.: Genome-wide survey of microrna–transcription factor feed-forward regulatory circuits in human. *Molecular BioSystems* , 5(8):854–867, 2009.

26. Siegal-Gaskins, D., Grotewold, E., and Smith, G. D.: The capacity for multistability in small gene regulatory networks. *BMC Systems Biology* , 3(1):1, 2009.

27. Thomas, P., Popović, N., and Grima, R.: Phenotypic switching in gene regulatory networks. *Proceedings of the National Academy of Sciences* , 111(19):6994–6999, 2014.

28. Feng, H. and Wang, J.: A new mechanism of stem cell differentiation through slow binding/unbinding of regulators to genes. *Scientific reports* , 2, 2012.

29. Chen, Y., Lv, C., Li, F., and Li, T.: Distinguishing the rates of gene activation from phenotypic variations. *BMC systems biology* , 9(1):1, 2015.

30. Duncan, A., Liao, S., Vejchodskỳ, T., Erban, R., and Grima, R.: Noise-induced multistability in chemical systems: Discrete versus continuum modeling. *Physical Review E* , 91(4):042111, 2015.

31. Strasser, M., Theis, F. J., and Marr, C.: Stability and multiattractor dynamics of a toggle switch based on a two-stage model of stochastic gene expression. *Biophysical Journal* , 102(1):19–29, 2012.

32. Margaret, J. T., Chu, B. K., Roy, M., and Read, E. L.: Dna-binding kinetics determines the mechanism of noise-induced switching in gene networks. *Biophysical Journal* , 109(8):1746–1757, 2015.

33. Zia, R. and Schmittmann, B.: Probability currents as principal characteristics in the statistical mechanics of non-equilibrium steady states. *Journal of Statistical Mechanics: Theory and Experiment*, 2007(07):P07012, 2007.

34. Li, C., Wang, E., and Wang, J.: Landscape, flux, correlation, resonance, coherence, stability, and key network wirings of stochastic circadian oscillation. *Biophysical Journal*, 101(6):1335–1344, 2011.

35. Zhang, X.-J., Qian, H., and Qian, M.: Stochastic theory of nonequilibrium steady states and its applications. part i. *Physics Reports*, 510(1):1–86, 2012.

36. Wang, J., Xu, L., and Wang, E.: Potential landscape and flux framework of nonequilibrium networks: robustness, dissipation, and coherence of biochemical oscillations. *Proceedings of the National Academy of Sciences*, 105(34):12271–12276, 2008.

37. Xu, L., Shi, H., Feng, H., and Wang, J.: The energy pump and the origin of the nonequilibrium flux of the dynamical systems and the networks. *The Journal of Chemical Physics*, 136(16):165102, 2012.

38. Terebus, A., Liu, C., and Liang, J.: Discrete flux and velocity fields of probability and their global maps in reaction systems. *The Journal of Chemical Physics*, 149(18):185101, 2018.

39. Li, C. and Wang, J.: Landscape and flux reveal a new global view and physical quantification of mammalian cell cycle. *Proceedings of the National Academy of Sciences*, 111(39):14130–14135, 2014.

40. de Oliveira, L. R., Bazzani, A., Giampieri, E., and Castellani, G. C.: The role of nonequilibrium fluxes in the relaxation processes of the linear chemical master equation. *The Journal of Chemical Physics*, 141(6):08B608_1, 2014.

41. Bianca, C. and Lemarchand, A.: Evaluation of reaction fluxes in stationary and oscillating far-from-equilibrium biological systems. *Physica A: Statistical Mechanics and its Applications*, 438:1–16, 2015.

42. Wang, J., Xu, L., Wang, E., and Huang, S.: The potential landscape of genetic circuits imposes the arrow of time in stem cell differentiation. *Biophysical Journal*, 99(1):29–39, 2010.

43. Li, C. and Wang, J.: Quantifying the underlying landscape and paths of cancer. *Journal of The Royal Society Interface*, 11(100):20140774, 2014.

44. Tang, Y., Yuan, R., Wang, G., Zhu, X., and Ao, P.: Potential landscape of high dimensional nonlinear stochastic dynamics with large noise. *Scientific Reports*, 7:15762, 2017.

45. Shankar, R.: *Principles of quantum mechanics*. Springer Science & Business Media, 2012.

46. Xu, S., Sheng, P., and Liu, C.: An energetic variational approach for ion transport. *arXiv preprint arXiv:1408.4114*, 2014.

47. Keener, J. and Sneyd, J.: *Biochemical Reactions*. Springer, 1998.

48. Kurtz, T. G.: The relationship between stochastic and deterministic models for chemical reactions. *The Journal of Chemical Physics*, 57(7):2976–2978, 1972.

49. Kurtz, T.: Limit theorems for sequences of jump markov processes. *J Appl Probab*, 8(2):344–356, 1971.

50. Gillespie, C. S.: Moment-closure approximations for mass-action models. *IET systems biology*, 3(1):52–58, 2009.

51. Smadbeck, P. and Kaznessis, Y. N.: A closure scheme for chemical master equations. *Proceedings of the National Academy of Sciences*, 110(35):14261–14265, 2013.

52. Grima, R.: A study of the accuracy of moment-closure approximations for stochastic chemical kinetics. *The Journal of chemical physics*, 136(15):04B616, 2012.

53. Ivanov, I. V., Qian, X., and Pal, R.: *Emerging Research in the Analysis and Modeling of Gene Regulatory Networks*. IGI Global, 2016.

54. Milo, R., Shen-Orr, S., Itzkovitz, S., Kashtan, N., Chklovskii, D., and Alon, U.: Network motifs: simple building blocks of complex networks. *Science*, 298(5594):824–827, 2002.

55. Maamar, H., Raj, A., and Dubnau, D.: Noise in gene expression determines cell fate in bacillus subtilis. *Science*, 317(5837):526–529, 2007.

56. Inui, M., Martello, G., and Piccolo, S.: Microrna control of signal transduction. *Nature reviews Molecular cell biology* , 11(4):252, 2010.

57. Ferrell Jr, J. E.: Self-perpetuating states in signal transduction: positive feedback, double-negative feedback and bistability. *Current opinion in cell biology* , 14(2):140–148, 2002.

58. Düvel, K., Yecies, J. L., Menon, S., Raman, P., Lipovsky, A. I., Souza, A. L., Triantafellow, E., Ma, Q., Gorski, R., Cleaver, S., et al.: Activation of a metabolic gene regulatory network downstream of mtor complex 1. *Molecular cell* , 39(2):171–183, 2010.

59. Covert, M. W. and Palsson, B. Ø.: Transcriptional regulation in constraints-based metabolic models of escherichia coli. *Journal of Biological Chemistry* , 277(31):28058–28064, 2002.

60. McAdams, H. H. and Arkin, A.: Stochastic mechanisms in gene expression. *Proceedings of the National Academy of Sciences* , 94(3):814–819, 1997.

61. Shahrezaei, V., Ollivier, J. F., and Swain, P. S.: Colored extrinsic fluctuations and stochastic gene expression. *Molecular Systems Biology* , 4(1):196, 2008.

62. Elowitz, M. B., Levine, A. J., Siggia, E. D., and Swain, P. S.: Stochastic gene expression in a single cell. *Science* , 297(5584):1183–1186, 2002.

63. Swain, P. S., Elowitz, M. B., and Siggia, E. D.: Intrinsic and extrinsic contributions to stochasticity in gene expression. *Proceedings of the National Academy of Sciences* , 99(20):12795–12800, 2002.

64. Kærn, M., Elston, T. C., Blake, W. J., and Collins, J. J.: Stochasticity in gene expression: from theories to phenotypes. *Nature Reviews Genetics* , 6(6):451–464, 2005.

65. Vellela, M. and Qian, H.: A quasistationary analysis of a stochastic chemical reaction: Keizer?s paradox. *Bulletin of Mathematical Biology* , 69(5):1727–1746, 2007.

66. Munsky, B. and Khammash, M.: The finite state projection algorithm for the solution of the chemical master equation. *The Journal of chemical physics* , 124(4):044104, 2006.

67. Wolf, V., Goel, R., Mateescu, M., and Henzinger, T. A.: Solving the chemical master equation using sliding windows. *BMC Systems Biology* , 4(1):42, 2010.

68. Kazeev, V., Khammash, M., Nip, M., and Schwab, C.: Direct solution of the chemical master equation using quantized tensor trains. *PLoS computational biology* , 10(3):e1003359, 2014.

69. Cao, Y., Terebus, A., and Liang, J.: State space truncation with quantified errors for accurate solutions to discrete chemical master equation. *Bulletin of mathematical biology* , 78(4):617–661, 2016.

70. Darvey, I. G., Ninham, B., and Staff, P.: Stochastic models for second-order chemical reaction kinetics. the equilibrium state. *The journal of chemical physics* , 45(6):2145–2155, 1966.

71. McQuarrie, D. A.: Stochastic approach to chemical kinetics. *Journal of Applied Probability* , 4(3):413–478, 1967.

72. Laurenzi, I. J.: An analytical solution of the stochastic master equation for reversible bimolecular reaction kinetics. *The Journal of Chemical Physics* , 113(8):3315–3322, 2000.

73. Van Kampen, N. G.: *Stochastic processes in physics and chemistry* . Elsevier, 2007.

74. Sjöberg, P., Lötstedt, P., and Elf, J.: Fokker–planck approximation of the master equation in molecular biology. *Computing and Visualization in Science* , 12(1):37–50, 2009.

75. Grima, R., Thomas, P., and Straube, A. V.: How accurate are the nonlinear chemical fokker-planck and chemical langevin equations? *The Journal of Chemical Physics* , 135(8):084103, 2011.

76. Baras, F., Mansour, M. M., and Pearson, J.: Microscopic simulation of chemical bistability in homogeneous systems. *The Journal of Chemical Physics* , 105(18):8257–8261, 1996.

77. Kuwahara, H. and Mura, I.: An efficient and exact stochastic simulation method to analyze rare events in biochemical systems. *The Journal of chemical physics* , 129(16):10B619, 2008.

78. Gillespie, D. T., Roh, M., and Petzold, L. R.: Refining the weighted stochastic simulation algorithm. *The Journal of chemical physics* , 130(17):174103, 2009.

79. MacNamara, S., Bersani, A. M., Burrage, K., and Sidje, R. B.: Stochastic chemical kinetics and the total quasi-steady-state assumption: application to the stochastic simulation algorithm and chemical master equation. *The Journal of chemical physics* , 129(9):09B605, 2008.

80. MacNamara, S., Burrage, K., and Sidje, R. B.: Multiscale modeling of chemical kinetics via the master equation. *Multiscale Modeling & Simulation* , 6(4):1146–1168, 2008.

81. Jahnke, T.: On reduced models for the chemical master equation. *Multiscale Modeling & Simulation* , 9(4):1646–1676, 2011.

82. Sidje, R. B.: Expokit: A software package for computing matrix exponentials. *ACM Transactions on Mathematical Software (TOMS)* , 24(1):130–156, 1998.

83. Munsky, B. and Khammash, M.: A multiple time interval finite state projection algorithm for the solution to the chemical master equation. *Journal of Computational Physics* , 226(1):818–835, 2007.

84. Cao, Y., Terebus, A., and Liang, J.: Accurate chemical master equation solution using multi-finite buffers. *Multiscale Modeling & Simulation* , 14(2):923–963, 2016.

85. Terebus, A., Cao, Y., and Liang, J.: Exact computation of probability landscape of stochastic networks of single input and coupled toggle switch modules. In *2014 36th Annual International Conference of the IEEE Engineering in Medicine and Biology Society* , pages 5228–5231. IEEE, 2014.

86. Karlin, S. and Taylor, H. E.: *A second course in stochastic processes* . Elsevier, 1981.

87. Arkin, A., Ross, J., and McAdams, H. H.: Stochastic kinetic analysis of developmental pathway bifurcation in phage λ-infected escherichia coli cells. *Genetics* , 149(4):1633–1648, 1998.

88. Aurell, E., Brown, S., Johanson, J., and Sneppen, K.: Stability puzzles in phage λ. *Physical Review E* , 65(5):051914, 2002.

89. Zhu, X.-M., Yin, L., Hood, L., and Ao, P.: Calculating biological behaviors of epigenetic states in the phage λ life cycle. *Functional & integrative genomics* , 4(3):188–195, 2004.

90. Cao, Y. and Liang, J.: Nonlinear langevin model with product stochasticity for biological networks: the case of the schnakenberg model. *Journal of Systems Science and Complexity* , 23(5):896–905, 2010.

91. Li, M., McClure, W., and Susskind, M. M.: Changing the mechanism of transcriptional activation by phage λ repressor. *Proceedings of the National Academy of Sciences* , 94(8):3691–3696, 1997.

92. Hawley, D. K. and McClure, W. R.: In vitro comparison of initiation properties of bacteriophage lambda wild-type pr and x3 mutant promoters. *Proceedings of the National Academy of Sciences* , 77(11):6381–6385, 1980.

93. Hawley, D. K. and Mcclure, W. R.: Mechanism of activation of transcription initiation from the λprm promoter. *Journal of molecular biology* , 157(3):493–525, 1982.

94. Shea, M. A. and Ackers, G. K.: The or control system of bacteriophage lambda: A physical-chemical model for gene regulation. *Journal of molecular biology* , 181(2):211–230, 1985.

95. Kuttler, C. and Niehren, J.: Gene regulation in the pi calculus: Simulating cooperativity at the lambda switch. In *Transactions on computational systems biology VII* , pages 24–55. Springer, 2006.

96. Schultz, D., Jacob, E. B., Onuchic, J. N., and Wolynes, P. G.: Molecular level stochastic model for competence cycles in bacillus subtilis. *PNAS* , 104(45), 2007.

97. Huang, S., Ernberg, I., and Kauffman, S.: Cancer attractors: a systems view of tumors from a gene network dynamics and developmental perspective. In *Seminars in cell & developmental biology* , volume 20, pages 869–876. Elsevier, 2009.

98. Shiraishi, T., Matsuyama, S., and Kitano, H.: Large-scale analysis of network bistability for human cancers. *PLoS computational biology* , 6(7):e1000851, 2010.

99. Lu, T., Shen, T., Bennett, M. R., Wolynes, P. G., and Hasty, J.: Phenotypic variability of growing cellular populations. *Proceedings of the National Academy of Sciences* , 104(48):18982–18987, 2007.

100. Cao, Y., Terebus, A., and Liang, J.: Accurate chemical master equation solution using multi-finite buffers. *Multiscale Modeling & Simulation* , 14(2):923–963, 2016.

101. Lee, T. I., Rinaldi, N. J., Robert, F., Odom, D. T., Bar-Joseph, Z., Gerber, G. K., Hannett, N. M., Harbison, C. T., Thompson, C. M., Simon, I., et al.: Transcriptional regulatory networks in saccharomyces cerevisiae. *science* , 298(5594):799–804, 2002.

102. Shen-Orr, S. S., Milo, R., Mangan, S., and Alon, U.: Network motifs in the transcriptional regulation network of escherichia coli. *Nature genetics* , 31(1):64–68, 2002.

103. Mangan, S., Itzkovitz, S., Zaslaver, A., and Alon, U.: The incoherent feed-forward loop accelerates the response-time of the gal system of escherichia coli. *Journal of molecular biology* , 356(5):1073–1081, 2006.

104. Mangan, S. and Alon, U.: Structure and function of the feed-forward loop network motif. *Proceedings of the National Academy of Sciences* , 100(21):11980–11985, 2003.

105. François, P. and Siggia, E. D.: A case study of evolutionary computation of biochemical adaptation. *Physical biology* , 5(2):026009, 2008.

106. Ma, W., Trusina, A., El-Samad, H., Lim, W. A., and Tang, C.: Defining network topologies that can achieve biochemical adaptation. *Cell* , 138(4):760–773, 2009.

107. Goentoro, L., Shoval, O., Kirschner, M. W., and Alon, U.: The incoherent feedforward loop can provide fold-change detection in gene regulation. *Molecular cell* , 36(5):894–899, 2009.

108. Kittisopikul, M. and Süel, G. M.: Biological role of noise encoded in a genetic network motif. *Proceedings of the National Academy of Sciences* , 107(30):13300–13305, 2010.

109. Wang, P., Lü, J., and Ogorzalek, M. J.: Global relative parameter sensitivities of the feed-forward loops in genetic networks. *Neurocomputing* , 78(1):155–165, 2012.

110. Wang, R.-S., Saadatpour, A., and Albert, R.: Boolean modeling in systems biology: an overview of methodology and applications. *Physical biology* , 9(5):055001, 2012.

111. Conrad, B. and Antonarakis, S. E.: Gene duplication: a drive for phenotypic diversity and cause of human disease. *Annu. Rev. Genomics Hum. Genet.* , 8:17–35, 2007.

112. Lynch, M. and Conery, J. S.: The evolutionary fate and consequences of duplicate genes. *Science* , 290(5494):1151–1155, 2000.

113. Kondrashov, F. A.: Gene duplication as a mechanism of genomic adaptation to a changing environment. In *Proc. R. Soc. B* , volume 279, pages 5048–5057. The Royal Society, 2012.

114. Acar, M., Mettetal, J. T., and van Oudenaarden, A.: Stochastic switching as a survival strategy in fluctuating environments. *Nature genetics* , 40(4):471–475, 2008.

115. Gunawan, R., Cao, Y., Petzold, L., and Doyle III, F. J.: Sensitivity analysis of discrete stochastic systems. *Biophysical journal* , 88(4):2530–2540, 2005.

116. Vo, H. D. and Sidje, R. B.: An adaptive solution to the chemical master equation using tensors. *The Journal of chemical physics* , 147(4):044102, 2017.

117. Burrage, K., Hegland, M., Macnamara, S., Sidje, R., et al.: A krylov-based finite state projection algorithm for solving the chemical master equation arising in the discrete modelling of biological systems. In *Proc. of The AA Markov 150th Anniversary Meeting* , number 21-37, 2006.

118. Yuan, R., Wang, X., Ma, Y., Yuan, B., and Ao, P.: Exploring a noisy van der pol type oscillator with a stochastic approach. *Physical Review E* , 87(6):062109, 2013.

119. Mou, C. Y., Luo, J.-l., and Nicolis, G.: Stochastic thermodynamics of nonequilibrium steady states in chemical reaction systems. *The Journal of Chemical Physics* , 84(12):7011–7017, 1986.

120. Schmiedl, T. and Seifert, U.: Stochastic thermodynamics of chemical reaction networks. *The Journal of Chemical Physics* , 126(4):044101, 2007.

121. Schultz, D., Walczak, A. M., Onuchic, J. N., and Wolynes, P. G.: Extinction and resurrection in gene networks. *Proceedings of the National Academy of Sciences* , 105(49):19165–19170, 2008.

122. Tang, Y., Yuan, R., and Ao, P.: Nonequilibrium work relation beyond the boltzmann-gibbs distribution. *Physical Review E* , 89(6):062112, 2014.

123. Zhou, P. and Li, T.: Construction of the landscape for multi-stable systems: Potential landscape, quasi-potential, a-type integral and beyond. *The Journal of Chemical Physics* , 144(9):094109, 2016.

124. Bazzani, A., Castellani, G. C., Giampieri, E., Remondini, D., and Cooper, L. N.: Bistability in the chemical master equation for dual phosphorylation cycles. *The Journal of Chemical Physics* , 136(23):06B611, 2012.

125. Horowitz, J. M. and Esposito, M.: Thermodynamics with continuous information flow. *Physical Review X* , 4(3):031015, 2014.

126. Ceccato, A. and Frezzato, D.: Remarks on the chemical fokker-planck and langevin equations: Nonphysical currents at equilibrium. *The Journal of Chemical Physics* , 148(6):064114, 2018.

127. Allen, L. J.: *An introduction to stochastic processes with applications to biology* . CRC Press, 2010.

128. Schlögl, F.: Chemical reaction models for non-equilibrium phase transitions. *Zeitschrift für Physik* , 253(2):147–161, 1972.

129. Qian, H., Saffarian, S., and Elson, E. L.: Concentration fluctuations in a mesoscopic oscillating chemical reaction system. *Proceedings of the National Academy of Sciences* , 99(16):10376–10381, 2002.

130. Ge, H., Qian, M., and Qian, H.: Stochastic theory of nonequilibrium steady states. part ii: Applications in chemical biophysics. *Physics Reports* , 510(3):87–118, 2012.

131. Vellela, M. and Qian, H.: Stochastic dynamics and non-equilibrium thermodynamics of a bistable chemical system: the schlögl model revisited. *Journal of The Royal Society Interface* , 6(39):925–940, 2009.

132. Sekine, R., Yamamura, M., Ayukawa, S., Ishimatsu, K., Akama, S., Takinoue, M., Hagiya, M., and Kiga, D.: Tunable synthetic phenotypic diversification on waddingtons landscape through autonomous signaling. *Proceedings of the National Academy of Sciences* , 108(44):17969–17973, 2011.

133. Wu, M., Su, R.-Q., Li, X., Ellis, T., Lai, Y.-C., and Wang, X.: Engineering of regulated stochastic cell fate determination. *Proceedings of the National Academy of Sciences* , 110(26):10610–10615, 2013.

134. Balázsi, G., van Oudenaarden, A., and Collins, J. J.: Cellular decision making and biological noise: from microbes to mammals. *Cell* , 144(6):910–925, 2011.

135. Lugagne, J.-B., Carrillo, S. S., Kirch, M., Köhler, A., Batt, G., and Hersen, P.: Balancing a genetic toggle switch by real-time feedback control and periodic forcing. *Nature Communications* , 8(1):1671, 2017.

136. Kim, K.-Y. and Wang, J.: Potential energy landscape and robustness of a gene regulatory network: toggle switch. *PLoS Computational Biology* , 3(3):e60, 2007.

137. Wilkinson, D. J.: Stochastic modelling for quantitative description of heterogeneous biological systems. *Nature Reviews Genetics* , 10(2):122, 2009.

138. Szekely, T. and Burrage, K.: Stochastic simulation in systems biology. *Computational and structural biotechnology journal* , 12(20):14–25, 2014.

139. Hanggi, P., Grabert, H., Talkner, P., and Thomas, H.: Bistable systems: Master equation versus fokker-planck modeling. *Physical Review A* , 29(1):371, 1984.

140. Tran, L. M., Rizk, M. L., and Liao, J. C.: Ensemble modeling of metabolic networks. *Biophysical journal* , 95(12):5606–5617, 2008.

141. Beard, D. A. and Qian, H.: Relationship between thermodynamic driving force and one-way fluxes in reversible processes. *PloS one* , 2(1):e144, 2007.

142. Wiechert, W.: The thermodynamic meaning of metabolic exchange fluxes. *Biophysical journal* , 93(6):2255–2264, 2007.

143. Schultz, D., Onuchic, J. N., and Wolynes, P. G.: Understanding stochastic simulations of the smallest genetic networks. *The Journal of Chemical Physics* , 126(24):06B613, 2007.

144. Wang, J., Zhang, J., Yuan, Z., and Zhou, T.: Noise-induced switches in network systems of the genetic toggle switch. *BMC Systems Biology* , 1(1):50, 2007.

145. Verd, B., Crombach, A., and Jaeger, J.: Classification of transient behaviours in a time-dependent toggle switch model. *BMC Systems Biology* , 8(1):43, 2014.

146. Fang, X., Liu, Q., Bohrer, C., Hensel, Z., Han, W., Wang, J., and Xiao, J.: Cell fate potentials and switching kinetics uncovered in a classic bistable genetic switch. *Nature communications* , 9(1):2787, 2018.

147. Warren, P. B. and ten Wolde, P. R.: Chemical models of genetic toggle switches. *The Journal of Physical Chemistry B* , 109(14):6812–6823, 2005.

148. Gardiner, C. W. et al.: *Handbook of stochastic methods* , volume 3. springer Berlin, 1985.

149. Elowitz, M. B. and Leibler, S.: A synthetic oscillatory network of transcriptional regulators. *Nature* , 403(6767):335, 2000.

150. Buse, O., Pérez, R., and Kuznetsov, A.: Dynamical properties of the repressilator model. *Physical Review E* , 81(6):066206, 2010.

151. Loinger, A. and Biham, O.: Stochastic simulations of the repressilator circuit. *Physical Review E* , 76(5):051917, 2007.

152. Xiao, M. and Cao, J.: Genetic oscillation deduced from hopf bifurcation in a genetic regulatory network with delays. *Mathematical biosciences* , 215(1):55–63, 2008.

153. Smolen, P., Baxter, D. A., and Byrne, J. H.: A reduced model clarifies the role of feedback loops and time delays in the drosophila circadian oscillator. *Biophysical journal* , 83(5):2349–2359, 2002.

154. Feng, H., Han, B., and Wang, J.: Landscape and global stability of nonadiabatic and adiabatic oscillations in a gene network. *Biophysical journal* , 102(5):1001–1010, 2012.

155. Novák, B. and Tyson, J. J.: Design principles of biochemical oscillators. *Nature reviews Molecular cell biology* , 9(12):981, 2008.

156. Qian, W., Liao, B.-Y., Chang, A. Y.-F., and Zhang, J.: Maintenance of duplicate genes and their functional redundancy by reduced expression. *Trends in Genetics* , 26(10):425–430, 2010.

APPENDICES

The license to publish chapters of the paper: Cao, Youfang, Anna Terebus, and Jie Liang. "State space truncation with quantified errors for accurate solutions to discrete chemical master equation." Bulletin of mathematical biology 78.4 (2016): 617-661.

requirements specified in the attached copy of your order form, and for no other use, subject to the conditions below:

1. The Licensor warrants that it has, to the best of its knowledge, the rights to license reuse of this material. However, you should ensure that the material you are requesting is original to the Licensor and does not carry the copyright of another entity (as credited in the published version).

   If the credit line on any part of the material you have requested indicates that it was reprinted or adapted with permission from another source, then you should also seek permission from that source to reuse the material.

2. Where **print only** permission has been granted for a fee, separate permission must be obtained for any additional electronic re-use.

3. Permission granted **free of charge** for material in print is also usually granted for any electronic version of that work, provided that the material is incidental to your work as a whole and that the electronic version is essentially equivalent to, or substitutes for, the print version.

4. A licence for 'post on a website' is valid for 12 months from the licence date. This licence does not cover use of full text articles on websites.

5. Where **'reuse in a dissertation/thesis'** has been selected the following terms apply: Print rights of the final author's accepted manuscript (for clarity, NOT the published version) for up to 100 copies, electronic rights for use only on a personal website or institutional repository as defined by the Sherpa guideline (www.sherpa.ac.uk/romeo/).

6. Permission granted for books and journals is granted for the lifetime of the first edition and does not apply to second and subsequent editions (except where the first edition permission was granted free of charge or for signatories to the STM Permissions Guidelines http://www.stm-assoc.org/copyright-legal-affairs/permissions/permissions-guidelines/), and does not apply for editions in other languages unless additional translation rights have been granted separately in the licence.

7. Rights for additional components such as custom editions and derivatives require additional permission and may be subject to an additional fee. Please apply to Journalpermissions@springernature.com/bookpermissions@springernature.com for these rights.

8. The Licensor's permission must be acknowledged next to the licensed material in print. In electronic form, this acknowledgement must be visible at the same time as the figures/tables/illustrations or abstract, and must be hyperlinked to the journal/book's homepage. Our required acknowledgement format is in the Appendix below.

9. Use of the material for incidental promotional use, minor editing privileges (this does not include cropping, adapting, omitting material or any other changes that affect the meaning, intention or moral rights of the author) and copies for the disabled are permitted under this licence.

10. Minor adaptations of single figures (changes of format, colour and style) do not require the Licensor's approval. However, the adaptation should be credited as shown in Appendix below.

Appendix — Acknowledgements:

For Journal Content:
Reprinted by permission from [**the Licensor**]: [**Journal Publisher** (e.g.

The license to publish chapters of the paper: "Exact computation of probability landscape of stochastic networks of single input and coupled toggle switch modules." 2014 36th Annual International Conference of the IEEE Engineering in Medicine and Biology Society. IEEE, 2014.

The license to publish chapters of the paper: "Terebus, Anna, Chun Liu, and Jie Liang. "Discrete flux and velocity fields of probability and their global maps in reaction systems." The Journal of chemical physics 149.18 (2018): 185101."

180

AIP PUBLISHING LICENSE
TERMS AND CONDITIONS

May 17, 2019

This Agreement between Anna Terebus ("You") and AIP Publishing ("AIP Publishing") consists of your license details and the terms and conditions provided by AIP Publishing and Copyright Clearance Center.

License Number	4591531208934
License date	May 17, 2019
Licensed Content Publisher	AIP Publishing
Licensed Content Publication	Journal of Chemical Physics
Licensed Content Title	Discrete flux and velocity fields of probability and their global maps in reaction systems
Licensed Content Author	Anna Terebus, Chun Liu, Jie Liang
Licensed Content Date	Nov 14, 2018
Licensed Content Volume	149
Licensed Content Issue	18
Type of Use	Thesis/Dissertation
Requestor type	Author (original article)
Format	Print and electronic
Portion	Excerpt (> 800 words)
Will you be translating?	No
Title of your thesis / dissertation	COMPUTING LANDSCAPE, VELOCITY AND FLUX OFPROBABILITY MASS IN GENE REGULATORY NETWORKS
Expected completion date	Jun 2019
Estimated size (number of pages)	160
Requestor Location	Anna Terebus 215 W Washington, Apt 3311 CHICAGO, IL 60606 United States Attn: Anna Terebus
Total	0.00 USD

Terms and Conditions

AIP Publishing -- Terms and Conditions: Permissions Uses

AIP Publishing hereby grants to you the non-exclusive right and license to use and/or distribute the Material according to the use specified in your order, on a one-time basis, for the specified term, with a maximum distribution equal to the number that you have ordered. Any links or other content accompanying the Material are not the subject of this license.

1. You agree to include the following copyright and permission notice with the reproduction of the Material:"Reprinted from [FULL CITATION], with the permission of AIP Publishing." For an article, the credit line and permission notice must be printed on the first page of the article or book chapter. For photographs, covers, or tables, the notice may appear with the Material, in a footnote, or in the reference list.

2. If you have licensed reuse of a figure, photograph, cover, or table, it is your responsibility to ensure that the material is original to AIP Publishing and does not contain the copyright of another entity, and that the copyright notice of the figure, photograph, cover, or table does not indicate that it was reprinted by AIP Publishing, with permission, from another source. Under no circumstances does AIP Publishing purport or intend to grant permission to reuse material to which it does not hold appropriate rights.
You may not alter or modify the Material in any manner. You may translate the Material into

another language only if you have licensed translation rights. You may not use the Material for promotional purposes.

3. The foregoing license shall not take effect unless and until AIP Publishing or its agent, Copyright Clearance Center, receives the Payment in accordance with Copyright Clearance Center Billing and Payment Terms and Conditions, which are incorporated herein by reference.

4. AIP Publishing or Copyright Clearance Center may, within two business days of granting this license, revoke the license for any reason whatsoever, with a full refund payable to you. Should you violate the terms of this license at any time, AIP Publishing, or Copyright Clearance Center may revoke the license with no refund to you. Notice of such revocation will be made using the contact information provided by you. Failure to receive such notice will not nullify the revocation.

5. AIP Publishing makes no representations or warranties with respect to the Material. You agree to indemnify and hold harmless AIP Publishing, and their officers, directors, employees or agents from and against any and all claims arising out of your use of the Material other than as specifically authorized herein.

6. The permission granted herein is personal to you and is not transferable or assignable without the prior written permission of AIP Publishing. This license may not be amended except in a writing signed by the party to be charged.

7. If purchase orders, acknowledgments or check endorsements are issued on any forms containing terms and conditions which are inconsistent with these provisions, such inconsistent terms and conditions shall be of no force and effect. This document, including the CCC Billing and Payment Terms and Conditions, shall be the entire agreement between the parties relating to the subject matter hereof.

This Agreement shall be governed by and construed in accordance with the laws of the State of New York. Both parties hereby submit to the jurisdiction of the courts of New York County for purposes of resolving any disputes that may arise hereunder.

V1.2

Questions? customercare@copyright.com or +1-855-239-3415 (toll free in the US) or +1-978-646-2777.

VITA

NAME:	Anna Terebus

EDUCATION: **Ph.D. in Bioinformatics**, University of Illinois at Chicago, Chicago, Illinois, 2019.

M.S. in Applied Mathematics with honors, Rivne State Humanitarian University, Rivne, Ukraine, 2009.

B.S. in Applied Mathematics with honors, Rivne State Humanitarian University, Rivne, Ukraine, 2008.

ACADEMIC EXPERIENCE

2012 - 2019   **Graduate Research Assistant**, Molecular and Systems Computational Bioengineering Lab, Department of Bioengineering, University of Illinois at Chicago

2013 - 2014   **Graduate Teaching Assistant**, Department of Bioengineering, University of Illinois at Chicago. Classes: Introduction to Bioinformatics and Bioinformatics Laboratory (Fall 2013 and Fall 2014); Biological Systems Modeling (Spring 2014)

2009 - 2012   **Research Assistant**, Mathematical Modeling Laboratory, Rivne State Humanitarian University, Rivne, Ukraine

2009, 2012   **Teaching Instructor**, Department of Applied Math and Informatics: Rivne State Humanitarian University, Rivne, Ukraine. Classes: Programming in C, Computer Algorithms (Spring 2012), Programming in Prolog (Fall 2009)

2012   **Little Academy of Science Advisor**, Rivne Nature Science and Mathematics Lyceum Elitar. Coached the team of high school students for the All Ukrainian Olympiad and Ukrainian Small Academy of Science Competition.

PUBLICATIONS

- **A. Terebus**, C. Liu, J. Liang Discrete and Continuous Numerical Models of Probability Flux of Switching Dynamics: Uncovering Stochastic Oscillations in Toggle-Switch System (manuscript).

- **A. Terebus**, Y. Cao, and J. Liang Sensitivities of Regulation Intensities in Feed-Forward Loops with Multistability Conf Proc IEEE Eng Med Biol Soc, 2019 (accepted).

- **A. Terebus**, C. Liu, J. Liang Discrete flux and velocity fields of probability and their global maps in reaction systems, Journal of Chem Physics, 2018, 149 (18), 185101.

- C. Ma, T. Luciani, **A. Terebus**, J. Liang, and G. E. Marai PRODIGEN: Visualizing the Probability Landscape of Stochastic Gene Regulatory Networks in State and Time Space, BMC Bioinformatics, BMC bioinformatics, 2017, 18 (2), 24.

- Y. Cao, **A. Terebus**, J. Liang State space truncation with quantified errors for accurate solutions to discrete Chemical Master Equation, Bull of Math Biol, 2016, 78(4):617-661.

- Y. Cao, **A. Terebus**, J. Liang Accurate Chemical Master Equation Solution using Multi-Finite Buffers, SIAM Mult Model and Simul, 2016, 14(2):923-963.

- G. Gursoy, **A. Terebus**, Y. Cao, and J. Liang Mechanisms of Stochastic Focusing and Defocusing in Biological Reaction Networks: Insight from Accurate Chemical Master Equation (ACME) Solutions, Conf Proc IEEE Eng Med Biol Soc, 2016, 1480-1483.

- J. Liang, Y. Cao, G. Gursoy, H. Naveed, **A. Terebus**, and J. Zhao Multiscale modeling of cellular epigenetic states: stochasticity in molecular networks, chromatin folding in cell nuclei, and tissue pattern formation of cells, Critic Rev in Biomed Eng, 2015, 43(4):323-346.

- **A. Terebus**, Y. Cao, and J. Liang "Exact computation of probability landscape of stochastic networks of Single Input and Coupled Toggle Switch Modules", Conf Proc IEEE Eng Med Biol Soc, 2014, 228-5231.

- A. Bomba, **A. Terebus** "A spatial generalization of the method of conformal mappings for the solution of model boundary-value filtration problems", Springer: Journal of Math Sciences, 187.5, 2012, pp. 596-605.

- A. Bomba, **A. Terebus** "Quasiideal fields modeling for thin spatially curved anisotropic layers", Reports of National Academy of Science of Ukraine, 2011, 10 pp: 37-43 (In Ukrainian).

AWARDS

2017-2019,   UIC Office of Dean of Students Leadership Award

2018-2019,   Chancellor's Student Service and Leadership Award

2016,   Quantitative Cell Biology Network travel support for the travel to Gordon Research conference "Stochastic Physics in Biology"

2016, 2018,   UIC Graduate Student Council Travel Award

2009,   Winner of the Zavtra.UA Viktor Pinchuk Foundation Scholarship

2007,   President of Ukraine Academic Scholarship

2006,   Rivne Administration Academic Scholarship

2004,   Double Winner in all Ukrainian Small Academy of Science Competition in mathematics and software engineering for mathematical research divisions

2002-2003,   Winner of Rivne Region Olympiad in Mathematics for High school students.

SEMINAR TALKS

2017,   Accurate Modeling of Stochastic Biochemical Reaction Networks: Noise-Induced Multistability, Velocity and Flux Fields of Probability Mass, Center for Computational Biology, **Flatiron Institute**, NYC, NY.

2016,   Exact Flux and Velocity Fields of Probability Mass in Biochemical Reaction Networks, Department of Mathematics, **Penn State University**, University Park, PA.

2012,   Spatial model analogues of boundary-value problems on conformal and quasiconformal mappings, Department of Cybernetics, **National Taras Shevchenko University**, Kyiv, Ukraine.

CONFERENCE TALKS

2017,   Feed-Forward Loop Network Motif As a Mediator of Phenotypic Switch in Cells, Great Lakes Bioinformatics Conference, University of Illinois at Chicago, Chicago IL.

2014,   Exact computation of probability landscape of stochastic networks of Single Input and Coupled Toggle Switch Modules", Engineering in Medical and Biological Society (EMBC), 36th Annual Int. Conf. of the IEEE, Chicago, IL.

POSTER PRESENTATIONS

- 2019, International Conference on Biomedical and Health Informatics, Chicago, IL.

- 2019, Biophysical Society 63rd Annual Meeting, Baltimore, MD.

- 2018, International Society of Computational Biology, Chicago, IL.

- 2018, Biophysical Society 62th Annual Meeting, San Francisco, CA.

- 2017, Great Lakes Bioinformatics Conference, Chicago, IL.

- 2017, Biophysical Society 61st Annual Meeting, New Orleans, LA.

- 2017, Gordon Research Conference: Stochastic Physics in Biology, Ventura, CA.

- 2016, Biophysical Society 60th Annual Meeting, Los Angeles, CA,

- 2015, Biophysical Society 59th Annual Meeting, Baltimore, MD.

- 2014, Biophysical Society 58th Annual Meeting, San Francisco, CA.

SERVICE, LEADERSHIP, AFFILIATIONS

2018-2019, President of UIC Graduate Student Council.

2018-2019, President of UIC College of Engineering Toastmasters Club.

2018, Member of International Society for Computational Biology.

2014, 2019-now, Member of Institute of Electrical and Electronic Engineers, Institute of Electrical and Electronic Engineers.

2014-now, Member of Biophysical Society.

2005-2012, Coach and Member of Jury of the Rivne region team to All-Ukrainian Mathematics Olympiad.

2012, Member of Jury of the 49th All-Ukrainian Mathematics Olympiad.